2001

The role of acoustic cavitation in enhanced ultrasound-induced heating in a tissue-mimicking phantom

BOSTON UNIVERSITY

COLLEGE OF ENGINEERING

Dissertation

THE ROLE OF ACOUSTIC CAVITATION IN ENHANCED ULTRASOUND-INDUCED HEATING IN A TISSUE-MIMICKING PHANTOM

by

PATRICK LEE EDSON

B.S., University of Rochester, 1995
M.S., Boston University, 2000

Submitted in partial fulfillment of the

requirements for the degree of

Doctor of Philosophy

2001

Approved by

First Reader

Ronald A. Roy, Ph.D.
Associate Professor of Mechanical Engineering

Second Reader

R. Glynn Holt, Ph.D.
Assistant Professor of Mechanical Engineering

Third Reader

Ali Nadim, Ph.D.
Associate Professor of Mechanical Engineering

Fourth Reader

Sheryl M. Grace, Ph.D.
Assistant Professor of Mechanical Engineering

THE ROLE OF ACOUSTIC CAVITATION IN ENHANCED ULTRASOUND-INDUCED HEATING IN A TISSUE-MIMICKING PHANTOM

(Order No.)

PATRICK LEE EDSON

Boston University, College of Engineering, 2001

Major Professor: Ronald A. Roy, Associate Professor of Mechanical Engineering

ABSTRACT

A complete understanding of high-intensity focused ultrasound-induced temperature changes in tissue requires insight into all potential mechanisms for heat deposition. Applications of therapeutic ultrasound often utilize acoustic pressures capable of producing cavitation activity. Recognizing the ability of bubbles to transfer acoustic energy into heat generation, a study of the role bubbles play in tissue hyperthermia becomes necessary. These bubbles are typically less than 50μm.

This dissertation examines the contribution of bubbles and their motion to an enhanced heating effect observed in a tissue-mimicking phantom. A series of experiments established a relationship between bubble activity and an enhanced temperature rise in the phantom by simultaneously measuring both the temperature change and acoustic emissions from bubbles. It was found that a strong correlation exists between the onset of the enhanced heating effect and observable cavitation activity. In addition, the likelihood of observing the enhanced heating effect was largely unaffected by the insonation duration for all but the shortest of insonation times, 0.1 seconds.

Numerical simulations were used investigate the relative importance of two candidate mechanisms for heat deposition from bubbles as a means to quantify the number of bubbles required to

produce the enhanced temperature rise. The energy deposition from viscous dissipation and the absorption of radiated sound from bubbles were considered as a function of the bubble size and the viscosity of the surrounding medium. Although both mechanisms were capable of producing the level of energy required for the enhanced heating effect, it was found that inertial cavitation, associated with high acoustic radiation and low viscous dissipation, coincided with the the nature of the cavitation best detected by the experimental system. The number of bubbles required to account for the enhanced heating effect was determined through the numerical study to be on the order of 150 or less.

Contents

List of Tables

List of Figures

Chapter 1

Introduction

Initial reports of the biological effects of "high intensity sound waves" [2, 3] describe several of the effects which have become increasingly important in therapeutic applications of medical ultrasound. Of primary interest at that time were effects involving the heating of a medium, the movement of particles within a medium, and the acceleration of chemical reactions. The most recent studies of high-intensity focused ultrasound (HIFU) as a means of medical therapy are largely motivated by what are potentially substantial advantages as compared to conventional surgery. HIFU offers a non-invasive surgical alternative (it is not necessary to physically enter the body as in conventional surgery) which, when coupled with ultrasound, magnetic resonance, or possibly other imaging techniques, offers the potential for a complete, non-invasive diagnostic and therapeutic system [4–7]. Common clinical applications of HIFU involve the destruction of a volume of tissue, an effect described as tissue necrosis. This ability to affect a volume of tissue, for either non-invasive destruction of internal tissue [8] or cauterization in conjunction with an invasive, conventional procedure [9], is a distinct advantage over alternative methods which only treat a surface.

The desired HIFU effect is often thermal, where acoustic energy deposited in tissue generates a temperature rise [10–14]. Fry, motivated by the desire to measure absolute pressure levels and acoustic absorption coefficients in liquid media, used a conservation of energy argument to predict the temperature rise due to short pulses of ultrasound [15, 16]. Fry's work ignored the effects of

heat conduction. Parker, concerned with the acoustic absorption coefficients in biological tissue in particular, extended Fry's work to include the effects of heat conduction [17,18].

This temperature rise, when sufficiently high (on the order of 60°C for 1 sec or more), can in turn lead to the intended destruction of a volume of tissue, such as a cancerous region in the body [8]. A HIFU-induced temperature rise occurs due to the high acoustic absorption of tissue [19] at megahertz frequencies . Energy from the incident acoustic field is absorbed and is subsequently manifested as a temperature increase whose magnitude is a function of the physical properties of the medium (*e.g.*, acoustic absorption, density, specific heat), properties of the focused ultrasound device (*e.g.*, beam geometry), and the frequency and time-averaged acoustic intensity of the acoustic field [17,20].

Other effects can occur as well. Acoustic cavitation occurs when acoustic pressures generate sufficient tension to "tear" a liquid apart, forming gas or gas and vapor filled cavities [21,22], where "sufficient" depends primarily on the tensile strength of the fluid and any impurities and inhomogeneities in the liquid. Acoustic cavitation activity is typically categorized based on the nature of the effect the sound field has on the cavities: either violent or gentle [23]. A bubble or cavity which oscillates moderately, though potentially nonlinearly, and may exist for several oscillations or acoustic cycles, is referred to as non-inertial (or sometimes stable) cavitation. Noninertial cavitation has also been termed gaseous cavitation because the dynamics are dominated by the compressibility of the gas in the cavity [24]. Alternatively, the phenomenon wherein a bubble oscillates violently, often expanding to greater than twice its equilibrium radius, and at times lasting for only one cycle is referred to as inertial (and occasionally transient) cavitation. This occurs when the collapse is dominated by the inertia of the in-rushing liquid; the gas plays a minor role [24]. Since Fry *et al.* [25] reported on cavitation effects *in vivo* in frogs, several authors have reported evidence of cavitation activity both *in vivo* [25–28] and *in vitro* [1,28,29], and related biological effects such as nerve paralysis [25] and increased tissue hyperthermia [1,27,29].

Most often, acoustic cavitation due to focused ultrasound in medical therapy is considered deleterious, for cavitating bubbles can cause significant mechanical damage to tissue in a region outside the treatment area, or excessive damage within the treatment area [30,31]. In addition, large num-

bers of bubbles can shield the incident pressure field, thereby inhibiting the intended therapeutic effect [20]. A notable exception is lithotripsy, where inertial cavitation bubbles are considered significant contributors to the desired treatment [32]. In addition Fry, *et al.* [28] described the potential positive use of ultrasound-induced cavitation for the elimination of gallstones, and as an aid to therapy by using the generated bubbles as a means of detecting the desired treatment area.

An area that has received some recent attention involves enhanced heat deposition in the presence of cavitation activity. As mentioned above, a focused ultrasound source will generate localized heating at the focus as a result of the tissue absorbing incident acoustic energy, and produce a measurable temperature rise in that tissue. However, several researchers have reported temperature levels in tissue and tissue mimicking phantoms beyond what can be attributed to absorption of the primary acoustic field, in some cases with supporting evidence for the existence of bubbles, at or near the focus of the ultrasound source.

Lele *et al.* reported an increase in the acoustic absorption coefficient, inferred though higher than expected temperature measurements in calf liver *in vitro*, above a threshold intensity of approximately 1500 W/cm^2 [29]. Measurements were made for 0.2 and 0.3 second cw-insonation times at 2.7 MHz. These experiments also included the measurements of acoustic emission from within the samples. From the subharmonic and broadband acoustic emission detected, they concluded that the increased absorption coefficient was due to the occurrence of cavitation activity.

Hynynen, in a study of the threshold for transient cavitation in dog's thigh muscle *in vivo*, reported enhanced temperature elevation in conjunction with both measurements of subharmonic emission and enhanced echogenicity in ultrasound images [27]. Measurements were made between 0.246 and 1.68 MHz for a 1 second cw insonation duration. The results indicated a threshold for enhanced heating as a function of frequency of 5.3 MPa/MHz. Hynynen also concluded that acoustic cavitation led to the increased temperature response.

Watmough *et al.* observed an increased temperature response in a bovine hide gelatine material where gaseous inclusions were introduced into the sample [33]. For measurements at 0.75 MHz with an intensity of 1 W/cm^2 and a cw insonation duration of 1 s, they observed temperature increase of

as much as 6 times between a sample with and without degassing. They concluded the enhanced heating was the result of microbubbles trapped at the inclusions in samples that were not degassed.

Fujishiro *et al.* reported an increase in the measured temperature rise in beef samples by a factor of 1.7 in the presence of a contrast agent (microbubbles), as compared to control samples [34]. Measurements were made at 1.5 MHz with an intensity of 0.9 W/cm^2 and a cw insonation duration of 3 minutes. An equivalent temperature rise, in the absence of the contrast agent, required a doubling of the intensity to 1.8 W/cm^2. The authors concluded that contrast agents could be used to enhance the thermal effects of ultrasound.

Holt and Roy observed an enhanced temperature effect in measurements of temperature in a tissue-mimicking phantom material at 1 MHz for insonation times between 0.5 and 10 seconds [1]. They report an acoustic pressure threshold for a large increase in the temperature rise during insonation that is a function of insonation duration and the dissolved gas concentration in the phantom. Viscous dissipation and acoustic emission from the bubbles are discussed as possible bubble heating mechanisms. By estimating of the thermal power generated by these mechanisms, the authors conclude that on the order of 100 bubbles could account for the enhanced temperature effect.

Other researchers have attempted to model heat generation from bubble activity in diagnostic and therapeutic applications. Wu modeled the effect of a suspension of contrast agents (microbubbles) on the total temperature rise from ultrasound for diagnostic parameters (3.5 W/cm^2 at 1 MHz) [35]. By treating the contrast agents as an effective medium with an increased absorption coefficient with respect to the surrounding medium, he noted a temperature rise of a few degrees at these diagnostic levels.

Hilgenfeldt *et al.* modeled the energy deposited from bubbles at contrast agent related sizes as a result of viscous dissipation and acoustic emission from the bubbles again at pressures, frequencies, and pulse waveform shapes relevant to diagnostic ultrasound [36, 37]. They reported strong absorption of the radiated sound by the surrounding blood resulting in temperature elevations of as high as 100 K for an acoustic pressure amplitude of 3 MPa and a 3 cycle pulse with a center frequency of 3 MHz and a gaussian envelope. They conclude that nonlinear bubble dynamics, sound

absorption, and the resultant heating must be considered with respect to ultrasound and contrast agents in diagnostic applications.

Chavrier *et al.* investigated the effect of acoustic emission from bubbles and the subsequent absorption of that sound and its effect on lesion development [38]. They modeled the behavior of air filled bubbles in water, and used the resulting emitted sound to develop a "global attenuation coefficient" to be used in solving a heat transfer equation for the temperature rise in a tissue mimicking phantom, and the resulting lesion development. This temperature rise was then used to predict the lesion formation in a phantom. Their results indicate that the presence of bubbles can significantly affect the magnitude and location of the temperature change, and consequently the lesion formation.

Of interest in this research is whether an enhanced heating effect due to bubble activity can be exploited to yield the temperature elevation required for tissue necrosis or cauterization at intensities lower than standard practice currently demands. Ideally, time-average acoustic intensities would be kept low enough such that biologically substantial temperature changes occur only at the focus of the source, where an irreversible or medically harmful change would be considered biologically substantial. However, a desired temperature rise at a particular location, relying solely on direct absorption, may require intensities that have an effect in the propagation path. With lower acoustic intensities and an enhanced heating effect at the focus, there is less chance of unwanted heating outside the region of treatment area.

Cavitation may be induced with high *instantaneous* intensities yet low time-average intensities. This could potentially allow for bubble related heating effects at relatively low time-average intensities by lowering the pulse duration for a fixed pulse period. In addition, problems such as mechanical damage and bubble shielding may be mitigated in situations where the cavitation field (amount of cavitation activity, type of cavitation activity) can be "tuned "to provide just the right amount of bubble activity required for the enhanced heating effect, but not more. This latter feature may require some form of feedback control, using a cavitation detector or heat detector as a sensor.

In an effort to better understand the possible benefits of a localized enhanced heating effect due to cavitation activity we have undertaken a series of *in vitro* experiments and numerical simulations

designed to ascertain the answers to crucial questions such as: Are bubbles in fact a contributing factor to enhanced heating? If so, what are the dominant mechanism(s) for heat deposition from bubbles in tissue or tissue mimicking materials at therapeutic ultrasound frequencies? How do parameters such as bubble size, acoustic pressure, and pulse duration affect these mechanisms, and in turn, the rate of temperature rise and maximum temperature achieved?

Different models which account for heating in tissue due to the direct absorption of the incident ultrasound field are discussed in Chapter 2. It is also noted where these models break down with respect to experiments that seem to indicate the presence of additional heating mechanisms. The experiments described in Chapter 3 address the question: does cavitation play a role in enhanced heating? The results indicated a strong correlation between more than just the occurrence of enhanced heating and the occurrence of observable cavitation activity. We also study the effect of insonation duration on the onset pressure and magnitude of the temperature change in the enhanced heating effect. Having found experimental evidence supporting a correlation between these two effects, numerical simulations were designed to establish the relative importance of candidate bubble heating mechanisms. Potentially important mechanisms such as the re-emission of sound and viscous absorption are discussed in Chapter 4, and the results are examined over a range of values for initial bubble size and medium viscosity in Chapter 5. A summary of results and concluding remarks are presented in Chapter 6.

In summary, the work presented in the dissertation is intended to enhance our understanding of the physical mechanisms involved in ultrasound hyperthermia. The mechanism investigated, beyond the direct absorption of sound, is cavitation activity. Experimental work using controlled tissue mimicking phantoms provides a means for correlating the effects of cavitation and ultrasound hyperthermia. It also provides insight into the relative importance of parameters not readily measured, such as bubble size. Numerical solutions compare the significance of potential bubble heating mechanisms, also as a function of bubble size. It is hoped this understanding may lead to more efficient or new and unique applications of therapeutic ultrasound.

Chapter 2

Ultrasound Hyperthermia

In this chapter we consider the heating of tissue due to high-intensity focused ultrasound. As an acoustic disturbance passes through an absorbing medium, energy is deposited, the physical manifestation of which is a temperature change [10–14]. The temperature change in tissue due to any source of heat deposition can be readily determined from the conservation of energy. Sources of heat generation may range from internal metabolic factors to external influences (*e.g.*, ultrasound pressure fields). As a result, several authors have reported the results of tissue heating models of varying complexity and accuracy. This variance is largely due to differences in the level of detail considered in the energy balance equation (*e.g.*, is conduction is included), the geometry under consideration (*e.g.*, whether symmetry can be taken advantage of), and whether an analytic solution to the resulting differential equation is desired. The conservation of energy in a homogeneous conducting medium is described by the following equation which will serve as the basis for the analysis in this chapter:

$$\overbrace{\rho C \frac{\partial T}{\partial t}}^{\text{Thermal Inertia}} = \overbrace{K \nabla^2 T}^{\text{Conduction}} + \overbrace{q}^{\text{Source Term}}, \tag{2.1}$$

where ρ, C, and K are the density, specific heat and thermal conductivity of the medium respectively. All sources of energy deposition are represented by a generic source term (energy per unit time and volume or simply power density), q.

Fry *et al.* developed a thermal model concerned exclusively with the effects of ultrasound, ig-

noring conduction and various biological effects [25]. An example of a biological effect would be heat transfer between tissue and small blood vessels as a result of perfusion. Parker has since extended this model to include the effects of conduction in one or two dimensions with the constraint of cylindrical symmetry [17, 18]. He provides analytic solutions at the expense of additional simplifying assumptions involving the material properties, the geometry of the ultrasound source and additional factors discussed in subsequent sections.

In the absence of external influences such as an applied ultrasound field, a minimum description of the transient temperature field in the human body would include conduction, heat transfer due to perfusion, and metabolic heat generation. Such a model was first proposed by Pennes [39]. This model has since been modified by several authors to include the effects of ultrasound as a source of energy deposition [40–42]. To maintain flexibility in material properties, material geometry, and ultrasound source geometry, standard finite difference time domain (FDTD) techniques have typically been employed to calculate a solution. Implemented in this manner, the Pennes model has proven to be accurate through comparison to experiments with an incident ultrasound field [40].

For the purposes of this research, tissue-mimicking phantoms which lack blood vessels and non-acoustic sources of internal heat generation are used for experimental work and are modeled for comparative numerical analysis. Under these circumstances, the analytic models by Fry and Parker may provide suitable estimates and are examined here as a possible method of predicting temperature changes. A more accurate approach involves using a modified Pennes equation that excludes the effects of perfusion and metabolic heat generation, but includes heat conduction in all dimensions, and allows generalized material properties and an ultrasound source geometry consistent with the experimental work. The result is a relatively simple experimental arrangement (described in Chapter 3) and related model which can readily implemented (a procedure that is discussed in Chapter 5).

In general, temperature predictions can be divided into two time domains, during and after in-

sonation:

$$T(t) = \begin{cases} T_I(t) & 0 < t < t_i, \\ T_C(t) & t > t_i, \end{cases} \tag{2.2}$$

where T_I is the temperature during insonation, T_C is the temperature after insonation as the medium cools, and t_i is the insonation duration. When the effects of conduction are included, Eq. 2.1 is most readily solved analytically *after* insonation when the source term is absent, provided an initial temperature distribution at the end of insonation is known. Several authors have taken advantage of this fact to solve for the temperature decay after insonation as a first step. That result is then used to solve the more complicated problem of the temperature during insonation, in particular with conduction included.

In the remainder of this chapter, analytic solutions to simplified heat transfer models will be presented. This discussion will be followed by a more comprehensive, less restrictive heat transfer model to be solved numerically in Chapter 5. Finally, a comparison of a small set of experimental results with solutions to the numerical implementation will be presented to illustrate the applicability of this model. These results will demonstrate the accuracy of a modified Pennes equation for a large range of values for acoustic intensity and insonation duration. However, for certain ranges of parameters there exists a substantial discrepancy. The existing model breaks down because it only considers the direct absorption of the incident acoustic field and neglects what will be shown to be substantial contributions from cavitation related mechanisms.

2.1 Linear Rate of Heating

Early attempts to relate the temperature change in tissue to energy deposition from an incident ultrasound field by Fry *et al.* were motivated largely by the desire to determine (1) absolute pressure levels and (2) acoustic absorption coefficients by measuring this temperature response [15, 16, 25]. The temperature change in a non-conducting medium used by Fry from consideration of Eq 2.1 is

$$\rho C \frac{\partial T}{\partial t} = q, \tag{2.3}$$

where the change in temperature is directly proportional to the energy deposition, q. Fry and subsequent authors approximate the energy deposition per unit volume and time due to ultrasound as [17,18,20]

$$q_{us} = 2\alpha I_0, \tag{2.4}$$

where α is the acoustic absorption coefficient and I_0 is the spatial-peak, time-averaged acoustic intensity at the focus of the acoustic source. Equation 2.4 assumes a mono-frequency, plane wave acoustic field at the focus. A complete derivation of this approximation is provided by Pierce [12]. Equation 2.3 is readily solved with a constant power density, such as Eq 2.4, to predict the temperature as function of time during insonation

$$T_I(t) = \frac{2\alpha I_0}{\rho C} t, \quad t < t_i, \tag{2.5}$$

where t_i is the insonation time. Eq 2.5 represents the *linear rate of heating* characteristic of short insonation times. Fry's model clearly ignores the effects of perfusion, metabolic heat generation, and other biological influences. More importantly, this result is only valid when conduction in the tissue is not a factor, *i.e.*, for insonation times which are much less than the thermal diffusion time. Tissue mimicking materials, such as those used in this research, often lack a network of vessels and sources of internal heat generation. However, for the insonation times and thermal properties discussed in Chapter 3, neglecting heat conduction may introduce a substantial error.

2.2 Heat Conduction

To predict the rate of heating during insonation and the subsequent temperature decay for a wide range of parameters involving insonation time and material geometry, Parker extended Fry's work to include the effects of heat conduction in one and two dimensions [17,18]. The models are not concerned with the physical ultrasound source, nor the propagation of sound, but assume that the focal region of highest intensity has cylindrical symmetry and is thin with respect to the axial direction, as shown in Fig. 2.1. In addition, a Gaussian radial profile is assumed for the acoustic

intensity

$$I(r) = I_0 e^{-r^2/b}, \tag{2.6}$$

where b is a measure of the Gaussian variance of the intensity field.

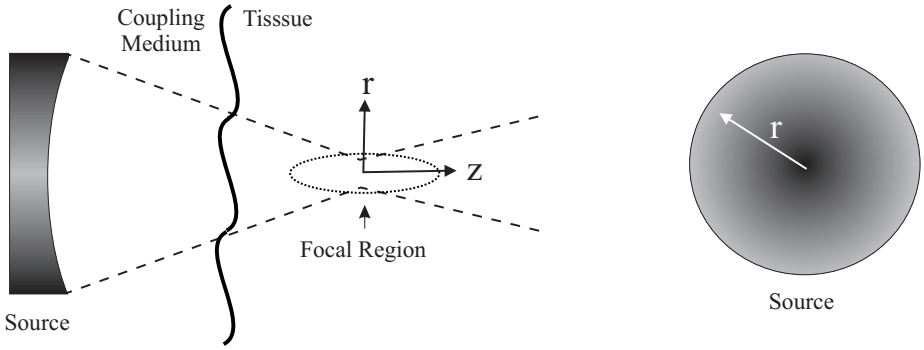

Figure 2.1: Parker model geometry.

2.2.1 Temperature Decay

Initial work by Parker considered only a short ultrasound impulse with conduction neglected (linear rate of heating) followed by a longer temperature decay where conduction is considered. The temperature is assumed to have the same spatial shape of and to be proportional to the acoustic intensity field at the end of insonation. This initial condition for the decay portion of the problem is simply

$$T_C(r, 0) = T_{max} e^{-r^2/b}, \tag{2.7}$$

where T_C is again the temperature during cooling and time is referenced from the end of insonation. T_{max} is the peak temperature at the end of insonation and is proportional to the intensity, I_0. Specifically, T_{max} can be based on Fry's result for the nonconducting medium (Eq. 2.5) and is thus given by the temperature achieved assuming a linear rate of heating

$$T_{max} = \frac{2\alpha I_0 t_i}{\rho C}, \tag{2.8}$$

where t_i is again the insonation time.

Given the initial condition in Eq. 2.7, the temperature decay is determined from the conservation

of energy, Eq. 2.1, including the effects of conduction, but absent any source term:

$$\rho C \frac{\partial T}{\partial t} = K \nabla^2 T, \tag{2.9}$$

One Dimensional Conduction

When considering one dimensional conduction only, Parker's model assumes cylindrical symmetry and the acoustic energy deposition is approximated as a line source along the transducer's axis of symmetry. As a result, conduction in the axial direction is ignored. This problem has been solved for the same geometry where, rather than an initial temperature distribution, the initial condition is an instantaneous heat source, Q at time $\tau = 0$ [43]. This solution is well documented by both Parker and Lele and consists of matching the initial condition described in Eq. 2.7 to that of the instantaneous heat source condition, which also has a Gaussian shape. In particular, the solution shown by Lele is [43]

$$T(r, \tau) = \frac{Q}{4\pi\kappa\tau} e^{-r^2/4\kappa\tau}, \tag{2.10}$$

where κ is the thermal diffusivity. This will match the initial condition of Eq. 2.7 for a time and magnitude of

$$\tau_0 = \frac{b}{4k}, \tag{2.11}$$

and

$$Q_0 = \pi T_{max} b, \tag{2.12}$$

respectively.

For time, t, corresponding to the time after insonation, the solution to Eq. 2.10 is shifted in time such that

$$t = \tau - \tau_0 \tag{2.13}$$

and the result for post-insonation cooling, as a function of radial distance and time becomes

$$T_C(r, t) = \frac{T_{max}}{(4\kappa/b)\, t + 1} e^{-r^2/(4\kappa t + b)}. \tag{2.14}$$

Two Dimensional Conduction

Parker also incorporated the effects of axial conduction [18], the result of which is the following equation for the temperature decay after insonation:

$$T(r,z,t) = \frac{T_{max}}{(4\kappa t/b)+1} e^{-r^2/(4\kappa t+b)} \left(\text{erf}\left(\frac{z}{4\kappa t}\right)\right). \tag{2.15}$$

The details of this derivation are not addressed in this work; the solution is presented here only for completeness. For conduction in multiple directions, the analytic solution is retired in favor of a numerical model with greater flexibility in material and beam properties.

2.2.2 Rate of Heating With Conduction

Equation 2.14 represents the temperature response after insonation, where the peak temperature is determined from the linear rate of heating. As the linear rate of heating represents the response for very short insonation times, it can be thought of as the impulse response of the medium to a burst of ultrasound. As such, it can then be used to determine an analytical solution for the rate of heating during a longer insonation with *one dimensional* conduction included as a function of the beam shape. This is accomplished by convolving Eq. 2.14 with a unit step function [18, 44, 45]:

$$T_I(r,t) = \int_0^t \frac{2\alpha I(r)}{\rho C\,[1+(4\kappa t/b)]} d\tau. \tag{2.16}$$

Equation 2.16 is readily solved for the temperature on axis, $r = 0$:

$$T_I(0,t) = \frac{2\alpha I_0}{\rho C}\left(\frac{b}{4\kappa}\right)\ln\left(1+\frac{4\kappa t}{b}\right) \tag{2.17}$$

which for $4\kappa t/b \ll 1$ reduces to Fry's result, as expected.

Equations 2.14 and 2.17 have been shown by Parker to provide suitable estimates given the assumptions specified in the derivations. However, a more rigorous model which includes two dimensional conduction (independent of the source shape and size) and, in general, a more accurate representation of the source and material geometry will be necessary when comparing to experimental results. The experimental conditions discussed in Chapter 3 are similar to but do not exactly

match the assumptions in the analytical model. This additional accuracy and flexibility can be found in a numerical solution to a more complete formulation of the conservation of energy equation.

2.3 Pennes Bioheat Transfer Equation (BHTE)

The Pennes bioheat transfer equation (BHTE) is a highly utilized linear model for heat transfer in the human body [39,41,46,47]. Pennes' motivation for developing this model was purely biological and as such did not include any external influences, including energy absorption from ultrasound. The general equation proposed by Pennes is

$$\rho_t C_t \frac{\partial T}{\partial t} = K_t \nabla^2 T - W_b C_b (T - T_a) + q_m, \tag{2.18}$$

where T is the temperature of the tissue, ρ_t, C_t, and K_t are the density, heat capacity, and conductivity of the tissue respectively, C_b and W_b are the heat capacity and perfusion of the blood respectively, T_a is ambient arterial temperature, and q_m represents metabolic heat generation.

This model has been shown to be fairly accurate under many circumstances [41,46]. Most inaccuracies concern heat transfer between tissue and small blood vessels and therefore are associated with the perfusion term [46,48]. As a result, they are not important to this research which does not utilize a vessel network either experimentally or theoretically. Therefore the appropriate BHTE is

$$\rho_t C_t \frac{\partial T}{\partial t} = K_t \nabla^2 T + q_m. \tag{2.19}$$

Here the power density source term is now metabolic rather than acoustic. However, by solving the equation numerically rather than relying on analytic solutions, the assumptions made by Parker and Fry are not necessary.

2.3.1 Ultrasound Induced Temperature Changes

Several authors have since supplemented or replaced the metabolic heat generation term with one representing the absorbed energy from an incident ultrasound field [40–42]. A straightforward implementation for this acoustic source term is to use Eq. 2.4 in the same manner as Fry and Parker.

Alternatively, Pierce [12] provides a more accurate description of the power dissipation per unit volume in a thermoviscous fluid:

$$q_{us} \approx \frac{2\alpha}{\rho c \omega^2} \left(\frac{\partial p}{\partial t} \right)^2, \tag{2.20}$$

where α is the absorption coefficient, ω is the acoustic source frequency, c is the speed of sound in the material, and p is the acoustic pressure. Energy deposition described by Eq. 2.20 will be referred as the *primary absorption* when discussing ultrasound related heating mechanisms as it represents the direct or primary absorption of energy from the incident pressure field.

If the BHTE is solved numerically for the purpose of reducing simplifying assumptions, the pressure field, p in Eq. 2.20 is best determined numerically as well. This can be accomplished by solving the wave equation over the same domain of interest as the BTHE solution. The particular form of the equation chosen is a nonlinear absorbing wave equation for quiescent fluids. A derivation of this equation is presented by Hallaj [49] and is related to the Westervelt [50] equation with the addition of losses due to thermal conduction and viscosity:

$$\nabla^2 p - \frac{1}{c^2} \frac{\partial^2 p}{\partial t^2} + \overbrace{\frac{2\alpha}{c\omega^2} \frac{\partial^3 p}{\partial t^3}}^{(1)} + \overbrace{\frac{\beta}{\rho c^4} \frac{\partial^2 p^2}{\partial t^2}}^{(2)} = 0, \tag{2.21}$$

where p is the acoustic pressure, c is the speed of sound, ω is the frequency, α is again the absorption coefficient, and β is the nonlinearity coefficient. Specifically term (1) represents losses due to thermal conductivity and viscosity while term (2) represents the nonlinearity in the governing continuity equation and equation of state. Inserting Eq. 2.20, as determined from Eq. 2.21, into the Pennes model yields

$$\rho_t C_t \frac{\partial T}{\partial t} = K_t \nabla^2 T + \frac{2\alpha}{\rho c \omega^2} \left(\frac{\partial p}{\partial t} \right)^2. \tag{2.22}$$

2.4 Temperature Predictions

In this section we take a qualitative look at the results of Fry and Parker's analytical models as well as numerical results from the modified BHTE. Only general information sufficient for a basic understanding of the discussion is presented here. A full explanation of the numerical solution will

be presented in Chapter 5. In addition, the material properties and the experimental setup (source and tissue phantom parameters and geometry) are detailed in Chapter 3. First, a sample heating and cooling curve is shown in Fig. 2.2 as predicted by the BHTE. Temperature and time have been normalized to the peak temperature and insonation time respectively so as to provide a qualitative look at the typical form of the curve.

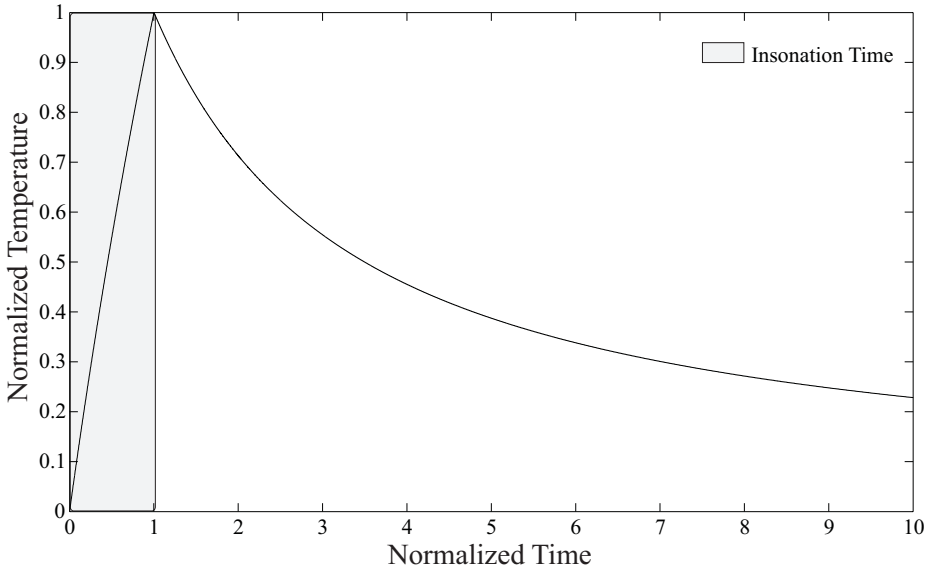

Figure 2.2: Sample temperature response as a function of time as predicted by the BHTE. Shading indicates the time the acoustic source is turned on (insonation time).

Figure 2.3 shows the calculated peak temperature change at the focus of the acoustic source, as a function of insonation duration using models by Fry, Parker, and the modified BHTE. The peak positive acoustic pressure at the focus for all calculations is 0.75 MPa and the acoustic source frequency is 1 MHz. Table 2.1 lists the tissue material properties used by all models. These values are consistent with measurements of the tissue phantom materials used in Chapter 3. For the BHTE solution, the geometry of the experimental arrangement discussed in Chapter 3 is modeled as accurately as possible. In those experiments, a portion of the propagation path between the acoustic source and the focus contains not only the tissue phantom, but water as well (similar to the geometry seen in Fig. 2.1). Therefore, the applicable properties of water are also listed in Table 2.1.

Given these parameters and a beam geometry with $\beta = 1.0 \times 10^{-6}\,\mathrm{m}^2$, the measure of the relative importance of conduction, $4\kappa t/b$, ranges from 0.0632 for 0.1 second insonation to 6.32 for a 10

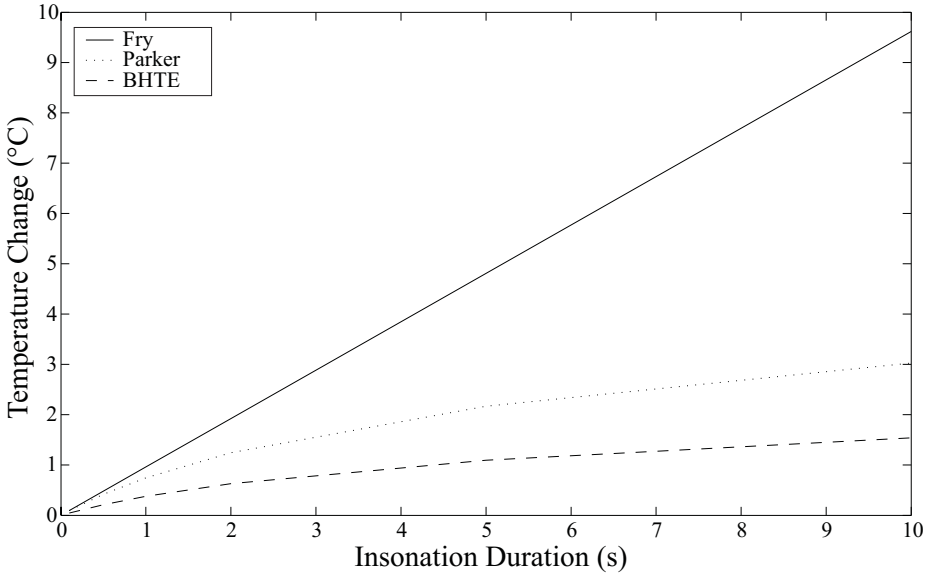

Figure 2.3: Predicted peak temperature change for three models as a function of insonation duration. Material properties are those of a tissue phantom.

second insonation. As a result, conduction in the radial direction cannot be ignored for much of this range, and a substantial discrepancy should be expected between the Fry and Parker models and is evident in Fig. 2.3. In addition, it provides some indication of the relative importance of conduction in the axial direction for a finite length focal region. Neglecting axial conduction and the additional assumptions described for the Parker model yields higher temperature values with respect to the BHTE solutions as well.

Differences in these models will be affected by the acoustic pressure amplitude as well. Figure 2.4 shows the peak temperature change as a function of peak negative pressure amplitude at the focus for the same three models. The insonation duration is 2 seconds. Given that each model is effectively scaled by the acoustic pressure squared, the difference in predicted values between models grows approximately quadratically with increasing pressure as well.

2.4.1 Comparison With Experiment

As was mentioned previously, the BHTE has been shown to be accurate in several experimental comparisons where the source of energy deposition is a focused ultrasound source. Chapter 3 will present results for several experiments designed to measure temperature changes in a tissue

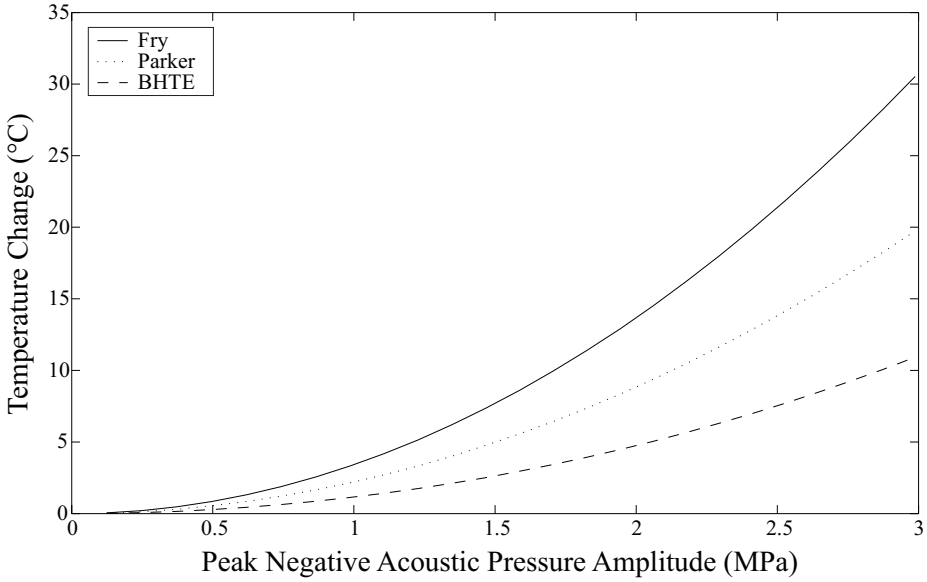

Figure 2.4: Peak temperature change for three models as a function of increasing peak negative acoustic pressure amplitude.

Material Property	Tissue	Water
Density (kg/m^3)	1003	1000
Sound speed (m/s)	1588	1500
Absorption (Np/m/MHZ)	5.066	n/a
Absorption (Np/m/MHz^2)	n/a	0.0253
Thermal diffusivity (m^2/s)	0.158×10^{-6}	n/a
Specific heat (J/kg·°C)	3710	n/a

Table 2.1: Material properties used in the three models presented in this section. The properties of water are required to calculate the pressure for the BHTE. Note that the absorption of tissue and water vary differently as a function of frequency.

mimicking phantom. However, examining a few general results here will be useful in understanding the limitations of the BHTE and in motivating the specific experimental goals discussed in the next chapter.

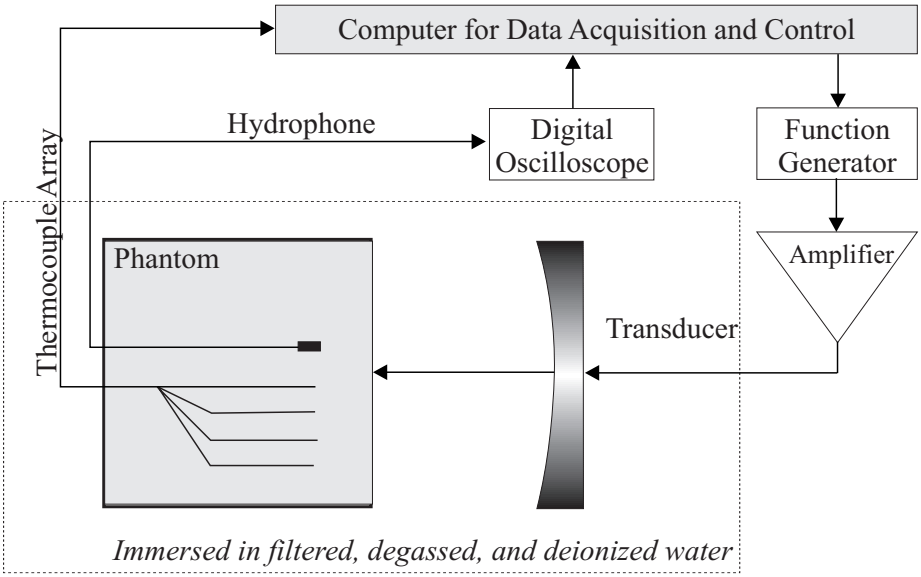

Figure 2.5: Example experimental apparatus for temperature measurement in a tissue phantom. The tissue phantom is instrumented with thermocouples and optionally a hydrophone [1].

An overview of the experimental apparatus is shown in Fig. 2.5, which is derived from similar experiments performed by Holt and Roy [1]. An ultrasound source and a tissue-mimicking phantom are immersed in filtered, degassed, and deionized water. For the results presented in this section, the phantom is insonified at 1 MHz for 2 seconds. The tissue phantom is composed primarily of water, agar, and graphite and is constructed with a thermocouple for temperature measurement, and a needle hydrophone for pressure calibration.

Figure 2.6 shows the peak temperature change measured with a thermocouple located 0.5 mm off axis in the focal plane. The results are compared to simulation results from the BHTE solved for geometry and parameters which match the experimental setup, including thermocouple location. These peak temperatures are plotted as a function of the peak negative acoustic pressure at the focus, and represent the average of 10 measurements at each pressure. The error bars for the experimental values show one standard deviation for these 10 measurements.

For the range of pressures plotted in Fig. 2.6 (up to ~1.6 MPa), there is close agreement between

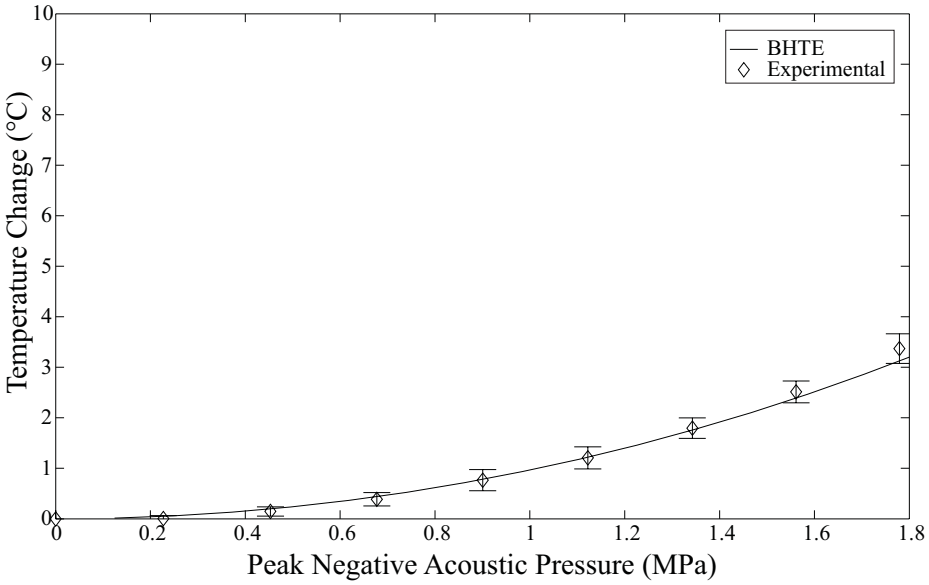

Figure 2.6: Comparison between experimental and numerical (BHTE) temperatures for a 2 second insonation at 1 MHz. Experimental values are averages of 10 measurements where the error bars represent +/- 1 standard deviation of those measurements.

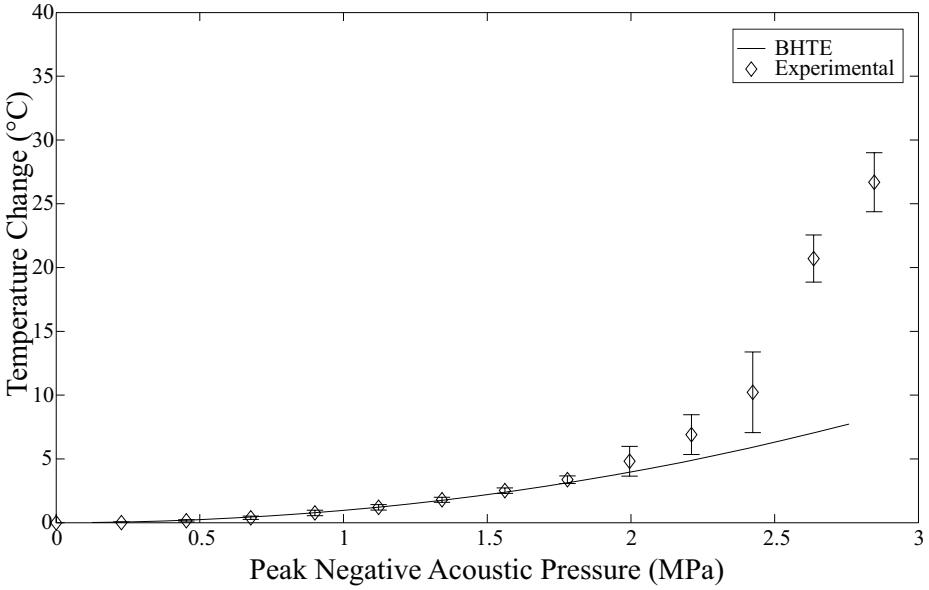

Figure 2.7: Comparison between experimental and predicted temperatures for a 2 second insonation at 1 MHz.

the measured and predicted temperatures. What is not seen in Fig. 2.6 is that there is a substantial deviation from the experimental measurements as the pressure continues to increase. This effect is seen clearly in Fig. 2.7 where peak negative pressures up to 2.8 MPa are plotted.

If we presume for the moment that experimental data is valid, then the discrepancy seen in Fig. 2.7 can be ascribed to one of two factors: (1) there is a fundamental flaw in the BTHE which only becomes apparent above certain pressures or (2) there are one or more physical effects which (a) only occur for certain pressure and (b) are not accounted for in the BHTE. The likely validity of the data is supported by the results of multiple authors presented in the previous chapter. Similarly, there has been substantial agreement between experimental results and the BHTE for a wide range of parameters, as mentioned earlier and seen in this research in Fig. 2.6. In addition, the experimental results show a dramatic change in temperature output, possibly indicative of a similarly dramatic change in the physical mechanisms at work.

As a result, it seems unlikely that there is a fundamental flaw in the BHTE, but rather, that there are effects involved in the region of enhanced heating that are simply not accounted for in that model. In fact, this threshold effect where dramatic changes are observed with a relatively small change in the driving parameter (in this case acoustic pressure) is very consistent with the onset of acoustic cavitation [51–53], an effect that has been associated experimentally [1, 27, 29] and theoretically [36–38] with an enhanced heating effect. The following chapter discusses experiments which are designed to test for a correlation between the onset of both enhanced heating and cavitation activity by simultaneously measuring these effects. Determining a correlation between the enhanced heating effect and cavitation activity will provide the motivation for looking at bubble heating mechanisms in subsequent chapters.

Chapter 3

Simultaneous Measurement of Thermal and Cavitation Activity

The experimental research performed as a part of this dissertation was motivated by three goals:

- To extend experimental results which indicate an "enhanced heating effect" above a threshold pressure
- To demonstrate a definitive link between this enhanced heating effect and acoustic cavitation "activity"
- To understand the effects of experimental parameters such as insonation duration on the properties of the "enhanced heating effect"

To accomplish these objectives, an experimental apparatus was developed that could simultaneously measure the temperature in a tissue-mimicking phantom and record indications of what we will define as acoustic cavitation activity in the phantom as well. By acoustic cavitation activity, or simply cavitation activity, we mean the acoustically forced motion of gas and vapor filled cavities (bubbles) resulting in "a conversion of acoustical to mechanical energy" [54]. The source of this acoustical energy is a high-intensity, focused, ultrasound transducer.

An enhanced heating effect is defined as any temperature rise in the tissue phantom above what is predicted by primary absorption, as described in Chapter 2. Tissue-mimicking phantoms, materials with important acoustic and thermal properties similar to real tissue, are chosen over *in vivo* measurements or measurements obtained using actual tissue samples *in vitro* because of the greater

ease in handling, the ability to precisely and independently control parameters, and the ability to consistently create samples with nearly identical material properties.

Temperature measurement is accomplished with standard thermocouples. Cavitation activity is monitored using a passive cavitation detector (PCD) similar to the one described by Roy *et al.* [55] and Calabrese [56]. Chapter 4 will discuss bubble dynamics and acoustic cavitation in some detail. Until then, the experiments in this chapter can be understood simply by recognizing that bubbles can act as excellent scatterers of acoustic energy, with the additional ability to re-emit sound as they oscillate in response to an incident acoustic pressure field. To exploit these properties, a second, properly positioned ultrasound transducer is used to passively listen for indications of cavitation activity by sensing acoustic emissions related to pulsating bubbles.

This dual capability of the apparatus is important in its ability to simultaneously detect the onset of observable cavitation activity and any changes in the behavior of the temperature rise in the phantom. In addition, these simultaneous measurements can yield information regarding the temperature rise and cavitation activity as a function of parameters such as insonation duration and the gas concentration in the tissue-mimicking phantoms. This information may provide insight into the basic physics of the problem, such as the relevant bubble dynamics and the physical nature of the mechanisms leading to an enhanced heating effect. The results may also lend guidance to eventual clinical applications where optimal operational parameters are of interest.

3.1 Experimental Apparatus

A schematic of the dual measurement apparatus is shown in Fig. 3.1. This is a top view of the primary components of the system. Detailed descriptions of all components are provided in subsequent sections. The experiments are performed in an acrylic tank containing filtered, degassed, and de-ionized water. The apparatus can be conveniently divided into four primary systems or components: (1) sound generation, (2) tissue phantom (3) temperature measurement, and (4) cavitation detection. A fifth component for *in situ* acoustic pressure measurement is optionally included in some experiments.

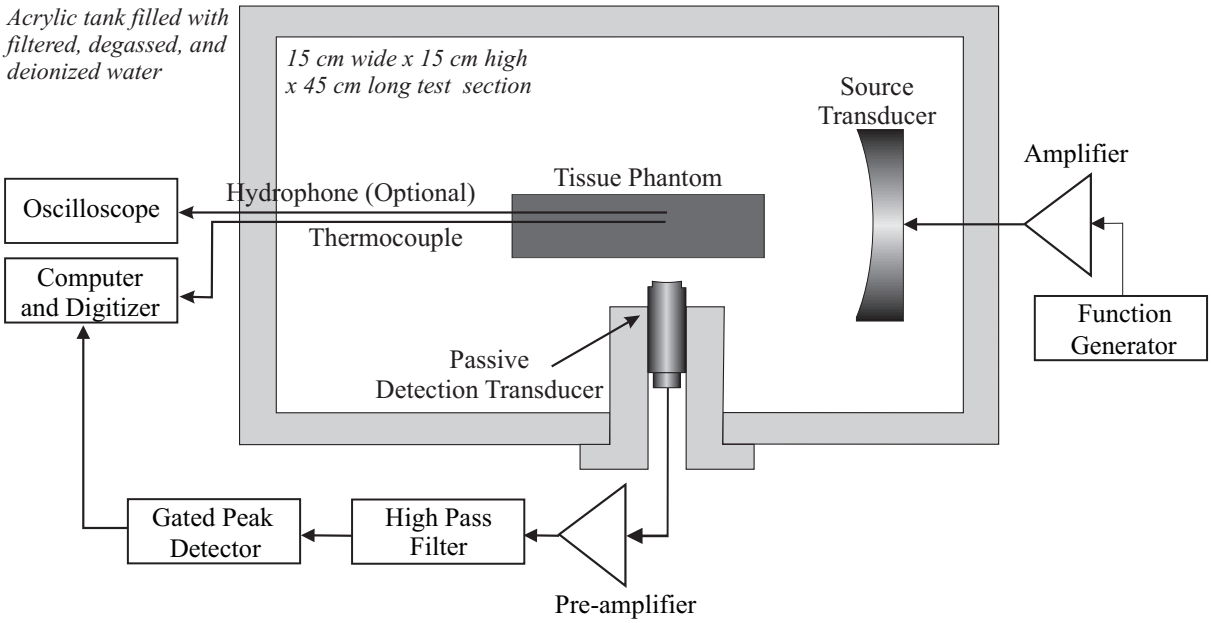

Figure 3.1: Top view of a dual cavitation and temperature monitoring apparatus. A 1 MHz source transducer is used to insonify a submerged tissue-mimicking tissue phantom. A thermocouple is embedded in the phantom to measure temperature and a second transducer is used to passively listen for indications of bubble activity. The phantom is mounted on x-y-z translation slides (not shown) to facilitate precise alignment.

3.1.1 Acoustic Source Generation

The acoustic source is a single element, piezoceramic, spherically focused transducer (H-101, Sonic Concepts, Woodinville, WA) with a 6.24 cm focal length (in water), a 7.0 cm aperture, and a center frequency of 1.1 MHz. A photo of the transducer can be seen in Fig. 3.2. The transducer generates a region of high-intensity ultrasound with a focal width of 1.9 mm and focal depth of 9.0 mm (full-width half-max pressure in the tissue phantom).

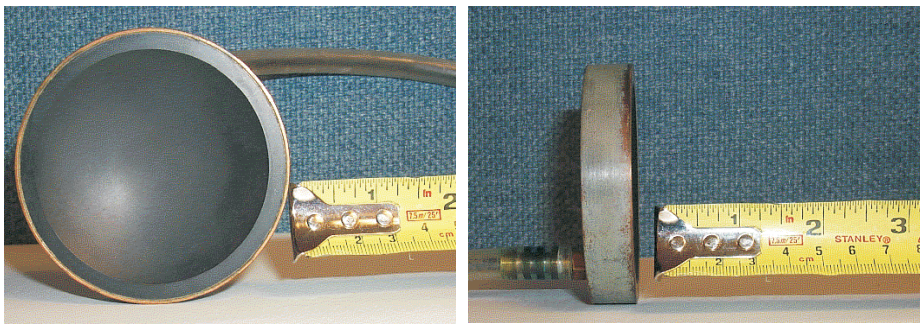

Figure 3.2: Sonic Concepts H-101 transducer. The transducer is spherically focused with a 7.0 cm aperture.

The transverse (with respect to the acoustic axis) beam profiles in the focal plane are shown in

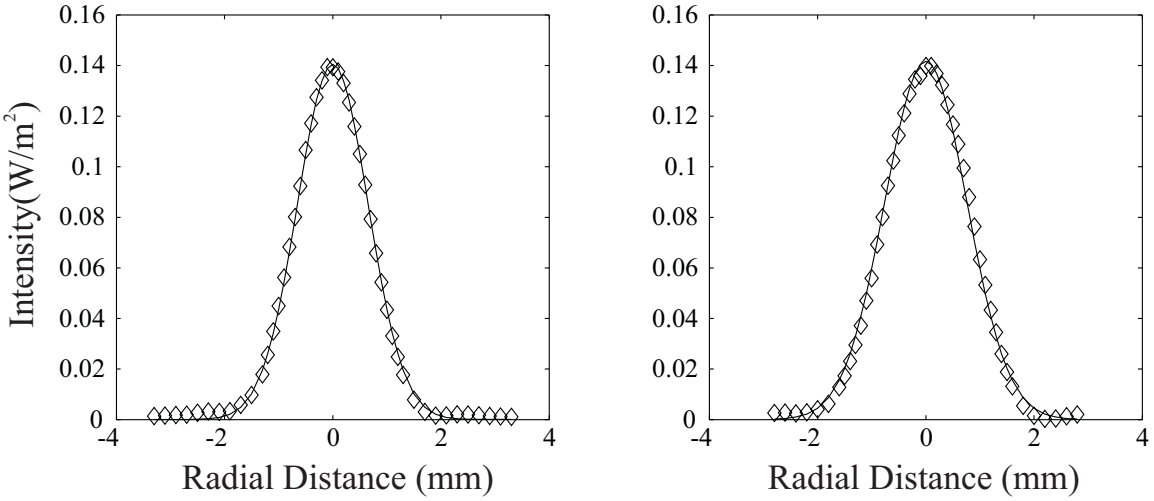

Figure 3.3: H-101 transducer *in situ* radial beam profile at 1 MHz: (a) horizontal (with respect to the apparatus) and (b) vertical intensity profiles in the focal plane. Measured data is represented with symbols and a Gaussian fit to the data is shown as a solid line.

Fig. 3.3. A Gaussian fit is also plotted for each profile. Although the Parker models will not be used, it is worth noting that the radial profile does meet Parker's profile requirement. The radial distance is with respect to the acoustic axis of the transducer. This data is obtained by making *in situ* pressure measurements using a calibrated needle hydrophone (NP-4, 1.0 mm active element, Dapco, Branford, CT). The details of the needle hydrophone and *in situ* pressure measurements are presented in Sec. 3.1.5. A ten-cycle acoustic pulse is generated by the source and measured as a function of location in the phantom. A sufficiently low acoustic pressure amplitude (typically under 0.5 MPa at the focus) was used to ensure a linear acoustic pressure field at the focus. The axial beam profile is shown in Fig. 3.4. The axial distance is with respect to the focal plane of the transducer.

For every experiment performed as a part of this research the transducer was operated at a frequency of 1 MHz. A 1 MHz, sinusoidal input is generated with a function generator (3314A, Hewlett Packard, Palo Alto, CA), this signal is amplified (Model A-150, 55 dB fixed-gain, Electronic Navigation Industries, Rochester, NY), and then delivered through an impedance matching network (Sonic Concepts, Woodinville, WA) designed specifically for this transducer.

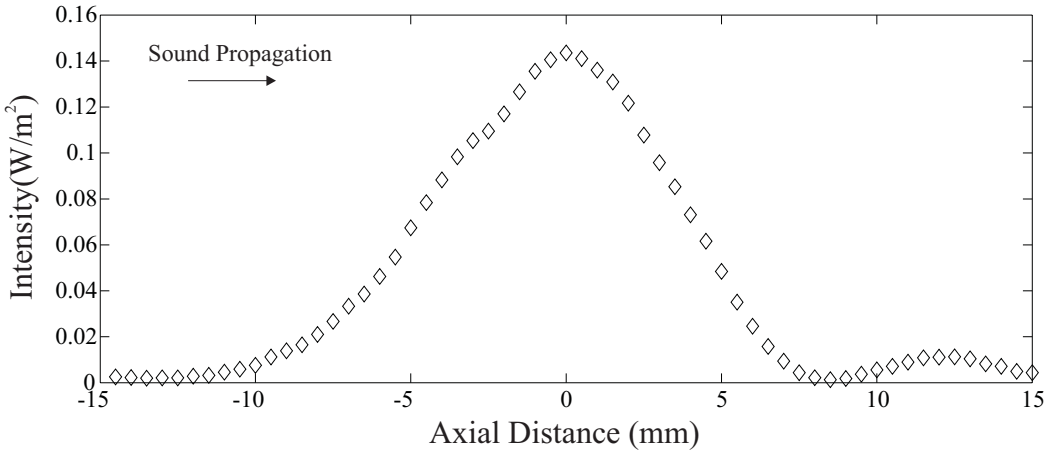

Figure 3.4: H-101 transducer *in situ* axial beam profile: axial intensity profile with respect to the focal plane (0 mm).

3.1.2 Tissue-Mimicking Phantom

The ideal material for experimental studies of ultrasound-induced temperature changes would be the real tissue of clinical interest. Further, *in vivo* experiments would provide the nearest approximation to clinical conditions. However, *in vivo* measurements, and even the use of real tissue *in vitro* can present substantial difficulties in preparation, handling, storage, and use of these materials. More importantly, a rigorous study of the effects of parameters such as insonation duration requires consistency in material properties between multiple samples. Tissue-mimicking phantoms can not only be created with repeatable material properties, but also be formed into any desired shape. The phantom mixtures described in detail below are created as liquids which can be readily poured into a mold, and equally important, poured around objects such as thermocouples or hydrophones which need to be embedded in the phantom. For these reasons, tissue-mimicking phantoms are used exclusively in this research.

The tissue phantom is constructed by first creating an acrylic mold of the desired shape. The mold also serves to support the phantom during experiments. Details of the phantom preparation are described below, however it is important to note here that it is only after several hours of cooling that the material achieves a gel-like consistency. At the time of creation the material is a liquid with a consistency between that of water and honey. In addition, extended exposure to air after solidification dramatically alters the physical properties of the material. As a result, molds

must be designed which, at least for the purposes of casting, are largely liquid-tight, and for storage, must be air-tight. Alternatively the phantoms may be stored in water.

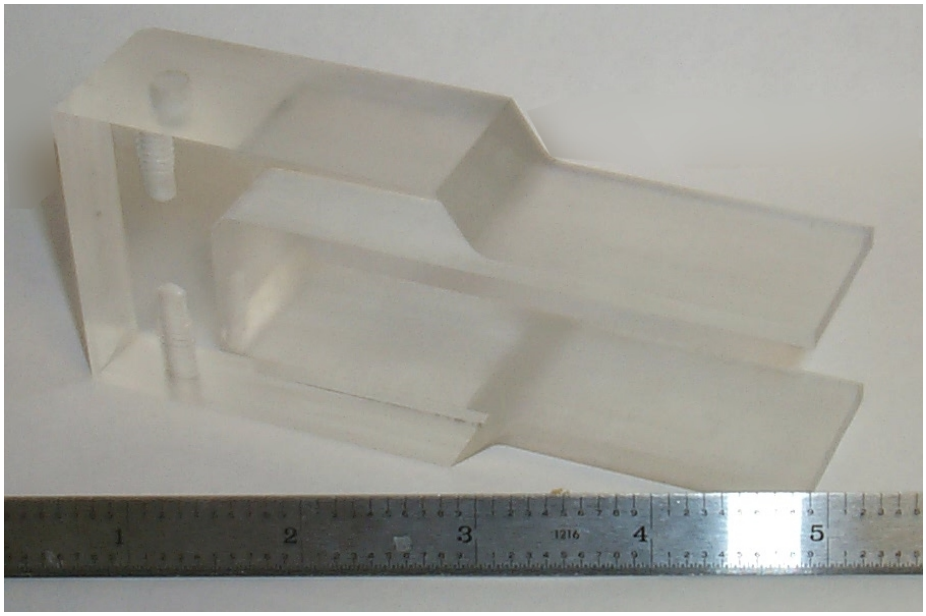

Figure 3.5: An example of a tissue phantom mold/phantom constructed from a single piece of acrylic.

Several criteria influence the shapes and sizes of the molds used. The molds are first designed to minimize the amount of material in the propagation path from the source so as to interfere with the incident sound field as little as possible. Only what is necessary to maintain the shape and integrity of the sample is used. For a similar reason, at least one side is designed to be completely removed to allow exposure to the passive cavitation detection transducer (described below). In addition, the relatively short focal length of the passive cavitation detection transducer limits the thickness of the sample on the side that will be exposed to this transducer. For the experiments described in this chapter, the molds create phantoms which are 2.5 cm x 2.5 cm wide and high and 6.5 cm to 9.5 cm in depth.

Figure 3.5 is a photograph of one example of a phantom mold/holder. Two sides and the front (nearest the acoustic source) face which would be covered when casting the phantom have been removed. This is how the holder with a phantom would be immersed in the tank. A schematic of the general phantom geometry, including typical locations for the hydrophone, thermocouple, and focal plane with respect to the front face of the phantom and the acoustic axis, is shown in Fig. 3.6. The

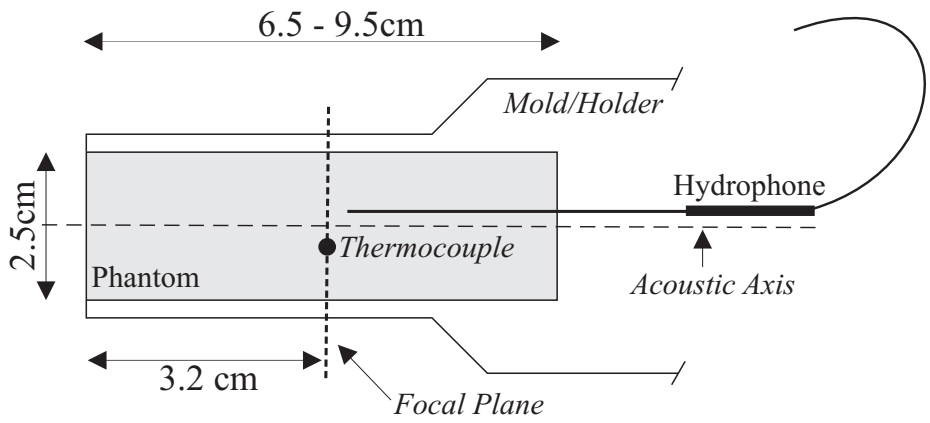

Figure 3.6: Schematic of the phantom and holder indicating the general size and typical locations for the thermocouple and hydrophone.

specific choices for the location of the thermocouple and hydrophone will be addressed in sections dedicated to those instruments. The size of the thermocouple has been exaggerated for illustration purposes.

The phantom material is a mixture of water, graphite (acts as a scatterer), agar, methyl paraben (acts as a preservative), and 1-propanol (adjusts sound speed). The specific quantities of each component depend on the desired properties of the resulting phantom. To create the phantom mixture, water is first heated to a minimum of 80°C. At this point, the remaining materials are added one at a time (agar, graphite, methyl paraben, and lastly 1-propanol). The well-mixed liquid may then be optionally degassed in a vacuum depending on the desired gas concentration, and is finally poured into the mold. Any devices to be embedded in the phantom (*e.g.*, thermocouples and/or a hydrophone) have already been placed in the desired locations in the mold prior to adding the mixture. After approximately 24 hours, the mixture has solidified and reached room temperature. Table 3.1 lists the recipes for the phantoms used in this research. Table 3.2 specifies the measured phantom properties as well as typical values for human tissue for reference [19].

Each phantom property value in Table 3.2 was measured using extra material from phantoms used in experiments. Specific heat is determined using adiabatic calorimetry at room temperature [19, 57], thermal conductivity from a steady-state longitudinal heat flow method [19, 57, 58], and the sound speed and attenuation are found using a through-transmission technique [19].

Component	"Agar-01"	"Agar-02"
Water (g)	600	600
Graphite (g)	80	24
Agar (g)	18	18
1-propanol (ml)	16	16
Methyl Paraben (g)	0.75	0.75

Table 3.1: Agar-based tissue phantom recipes.

Property	Tissue	"Agar-01"	"Agar-02"
Density (kg/m^3)	1000-1100	1005	1003
Sound speed (m/s)	1450-1600	1560	1588
Attenuation (Np/m/MHz)	5.6-17	18.2	5.1
Thermal diffusivity (mm^2/s)	0.105-0.106	0.179	0.158
Specific heat (J/kg·°C)	3600-3900	3300	3710

Table 3.2: Tissue and Agar tissue-mimicking phantom measured physical properties.

3.1.3 Temperature Measurement

Temperature is measured with one or more type-E thermocouples (0.127-mm diameter bare wire, 40 ms response time, Omega Engineering Inc., Stamford, CT) located in the focal plane of the acoustic source, typically 3 cm deep from the proximal face of the phantom, and at various locations in the cross-section. The cross-section locations were chosen based on the number of thermocouples present and the size of the phantom. However, the vast majority of the measurements were made with the thermocouple 0.5 mm off-axis with respect to the acoustic source.

Thermocouples are connected to an isothermal terminal block with cold-junction-compensation (SCB-68, National Instruments, Austin, TX). The terminal block outputs are connected to the analog inputs of a multifunction input/ouput (MIO) computer board (AT-MIO-16XE, 16-bit resolution, 100 kS/s, National Instruments, Austin, TX), and the thermocouple voltages are sampled at 1 kHz. The MIO board sample rate and timing is externally triggered via a signal from the same function generator which drives the acoustic source, a signal that is also connected to the terminal block. Note that this trigger is not specific to temperature measurements, but instead applies to any sampling performed by the MIO board, including measurements described shortly in Sec. 3.1.4. A detailed

schematic of the temperature measurement components is shown in Fig. 3.7.

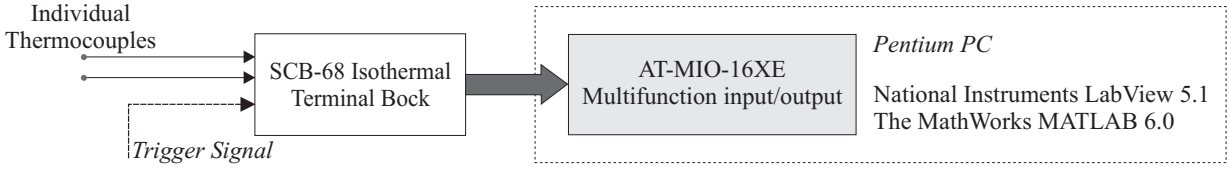

Figure 3.7: Schematic of the temperature measurement components. One or more thermocouples, connected to an isothermal terminal block, are sampled with a multifunction input/output computer board.

The sampled thermocouple voltages are converted to temperatures in software (LabVIEW 5.1, National Instruments, Austin, TX; MATLAB 6.0, The MathWorks, Natick, MA) based on the thermocouple type, and incorporates the cold-junction-compensation reading. At the highest gain, the input range of the MIO board is ± 100 mv, which results in quantized voltage increments of 3.0518 μV given the 16-bit resolution. This minimum voltage increment results in a ideal (*i.e.*, noise free) temperature resolution of $\sim 0.05\ ^{\circ}C$ for type-E thermocouples. There is no averaging or filtering performed, either in hardware or software, when the data is acquired. Section 3.2 examines acquired data to determine the real temperature resolution and noise level, and describes the post-processing steps that may be applied to the stored temperature values during analysis.

3.1.4 Cavitation Detection

Cavitation activity is monitored using a damped, spherically focused transducer (15 MHz center frequency, Panametrics, Waltham, MA) with a 1.9 cm focal length (in water) and a 0.64 cm aperture. The transducer is aligned such that the location of the focus corresponds to the location of the focus of the source transducer. This means the transducer is most sensitive to sound emitted at the location of highest acoustic intensity for the 1 MHz sound field, which is also where cavitation is most likely to occur. The confocal overlay volume for the source and PCD transducers is approximately 4.5 mm^3.

Three types of acoustic information is sensed by the PCD transducer. The first signal is primary path and multiple path (*i.e.*, reverberation) sound generated by the source transducer in the absence of cavitation activity. The second signal will be due to incident sound scattering directly

from bubbles. Both of the signals consist primarily of the 1 MHz source frequency, with potentially a small component of higher frequencies depending on the nonlinearity of the incident field. The latter signal will dominate the former in the presence of cavitation activity because the "bubbles as scatterers" reside in the focal region. The third type of received signal will be due to the active emission of sound from the bubble. Unlike the previous cases, this noise will consist of a range of frequencies at, above, and below the source frequency, based on the motion of the bubble wall. In order to further minimize the masking influence of the reverberant field, the approach taken in these experiments is to concentrate on monitoring the higher frequency noise associated with active acoustic emission from the bubbles.

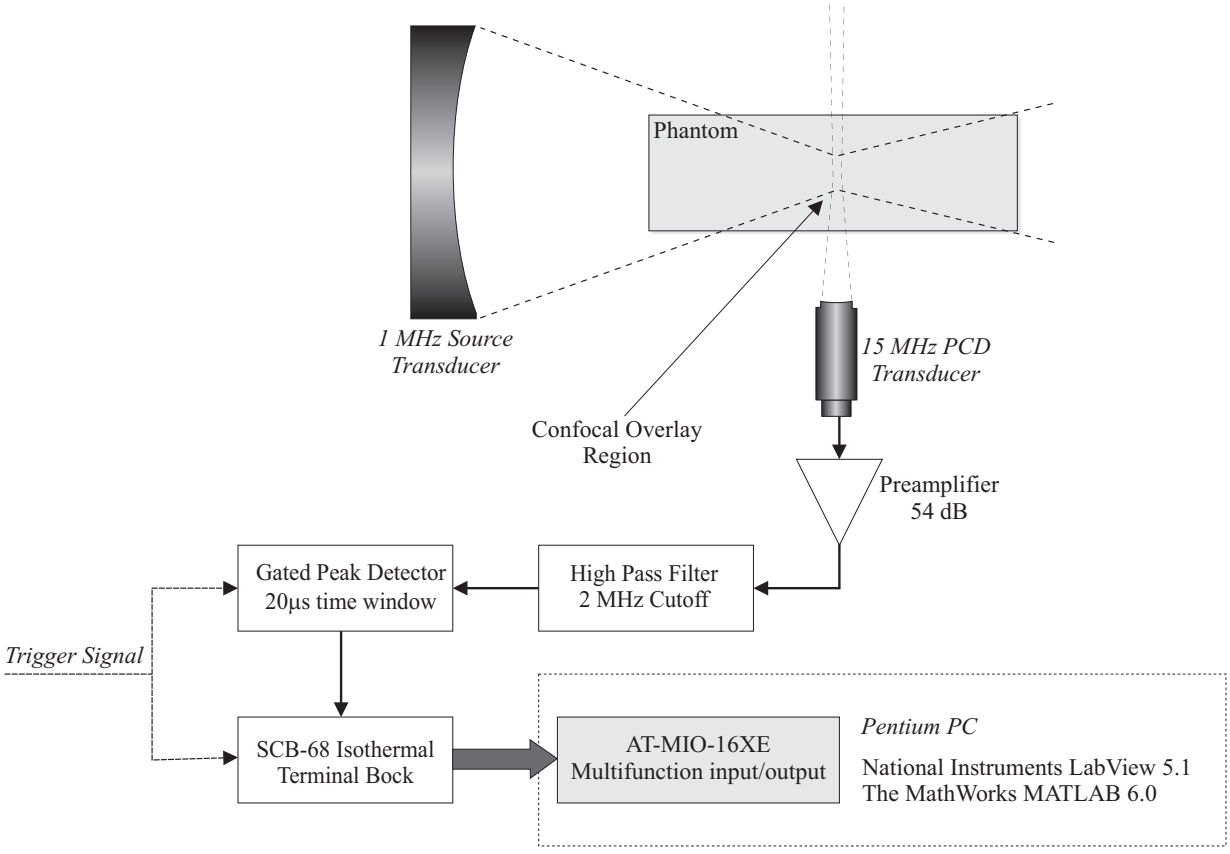

Figure 3.8: Schematic of the passive cavitation detection system. The signal received with a 15 MHz focused transducer, confocally aligned with the source transducer, is amplified and filtered to minimize components at the source frequency. The filtered signal is sampled with a digital gated peak detector for the peak value in a 20 μs time window. This peak value is sampled with a multifunction input/ouput computer board.

A detailed schematic of the PCD system is shown in Fig. 3.8. The received acoustic signal at

the sensing transducer is amplified (Model 5662, 54dB, Panametrics, Waltham, MA) and filtered in high-pass mode with a cutoff frequency of 2 MHz (Model 3940, 24dB/octave attenuation, Krohn-Hite Corp., Avon, MA). The filtered signal is directed to a gated digital peak detector (Model 5607, Panametrics, Waltham, MA). The peak detector determines the maximum PCD voltage for a 20 μs time window between triggers. The trigger source is the same 1 kHz signal from the function generator used by the MIO board. The DC output of the peak detector is connected to the terminal block used by the thermocouples, and finally sampled with the MIO board. The output range of the peak detector is 0 to 1 V, with an 8-bit quantization, yielding voltage output intervals of 3.9 mV. The quantization of the peak detector is substantially larger than that of the MIO board (16-bit, 15.259 μV for a 1 V range) and is the limiting factor in the resolution of these measurements in the absence of noise. The real resolution and noise of these measurements will be described as part of the post-processing discussion in Sec. 3.3

We refer to these time-dependent, sampled voltages from the the peak detector as the "PCD output" of the PCD system. This is our measure of what we have referred to as cavitation activity. We define the magnitude of PCD output to be the "level of cavitation activity", or simply cavitation level, where what constitutes the magnitude must be specified when the term is used. Examples of different measures of the cavitation level would be the mean, max, or rms value of the PCD output.

Some important features of the PCD system deserve further attention. The choice of a 20 μs window of peak detection for every 1 ms of insonation duration is a consequence of limitations in the peak detector, which cannot monitor a larger time window or be triggered at a faster rate. In essence, the detector has a dead time of 98%. However, this is not deemed problematic for CW-insonation at super-threshold pressures, for once the cavitation starts it tends to sustain itself. This effect is aided by the fact that the experiments are run in a gel, where bubbles cannot be forced out of the focus by radiation stress or acoustic streaming. Where this dead time could have an effect is at or near the threshold pressure for cavitation activity. At the inception of cavitation there is a larger likelihood that the activity will be sporadic, and thus may not be consistently detected.

Attention will be paid to the nature and types of acoustic cavitation in Chapter 4. However some

comments regarding the general nature of bubble behavior and the PCD system are necessary here. The PCD system has the property of being particularly sensitive to specific forms of cavitation. Lower energy "stable" cavitation bubbles tend to scatter and radiate at the primary frequency of the incident sound field. As was mentioned, this primary frequency of 1 MHz is intentionally filtered with a high pass filter. This fact, coupled with the frequency response of the PCD transducer, which has a center frequency of 15 MHz, results in a system that is much more responsive to the higher harmonics of the source frequency than to the source frequency itself. Bubbles which are acoustically active in this higher frequency range stand a greater chance of detection. Such bubbles include stable cavities that are pulsating nonlinearly, and inertial cavities that are collapsing violently, resulting in broadband acoustic emission.

3.1.5 *In Situ* Acoustic Pressure Measurement

Measuring the acoustic pressure inside tissue phantoms is important for a number of reasons. It allows us to determine the *in situ* geometric characteristics of the focal region, such as the data shown in Figs. 3.3 and 3.4. It is also one method of accurately positioning the thermocouple with respect to the acoustic axis and the focal plane of the source transducer. The focus of the source is readily determined by moving the phantom until the maximum acoustic pressure amplitude is measured with the hydrophone. If the location of the thermocouple relative to the hydrophone in the phantom mold is determined prior to adding the phantom mixture, the position of the thermocouple with respect to the focus is then known as well.

However, the reason we are most often interested in placing a hydrophone in a phantom is that it permits us to verify our propagation model through the measurement of the absolute, *in situ* pressure amplitude. An important decision in this process is the selection of a hydrophone to embed in the phantom. Ideally, the hydrophone would be broadband with a relatively flat frequency response above 1 MHz. This would capture harmonics above the source frequency due to any nonlinear effects that may develop during propagation of the incident field. Figure 3.9 shows a "membrane" hydrophone (Model 804, 0.6 mm active element [calibration traceable to the National Physical Lab-

oratory] UK, Perceptron, Hatboro, PA) which meets this requirement (seen in the left of the figure). However, practical considerations prevent us from using such a hydrophone. Despite a very small active element (0.6 mm), the cross-sectional area of the entire hydrophone is 11 cm. This fact, coupled with a very fragile membrane and the expense of the membrane hydrophone, make it a poor choice to place through the rigors of casting in a mold with an $80°C$ liquid.

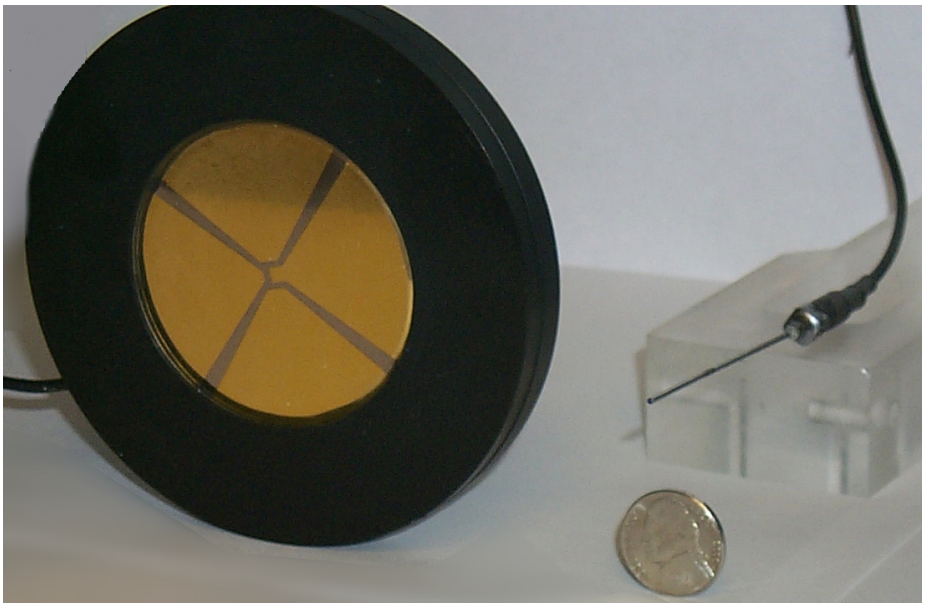

Figure 3.9: Membrane hydrophone (left) and needle hydrophone (right) available for the experiments discussed in this section. The membrane and needle hydrophones have active elements of 0.6 and 1.0 mm respectively.

The alternative available to us is to use a "needle" hydrophone. Figure 3.9 also shows a needle hydrophone (NP-4, 1.0 mm active element, Dapco, Branford, CT) on the right. The needle hydrophone has a slightly larger active element, but a substantially smaller cross-section. Unlike the membrane hydrophone, it will not affect the size of the phantom (already constrained by factors outlined in Sec. 3.1.2), is durable enough to sustain the temperatures and potential knocks and bumps of being cast with the phantom, and is comparatively inexpensive to replace.

The concern with the needle hydrophone is that the frequency response does not approach the behavior of the membrane hydrophone for frequencies of 1 MHz and higher. Figure 3.10 shows the sensitivity of a nearly identical needle hydrophone to the one used in these experiments as a function of frequency. The response of the PVDF hydrophone is shown as well. Although additional

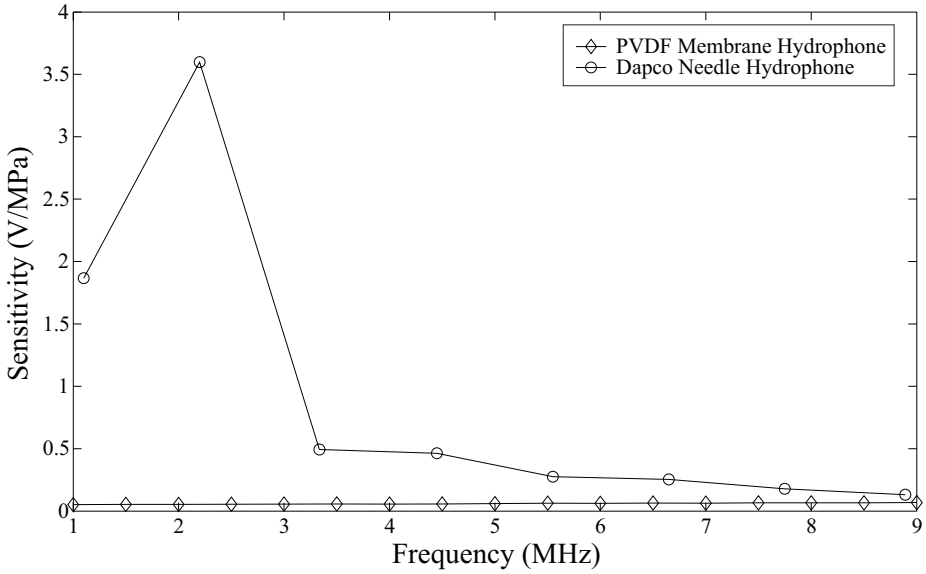

Figure 3.10: Sensitivity values as a function of frequency for the PVDF membrane hydrophone (diamonds) and a needle hydrophone (circles)

measurement points are required in the frequency response to determine the exact location of the peak sensitivity, it is clear that the response of the needle hydrophone is not "flat" as a function of frequency, and that the peak is somewhere between 1 and 3 MHz. The change in sensitivity at frequencies above the insonation frequency complicates the accurate measurement of pressure in the phantom if the propagation becomes nonlinear.

To overcome the deficiencies of each hydrophone, we will take advantage of an accurate, finite difference time domain (FDTD) solution for the acoustic pressure in the phantom. In Chapter 2 the concept of a FDTD solution for the Pennes bioheat transfer equation was presented. As a part of that solution, the Westervelt equation (Eq. 2.21) is solved for the pressure field in the phantom, which in turn allows us to calculate the contribution of primary absorption to the temperature change. This solution for the pressure field in the phantom will be used to determine the pressure in the phantom above the range of accuracy of the needle hydrophone.

The remaining issue is how to relate these numerical results for the pressure at the focus (focal pressure) to a conveniently measurable, experimental quantity. The FDTD results are referenced to the pressure at the surface of the source transducer (source pressure). The actual source pressure can not be measured as readily, for such a measurement requires a very small sensor that can be

placed very close to the face of the transducer. The most convenient measurable quantity is the voltage to the source transducer.

However, a relationship between the voltage to the transducer and the source pressure can be determined by comparing the needle hydrophone measurements in the phantom (as a function of transducer voltage) with the FDTD results (as a function of the source pressure) using results and measurements at the focus as the point of reference. This relationship will be valid so long as it is determined using pressure amplitudes where nonlinearity is not present, and the needle hydrophone measurements are known to be accurate. The details of the procedure are described in Chapter 5.

3.2 Temperature Measurements

An example of a "typical", *in situ* temperature measurement is shown in Fig. 3.11. Temperature is plotted as a function of time for an insonation duration of 1 second, a source frequency of 1 MHz, and with a peak negative acoustic pressure of 1.75 MPa. The measurement was made in the focal plane with the thermocouple located 0.5 mm off-axis. The plot is of the raw data without any averaging, filtering, or other post-processing, either in hardware or software. Threshold pressures for the enhanced heating effect will be discussed in detail later in this chapter, but it should be pointed out that in this example, there is no indication of enhanced heating, either in the temperature response or the associated PCD measurements (shown in Fig. 3.14). The temperature response where enhanced heating is observable has a similar form, though those results vary substantially in the overall magnitude of the peak temperature. Examples of responses above the threshold pressure for enhanced heating will be shown in subsequent sections.

The high frequency noise seen in Fig. 3.11 is not characteristic of *in situ* temperature responses. It is the direct result of electrical noise in the temperature measurement system. We can estimate the magnitude of this noise by measuring what should be a constant temperature value, *e.g.*, a measurement with the thermocouple placed in a constant temperature bath. The result of such a temperature measurement, made in a reservoir of water at room temperature, is shown in Fig. 3.12.

Analysis of the data shows a standard deviation of 0.1058 $^{\circ}C$ and a standard error of 0.0017 $^{\circ}C$.

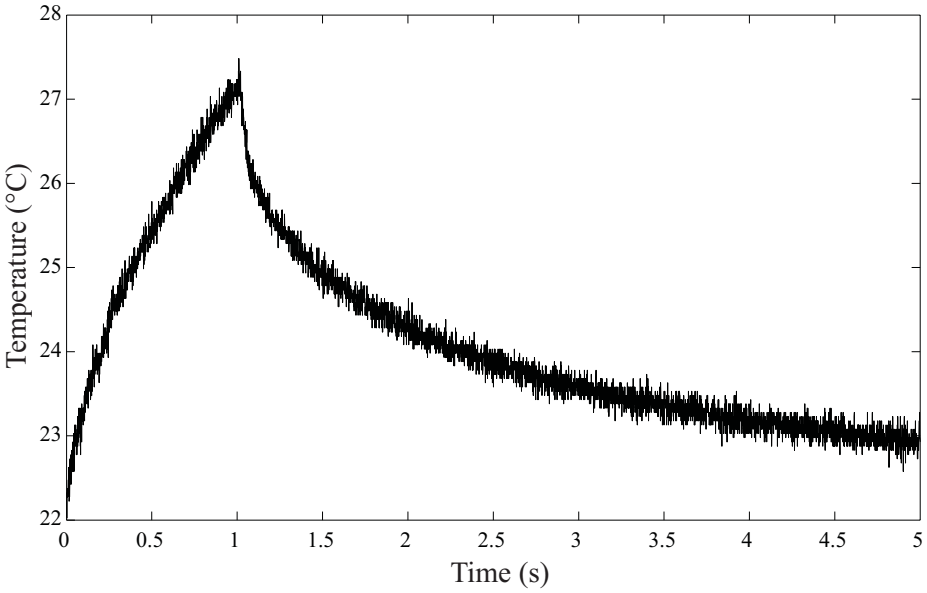

Figure 3.11: Example of temperature as a function of time *in situ* for a 1 second insonation duration, a source frequency of 1 MHz, and with a peak negative acoustic pressure of 1.75 MPa The data is shown without any averaging, filtering or other post-processing.

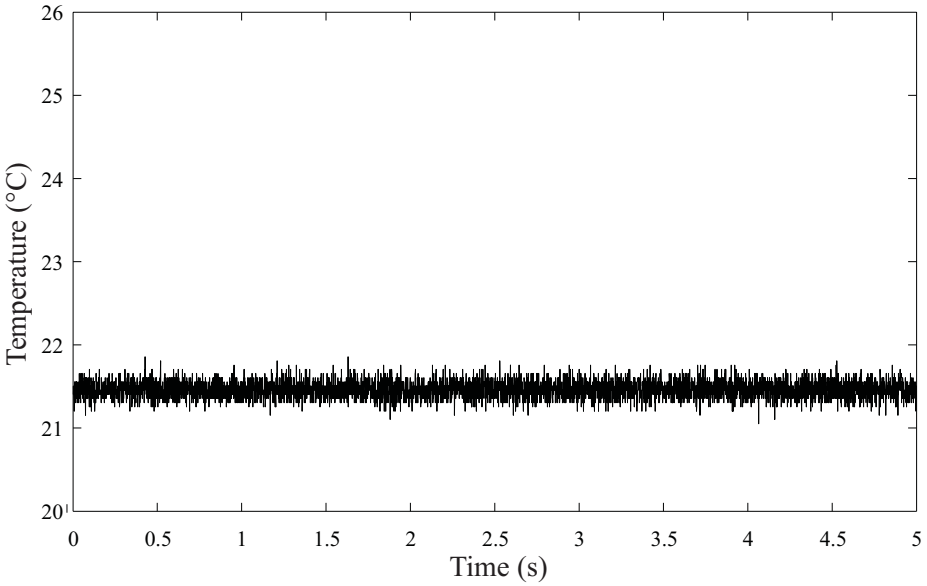

Figure 3.12: Temperature as a function of time in a constant temperature water bath with no acoustic source. The data is shown without any averaging, filtering or other post-processing.

Two objectives must be considered when evaluating the importance of the magnitude of the uncertainty introduced by this electrical noise on temperature measurements: (1) determining absolute temperature values for comparison to tissue heating models and (2) detecting both qualitatively and quantitatively an enhanced heating effect. It will be shown in subsequent sections that enhanced heating results in an increase in the peak temperature response of as much as 20 to 40°C over predictions by models in the absence of enhanced heating. For changes of this magnitude, the noise level discussed here will influence the measured values a fraction of a percent, and not alter any qualitative understanding of the effect.

In the absence of enhanced heating, or for relatively low enhanced heating levels, the temperature change is typically less than 10°C, and often as little as 1 to 5°C. In this range, the noise in the system will have a greater impact than for high levels of enhanced heating in determining the absolute temperature values. An additional motivation for reducing the level of noise, either prior to or after acquisition, is for qualitative analysis of the data. As the pressure amplitude is slowly increased in a study of the temperature response as a function of pressure, both the absolute temperature change from ambient, and the relative temperature change between pressure amplitudes will be small for low pressure amplitudes. Reducing the level of noise in the measured temperature will aid in a visual, qualitative analysis of the data (to be shown in Fig. 3.13).

A substantial portion of this high frequency noise can be removed, with little or no effect on the relatively slowly changing temperature response, by applying a simple moving-average filter of the form [59]

$$T_f[n] = \frac{1}{N+M+1} \sum_{k=-N}^{M} T[n-k] \tag{3.1}$$

where $T[n]$ and $T_f[n]$ represent the acquired and filtered temperatures, respectively, at sample n, and N and M indicate the number of samples averaged per filtered point. Figure 3.13 shows (a) measured and (b) filtered, using a 7 point moving-average filter, temperature values for the same parameters described for Fig. 3.11, but at peak negative acoustic pressure amplitudes of 0.7 and 0.9 MPa. The difference in the peak temperature between these two measurements is of the same order of magnitude as the noise in each signal. As a result, it is difficult to differentiate each response

without some form of filtering. Unless otherwise specified, the remainder of the temperature data presented in this chapter will include this moving-average filter to facilitate a qualitative assessment of the behavior.

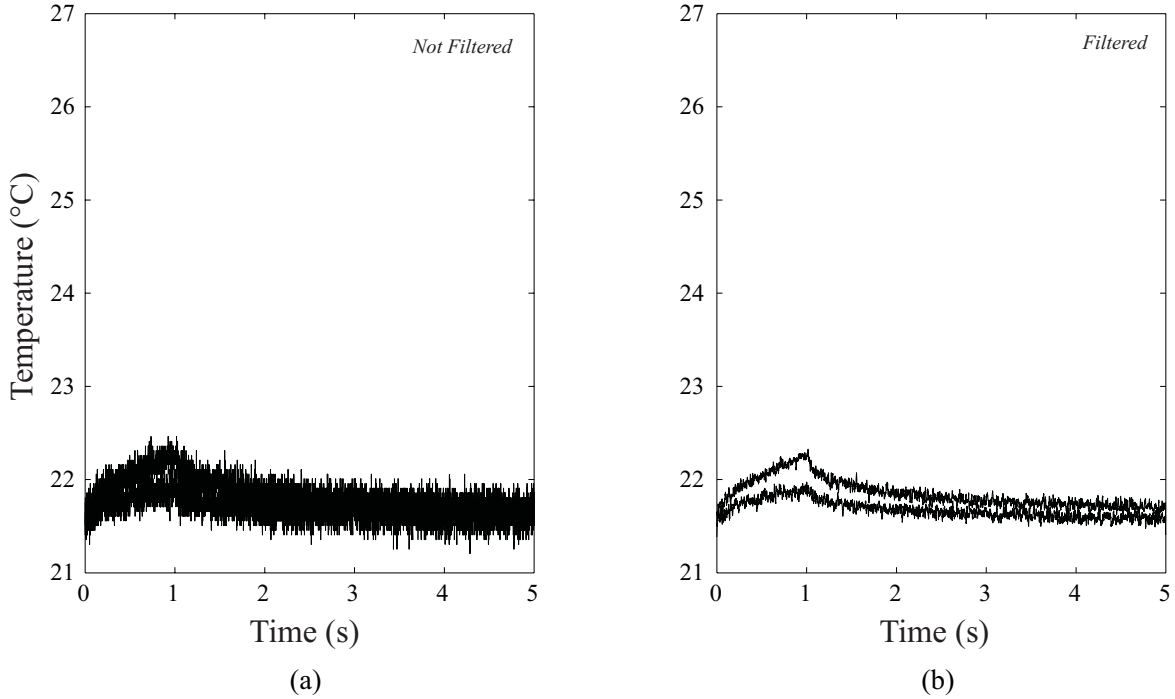

Figure 3.13: Temperature as a function of time *in situ* for peak negative pressure amplitudes of 0.7 and 0.9 MPa at the focus: (a) not filtered and (b) filtered with a 7 point moving average filter.

3.3 Passive Cavitation Detection Measurements

Example PCD measurements can be evaluated in much the same way as the temperature response, to become familiar with the nature of the system, and to determine the relative importance of noise. However, due to the dramatic difference in the output of the PCD system based on the presence or lack of cavitation activity, these two circumstances must be considered individually.

3.3.1 PCD Signal Characteristics: No Cavitation

An example of the output from the PCD system as a function of time is shown in Fig. 3.14, for the same parameters as the temperature measurement in Fig. 3.11. As with the temperature response,

there has been no post-processing of the data. Additionally, there are no indications of cavitation activity.

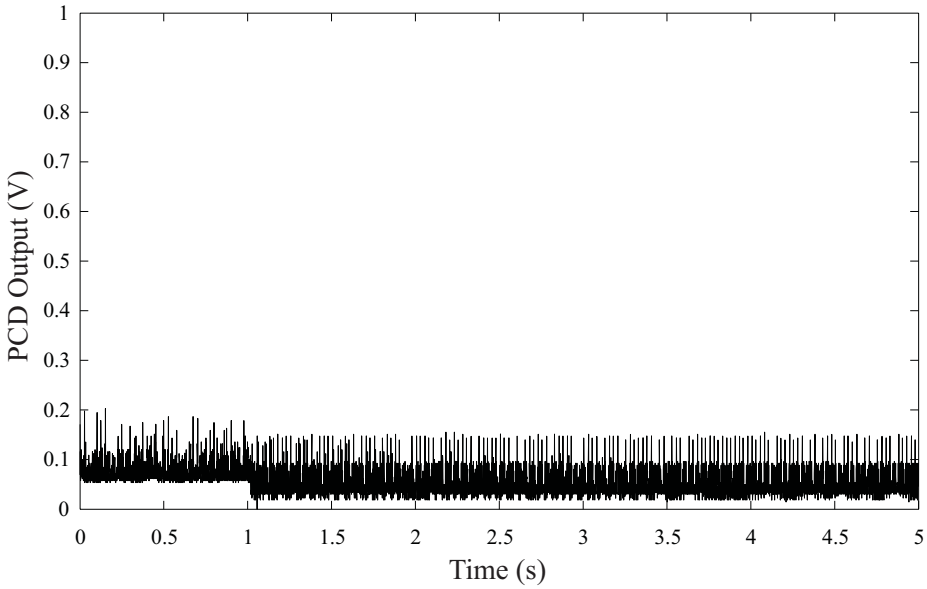

Figure 3.14: Sample PCD measurement in the absence of cavitation for a 1 second at a source frequency of 1 MHz. The data is shown without any averaging, filtering or other post-processing. The slight increase in the PCD output during insonation represents the background acoustical noise of the system.

The PCD output in Fig. 3.14 represents two distinctly different measurements when considering insonation and post insonation intervals. When the acoustic source is inactive, the output represents only the inherent electrical noise in the system and is not a function of the acoustic pressure. Analysis of the post insonation data in Fig. 3.14 yields a standard deviation of 0.0295 V and a standard error of 0.0005 V for the fluctuations in the noise level. During insonation, the output includes not only the electrical noise, but additionally any coherent reverberation or scattering due to the acoustic source, though still unrelated to cavitation activity (the high pass filter fails to remove *all* the signal energy at the insonation frequency). This second component *will* be a linear function of the acoustic source pressure. The magnitude of this acoustical noise can be determined by subtracting the electrical noise, determined from the post-insonation data.

Ideally, it would be desirable to use measurements in the absence of cavitation activity to determine the background acoustical noise for all pressure amplitudes investigated. Given these measures of acoustical and electrical noise, it would be possible to determine the output solely at-

tributable to cavitation activity if and when it occurs. It will be shown that there are some pressure amplitudes for which cavitation cannot be avoided for the insonation times employed. It is possible to minimize the likelihood of cavitation activity by employing very short pulses, however, that will alter the reverberant field as well. As a result, acoustical noise in the absence of cavitation activity at the latter pressures cannot be isolated, and the magnitude acoustical noise cannot be determined independent of any cavitation activity.

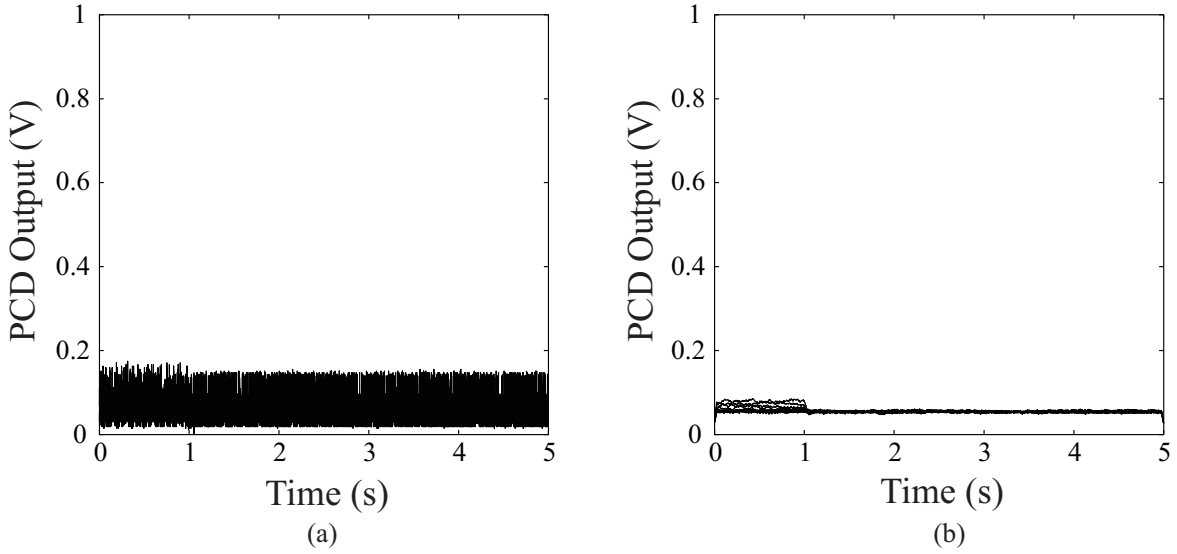

Figure 3.15: Sample PCD measurement in the absence of cavitation for a 1 second at a source frequency of 1 MHz for 9 peak negative acoustic pressure amplitudes between 0.0 and 1.75 MPa (a) the data without any averaging, filtering or other post-processing (b) the data with a 50 point moving-average filter applied.

Determining the pressure dependence of the acoustical noise is only of consequence if the magnitude with increasing pressure amplitude is significant with respect to either the electrical noise, or the cavitation activity. Figure 3.15a shows the PCD response for 9 acoustic pressure amplitudes between 0.0 and 1.75 MPa. It is clear from this figure that any dependence of the acoustical noise on the source pressure amplitude is lost in the electrical noise of the system. However, the level of noise in Fig. 3.14 can be reduced in a manner similar to that applied to the temperature response, by using a moving-average filter.

Unlike the temperature response, which is expected to vary during and for some time after insonation, the output from the PCD should remain constant during these times (still limiting the

discussion to responses without cavitation activity). After insonation, the PCD output would ideally be a DC value of zero, representing a lack of any acoustical or electrical noise in the system. During insonation, any acoustical noise due to reverberation or scattering due to the CW-output of the acoustic source at 1 MHz would be expected to reach steady-state with respect to the 1 kHz sampling rate of the PCD system, and maintain a constant value as well (in the absence of additional, time-varying events such as cavitation activity). As a result, it is possible to remove more noise from the PCD measurements than the temperature measurements which are time dependent, and obtain a "cleaner" signal.

Figure 3.15b shows the same data for multiple PCD measurements as a function of acoustic pressure amplitude, as was shown in Fig. 3.15, filtered with a 50 point moving-average filter. Reducing the level of electrical noise in this way makes it possible to see the dependence of the acoustical noise on the source pressure amplitude. However, the peak, combined acoustical and electrical noise (for the greatest pressure amplitudes encountered) remains less than 10% of the full range of the PCD system. As an additional note, though the acoustical noise may increase with increasing insonation pressure, the level of cavitation activity, when present, will increase as well. In the following section, this combined magnitude of the acoustical and electrical noise will be compared to the output in the presence of cavitation activity, and shown to be of relatively little importance under most circumstances.

3.3.2 PCD Signal Characteristics: Cavitation Present

Figure 3.16 shows a "typical" output from the PCD system when cavitation activity is detected. Although the exact behavior in the presence of cavitation activity can vary greatly, the example in Fig, 3.16 is representative of most incidents with cavitation activity: at some point during insonation the output increases dramatically (the onset or "nucleation" of observable cavitation activity) and remains at an elevated level, until the end of insonation (sustained cavitation activity). In many cases, the increase in the output begins nearly instantaneously, covering the entire insonation duration, and may saturate the detector, as seen in Fig, 3.16. In no measurements observed during the course

of this research did the cavitation activity cease during the insonation time once initially observed.

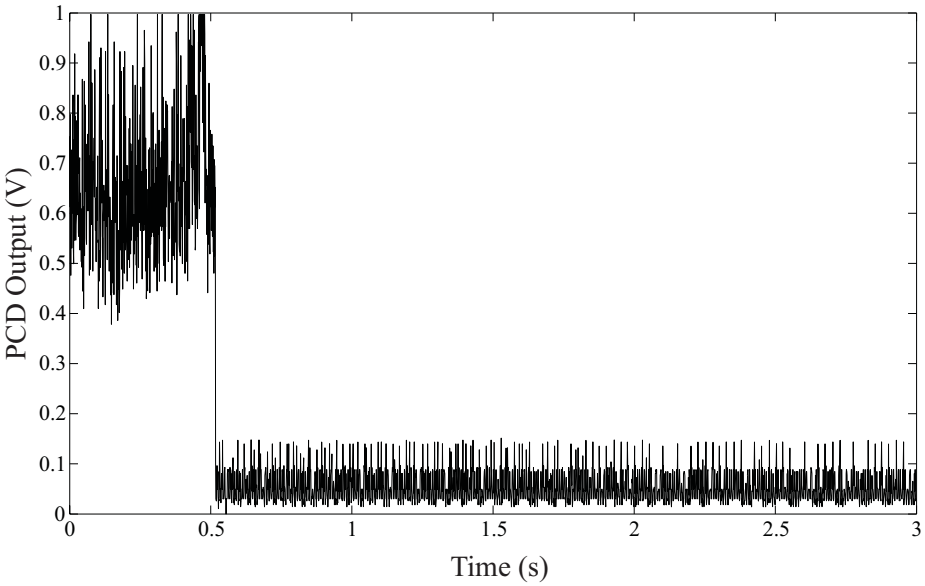

Figure 3.16: Example of the output of the PCD system when cavitation activity is detected. The data shown is not filtered or otherwise post-processed.

Ignoring for the moment the dramatic change in amplitude, the most important feature of Fig. 3.16 to consider in this section is the level and frequency of the PCD output that are a consequence of cavitation activity during insonation. These fluctuations vary as rapidly as the electrical noise in Fig. 3.11, however, the magnitude is far greater, and cannot be attributed solely to noise. As a result, any filtering of the PCD data where cavitation is observed will likely change the contributions of both cavitation activity and electrical noise to the overall signal. However, this may or may not be important depending on how the PCD signal is processed. For example, if the mechanism used to ultimately evaluate the PCD output is the maximum output during insonation, the effect of a moving average filter will vary based on the nature of the PCD response. Conversely, if a mean value of the response is desired, applying a moving average filter first will not alter the results substantially. As an example, the maximum value for Fig. 3.16, 0.99, reduces to 0.81 after filtering with the moving-average filter, or a change of approximately 20%. Taking the average value of the signal after applying the moving-filter, as compared to simply taking the average of the raw data results in a mean of 0.652 as opposed to 0.655, or a change of less than one half of a percent.

3.4 Observation of Enhanced Heating

The first important experimental observation of this research is what has been referred to thus far as the enhanced heating effect. Although the detection and measurement of this effect in and of itself is not unique, the ability to make this measurement provides the framework for all other experimental research presented here. Figure 3.17 shows the temperature response as a function of time and peak negative acoustic pressure amplitude for 13 approximately equal pressure steps from 0.0 to 2.2 MPa. The results are from a phantom made with recipe "Agar-01". The insonation duration is 1 second at a source frequency of 1 MHz. The single thermocouple is located in the focal plane, 0.5 mm off-axis. The temperature response is plotted for a 5 second interval, however, the phantom was allowed to rest for a minimum of 100 seconds between each insonation. This duration was sufficient to allow the heated phantom to return to the ambient temperature.

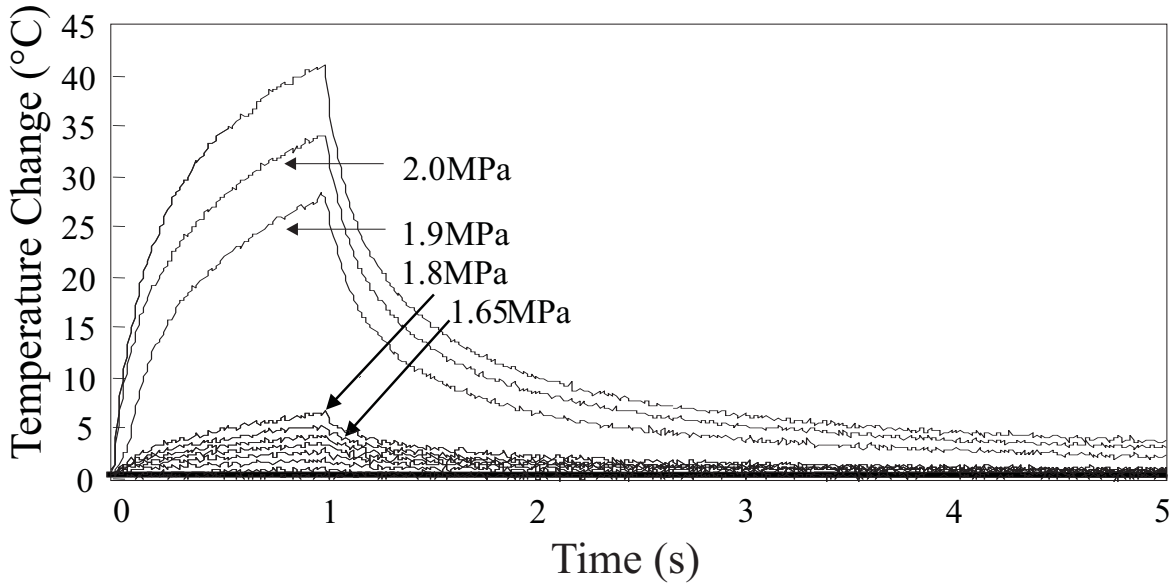

Figure 3.17: Temperature as a function of time for increasing acoustic pressure from 0.0 to 2.2 MPa. An enhanced heating effect is seen above 1.8 MPa where the peak temperature increases five-fold.

The most important feature of Fig. 3.17 is the dramatic increase in the rate of heating and the resulting peak temperature, between the measurements at 1.8 MPa and 1.9 MPa. All of the models described in Chapter 2 predict, either explicitly or approximately, a peak temperature that is proportional to the acoustic pressure squared. The changes in Fig. 3.17 are consistent with these

predictions up to and including 1.8 MPa. However, above this apparent threshold pressure for enhanced heating, the peak temperature output is substantially larger than expected (approximately 4-5 times greater than the expected value). It has been mentioned that this distinct threshold pressure in the temperature response is similar to a threshold effect commonly associated with the onset of acoustic cavitation. However, this fact alone is not sufficient to demonstrate a cause and effect relationship between the sudden onset of an enhanced heating effect and cavitation activity. Such a correlation is best achieved by direct observation of cavitation activity.

3.5 Correlation of Enhanced Heating and Observable Cavitation Activity

Figure 3.1 shows the configuration of the passive cavitation detector (PCD) for which the operational details have been described in Sec. 3.1.4. The important concept related to this detection scheme as it relates to the correlation of temperature and cavitation effects is that the temperature and PCD responses are measured simultaneously, and over the same time frame. Figure 3.18 is a plot of both the temperature response and the PCD measure of cavitation activity as a function of time for three pressure steps at or near the threshold for enhanced heating. The experimental parameters are identical to those described in Sec. 3.4.

Figure 3.18c, for a peak negative acoustic pressure amplitude of 1.65 MPa, shows a typical temperature response, and the baseline PCD response when there is no enhanced heating and no indications of cavitation activity. The PCD output at this pressure represents the background acoustical and electrical noise as described in Sec. 3.3. The temperature response is due exclusively to primary absorption (as can be seen in Fig. 2.6 where the BHTE with primary absorption predicts temperature values consistent with experimental values for pressure amplitudes below the threshold for enhanced heating). The outputs for both the temperature and PCD start out much the same in Fig. 3.18b, at 1.8 MPa. However, at approximately half the insonation time, there is a dramatic increase in the rate of heating. This change is accompanied by a substantial increase in the PCD out-

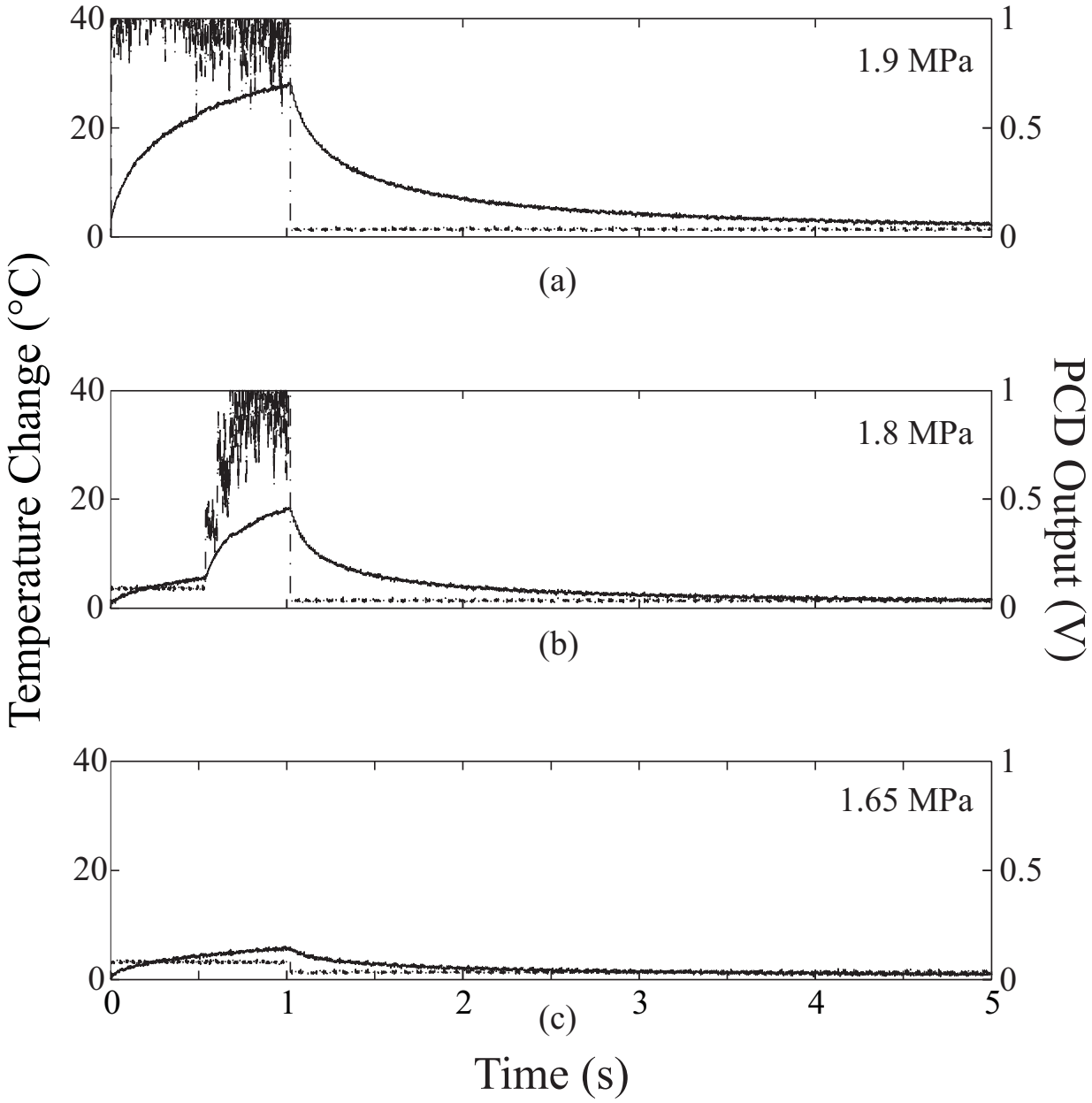

Figure 3.18: Temperature (*in situ*) (solid line) and cavitation activity (dotted line) as a function of time for three measurements at or near the threshold pressure for enhanced heating.

put, indicative of the onset of cavitation activity. This represents the onset of the enhanced heating effect and observable cavitation activity, and 1.8 MPa is the apparent threshold for this effect in this phantom, given a 1 second insonation duration. In Fig. 3.18a, the pressure amplitude at the focus has been increased to 1.9 MPa, the threshold pressure has been exceeded, and the enhanced heating effect occurs nearly instantaneously, as does the increased PCD response.

The nearly synchronous behavior in time between the two effects, seen in Fig. 3.18, is representative of the majority of the measurements made where the onset of enhanced heating and cavitation activity occurs some time after the start of insonation. However, a result that will be important for consideration in later sections is that there are circumstances under which the relationship is not as clear as that seen in Fig. 3.18. The results of Fig. 3.18 are representative of measurements where the first indications of cavitation activity and enhanced heating are large in magnitude with respect to the acoustical noise and the heating due to primary absorption respectively.

Under some circumstances, however, the initial cavitation response is distinguishable from the acoustical and electrical noise in the PCD system, yet is not as dramatic as the results shown in Fig. 3.18. In many of these cases, a resulting enhanced heating effect either does not occur, or is not substantial enough to be detected, either qualitatively through a visual assessment of the data, or through quantitative measurements, such as in comparison with model predications. An example of this scenario is shown in Fig. 3.19. The upper and lower plots show temperature and PCD output as a function of time, respectively, for 11 pressure steps between 0.0 and 1.6 MPa. The bold lines in the upper and lower plots represent the temperature and PCD output at an acoustic pressure amplitude of 1.6 MPa. The onset of some form of cavitation in the upper plot is readily apparent, however, the onset of this event is not reflected in temperature response in the same manner as in Fig. 3.18. This could be the result of a number of factors, such as the lack of a sufficient number of bubbles, or the presence of bubbles which are sufficiently acoustically active to influence the PCD response, but not quite of optimal size to induce measurable heating.

The correlation between cavitation activity and enhanced heating is not exclusive to the onset of each effect. Figure 3.20 shows the normalized peak temperature change and mean PCD output

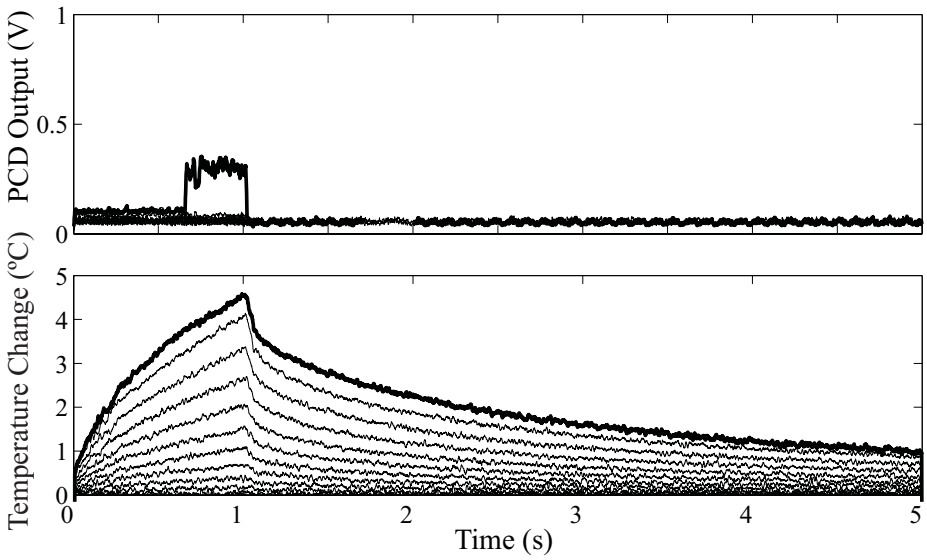

Figure 3.19: Temperature and PCD output as a function of time for 11 pressure steps between 0.0 and 1.6 MPa. The bold line indicates each response at 1.6 MPa.

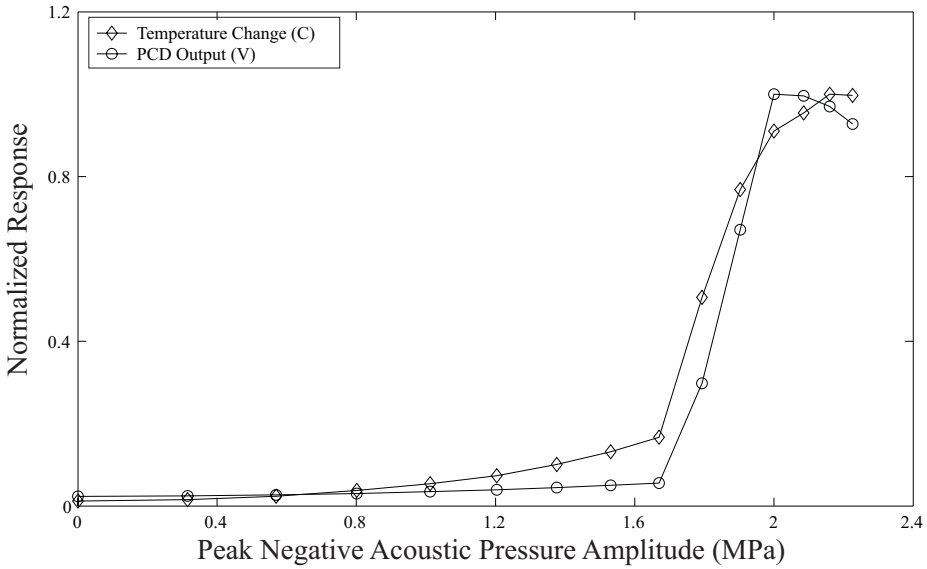

Figure 3.20: Normalized peak temperature response (diamonds) and observable cavitation activity (circles) as a function of peak negative acoustic pressure. The data has been normalized with respect to the peak value of each response to compare the relative change in magnitude as a function of acoustic pressure.

as a function of peak negative acoustic pressure for the same experimental parameters. The data represents a single measurement of the peak temperature and mean PCD value at each pressure. A degree of correlation exists between the relative change in each effect over the entire pressure range, not simply in the onset of each effect. In addition there is a saturation in the magnitude of both measurements, in this case occurring above approximately 2 MPa, where the rapid increase in both temperature change and cavitation activity either slows, or even declines.

The correlation coefficient, ρ_{tp}, between the the peak temperature change and the mean PCD output in Fig. 3.20 is 0.986, where the correlation coefficient is defined as

$$\rho_{tp} = \frac{C_{tp}}{\sigma_t \sigma_p}, \tag{3.2}$$

C_{tp} is the covariance between the peak temperature and the mean PCD output, σ_t is the standard deviation if the peak temperatures, and σ_p is the standard deviation of the PCD values [60].

This high correlation is not limited to a single set of measurements of temperature and cavitation activity, or to a single insonation duration. The values in Table 3.3 are the result of an analysis of the correlation coefficients for multiple measurements of temperature and cavitation activity over a range of insonation times. The experimental configuration is the same as that specified for in Fig. 3.20. The phantom recipe is "Agar-02", the peak negative acoustic pressure amplitude at the focus was 0.0 to 2.2 MPa, and the insonation duration ranges from 0.1 to 5 seconds. Specifically, 8 measurements at each pressure amplitude were made at 1 second, and 10 measurements at each pressure were made and 0.1, 0.5, 2, and 5 seconds. The mean correlation coefficient for these 48 measurements is 0.95.

Mean	0.95
Min	0.88
Max	0.99
Standard Deviation	0.03

Table 3.3: Statistics for the correlation between PCD output and temperature for 48 measurements at varying pressures and insonation times.

The strong correlation between the temperature response and the observable cavitation activity is an extremely important experimental observation. The ability to correlate the onset of enhanced

heating with cavitation activity not only in terms of the threshold pressure, where both effects are seen, but also in terms of the actual time of onset for both effects, as shown in Fig. 3.18 is significant. Not only does it indicate that the two processes are related, it also suggests that the specific type or types of acoustically active bubbles that are optimally detected by the PCD are likely those which are largely responsible for the enhanced heating effect. That information allows us to narrow our consideration of the type of cavitation (inertial or noninertial) and the range of bubble sizes involved. As was discussed in Sec. 3.1.4, this PCD system is optimally sensitive to large, stable bubbles which are oscillating nonlinearly, or inertial bubbles which are collapsing violently.

The possibility that the PCD system is particularly sensitive to the type of bubble activity that is responsible for enhanced heating is also supported by the correlation between the overall behavior of the temperature and PCD responses, as seen in Fig. 3.20, and quantified by ρ_{tp}. The data indicates that the relationship between the enhanced heating effect and the nature of the acoustically-active bubbles detected is not limited to the onset of each effect, but also applies to the level of each effect as well.

This is also true with respect to the plateau or saturation in both the temperature response and the PCD output in Fig. 3.20. A similar saturation is seen in the results from Holt and Roy [1] who observed not only a saturation, but a decline in the temperature response if the pressure was increased further. This saturation and decline is also consistent with the results of other researchers obtained *in vivo* [27]. Without direct observation of the bubble field, it is difficult to determine the specific reason for the decline in the PCD response. One possibility is that the density of bubbles in the focal region reaches a point where a portion of the incident sound is shielded from this region. As a result increasing the pressure does not increase the primary absorption, or the amount of bubble activity and subsequent bubble-related heating in the focal region. The idea of bubble shielding has been introduced by others such as Watkin *et al.* who argued that it was responsible for a shift in the region of peak temperature change toward the transducer [61].

The sum of the information in Fig. 3.20 demonstrates a key observation. It is clear from the data that there is a distinct pressure region of optimal heating, in this example, between ~1.8 and

2.0 MPa. Below this pressure range, there is no enhanced heating effect, and the temperature rise due to primary absorption is not significant with respect to the enhanced heating temperatures. Above this pressure range, there is no additional benefit with respect to the temperature rise, and in fact, there may be a decline in the peak temperature achieved. One possible application of this result is that the optimal range is determined prior to insonation. However, the strong correlation of the PCD output and the enhanced temperature effect means that this information may not be necessary prior to insonation. This optimal range can potentially be obtained in real-time from observation of the level of cavitation activity. This is important for biological tissue whose properties are not consistent between samples, and where prior knowledge of the optimal pressure may not be possible.

3.6 Insonation Duration

A useful parameter to examine in conjunction with the enhanced heating effect is the insonation duration. Unlike parameters which are difficult to vary, such as frequency (which requires either multiple or very broadband source transducers) or phantom material properties (which requires several different measurements), the insonation duration is relatively straightforward to change and investigate. This is important in therapeutic applications which take advantage of an enhanced heating effect (*e.g.*, achieving a desired temperature rise sooner or with a lower acoustic source strength) where changing a parameter must not only prove effective, but practical as well. A study of insonation duration may also lend insight into the physical processes as work. For example, a lower threshold for longer insonation times may suggest that gas diffusion plays a role in the cavitation nucleation process and/or the ensuing bubble dynamics, where an extended insonation time allows bubbles which are not efficient heat sources to grow to a more effective size via a process called rectified diffusion [62].

3.6.1 Determination of Enhanced Heating and Cavitation Threshold Pressures

In this section, possible criteria for defining the threshold pressure for cavitation activity and enhanced heating are explored, within the context of determining the effect of insonation duration. This choice is not an obvious one as there are multiple analysis techniques available for the PCD output and temperature response, all of which may provide a reasonable means of estimating a threshold pressure. There is also some question as to what physical effect the "threshold" pressure should be considered a threshold for. A traditional definition for the "cavitation threshold" can be summarized as the minimum pressure amplitude required to initiate or "nucleate" cavitation activity [55, 63]. Keeping in mind potential therapeutic applications of the enhanced heating effect, it is unclear whether this definition is sufficient or appropriate where repeatability and predictability may be important. In this context, we may want to consider a threshold pressure based at least in part on the repeatability of cavitation activity or the enhanced heating effect over multiple measurements, rather than the minimum pressure for which there is only one occurrence of either effect. This distinction will become more clear as the data is analyzed.

It is important to note that the objective here is not to determine *the* absolute threshold pressure for our measurements, for that is closely linked to the cavitation nuclei present in a given experimental arrangement. The precise threshold *in vitro* will not translate to the same threshold *in vivo*, nor is there likely to be a simple relationship given the complexity of biological tissue and the variability in the number of preexisting nucleation sites in different tissues and organs. What is important is the effect of insonation time on threshold pressure. Therefore, the choice of criteria for determining the threshold pressure is not as critical as ensuring that the criteria is applied uniformly across insonation times.

In the following two sections we consider three criteria for specifying a threshold pressure, each applied to the PCD output and the temperature response. The data analyzed in this section consists of 52 sets of measurements representing 5 different insonation times. Each set of measurements consists of 14 discrete measurements at increasing peak negative acoustic pressure amplitudes at the focus from 0.0 to 2.85 MPa. The insonation times are 0.1, 0.5, 1, 2, and 5 seconds with 10 sets of

measurements at each pressure amplitude, with the exception of 12 for 1 second. The phantom is recipe “Agar-02” and contains one thermocouple, in the focal plane, 0.5 mm off-axis. Of the 52 sets of measurements, 51 had at least one detectable occurrence of enhanced heating over the range of pressure amplitudes tested.

Thresholds Linked to Cavitation Activity

A simple method for estimating the threshold pressure for cavitation activity is to make a qualitative assessment of the presence of cavitation activity using the PCD output as a function of time. This can be accomplished by examining plots similar to the one shown in the upper portion of Fig. 3.19. The advantage of this method is that most occurrences of cavitation activity can be readily identified, without concern for a misinterpretation due to a “baseline” response. Here, we consider the baseline response to mean anything unrelated to cavitation activity, such as acoustical and electrical noise. Figures 3.16, 3.18, and 3.19 have shown that when cavitation activity is detected, the contribution of bubbles to the PCD output can generally be visually distinguished from the baseline response. Investigating each response individually also allows a quantitative determination of the number of measurements at each pressure amplitude which do and do not show indications of cavitation activity. This information would be lost if the aggregate behaviors of all the measurements at a given pressure amplitude and insonation duration are simply lumped together (*e.g.*, through a mean value, or some similar mechanism).

The disadvantages include the fact that a visual assessment makes it difficult to ensure that a uniform standard is applied across insonation times, and even multiple measurements of the same insonation time. It has been stated that incidents of cavitation activity typically result in significant changes in the PCD output. However, if there is any region where small levels of cavitation activity could be indistinguishable from the acoustical noise visually, it would be in the region of interest - near a threshold pressure. An additional disadvantage is that subjective decisions must be made such as whether “latent” cavitation activity (where the onset occurs late in the insonation duration) should be considered equally with “prompt” activity (which occurs at the start of insonation).

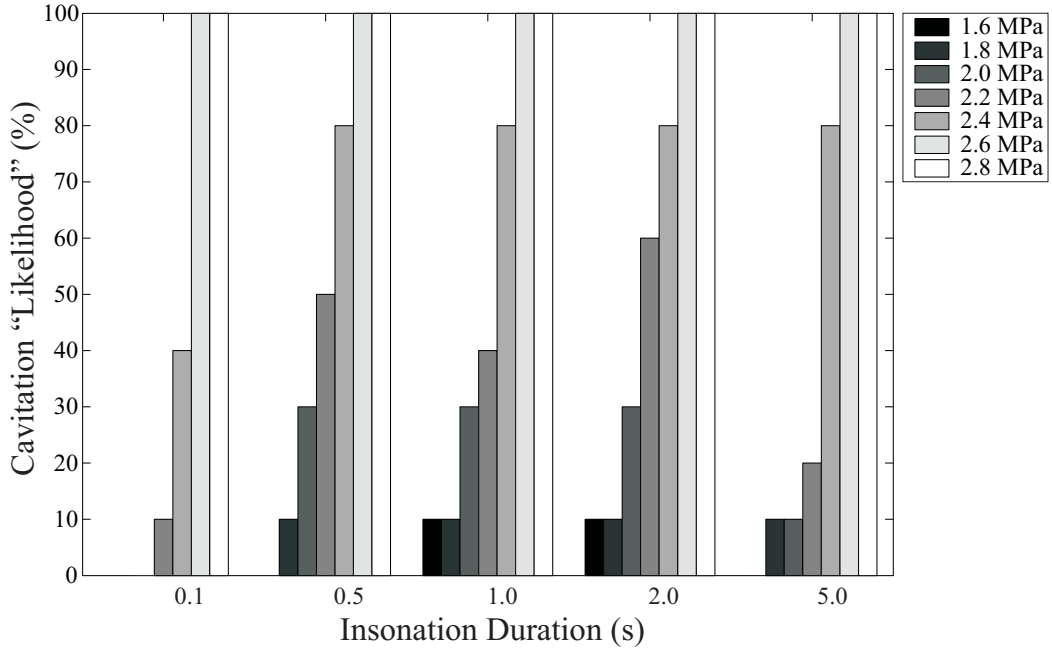

Figure 3.21: Percentage of measurements with cavitation activity detected based on a qualitative analysis of the PCD output as a function of time (10 point samples for 0.1, 0.5, 2, and 5 seconds. 12 point samples for 1 second.

Figure 3.21 shows the percentage of measurements, categorized by insonation duration, where there is any indication of cavitation activity, determined visually, as described above. The values in Fig. 3.21 could be considered the "likelihood" that some form of observable cavitation activity will occur at a particular pressure amplitude and insonation duration. No distinction is made based on the time during insonation when the activity was first detected. The first feature to note in Fig. 3.21 is that there is a noticeable increase in threshold pressure, defined as any occurrence of cavitation activity, for the shortest of insonation times, 0.1 seconds. Although there is a slight deviation from the following statement in the results for 5 seconds at 2.0 and 2.2 MPa, choosing criteria such as a 40% or 80% likelihood of cavitation activity will generally produce results which are independent of insonation time for values greater than 0.5 s.

Figure 3.21 also shows another important aspect of the cavitation activity. There are some pressures for which there is a near certainty of cavitation activity, and it is uniform across insonation times. This is a significant result in that the threshold pressure for repeatable and even predictable cavitation activity is markedly higher than that for any occurrence, and is independent of insonation

duration.

We can gain some confidence in the results of Fig. 3.21 by looking at a second criteria for determining a threshold pressure for cavitation activity. This involves examining the aggregate behavior of the PCD output as a function of the particular pressure and insonation duration, and looking at the variability of the output across multiple measurements. If the individual measurements in the absence of cavitation activity are at all repeatable in magnitude (*i.e.*, the noise remains constant across multiple measurements at the same pressure and insonation time), then looking at values such as the standard deviation, or minimum and maximum values of multiple measurements at the same pressure amplitude and insonation duration in this region should indicate very little variation between measurements.

To the contrary, Fig. 3.21 indicates that there are pressure amplitudes where cavitation activity is a possibility, but is not guaranteed. Therefore, at these pressure amplitudes, there will be large variations in the PCD output based on whether cavitation activity is detected. Even for pressure amplitudes where the likelihood of cavitation activity is 100%, there will be variability in the PCD output for each measurement. This distinction in variability of the PCD output from measurement to measurement would potentially isolate these two regions, and in turn, define a threshold pressure.

Figure 3.22 is a plot of the cavitation level, defined as the mean value of the PCD output during insonation, as a function of the peak negative acoustic pressure at the focus. For each plot, representing a single insonation duration, the value plotted for each pressure is a combined measure of all the measurements at that insonation duration. Values are determined as follows:

(1) For each measurement of PCD output as a function of time, a mean value of this response during insonation is calculated (the cavitation level)

(2) The cavitation levels are then averaged to determine a mean cavitation level as a function of pressure amplitude and insonation duration. More importantly, the error bars represent one standard deviation of the values averaged in step 2, and are an indication of the variability in the measurements.

Figure 3.22 is very consistent with Fig. 3.21 if a distinction can in fact be made between the

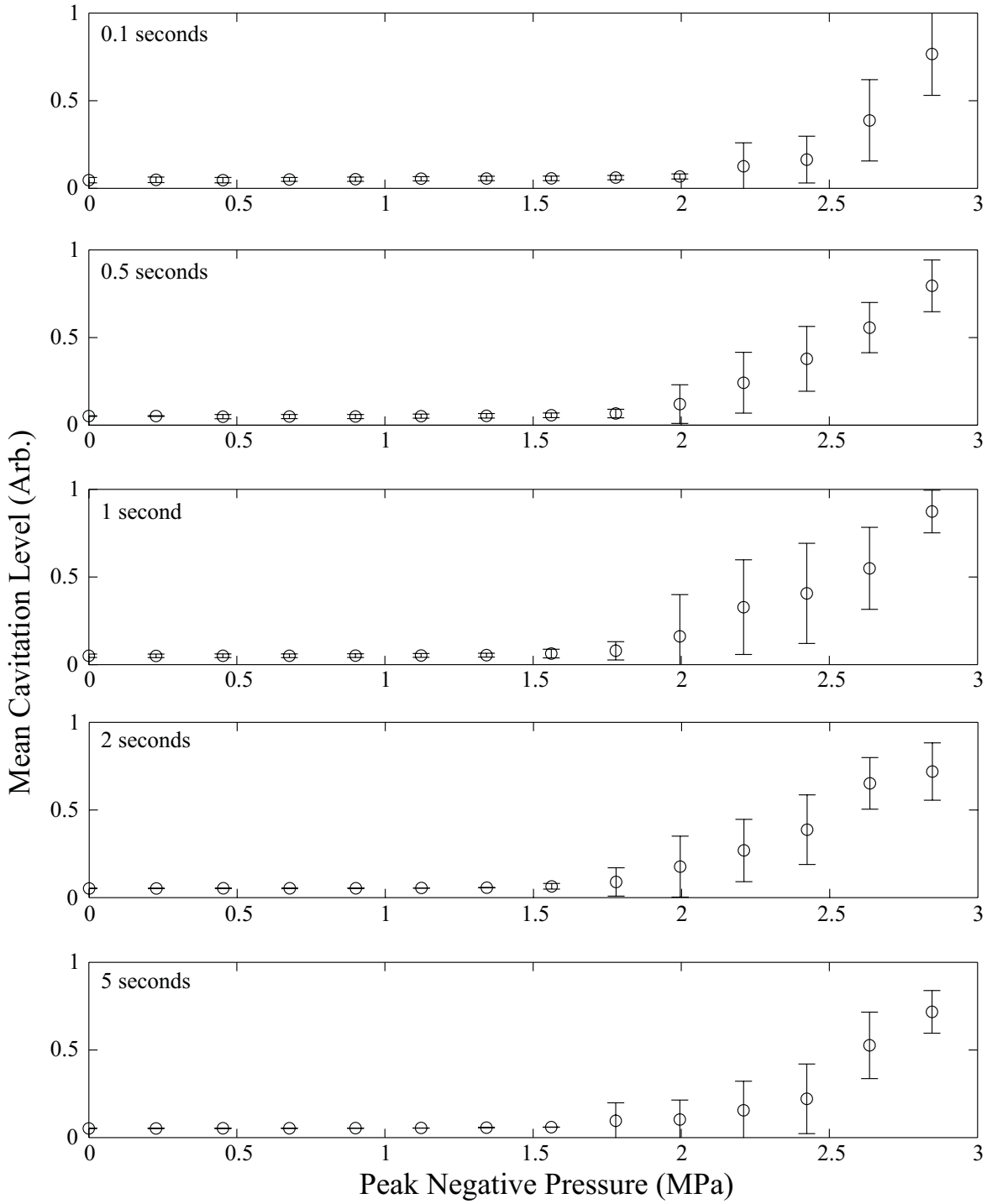

Figure 3.22: Mean PCD output during insonation (cavitation level) averaged over several repeated insonations as function of peak negative acoustic pressure amplitude at the focus and of insonation duration. Results for every measurement are included regardless of the presence or absence of cavitation activity.

occurrence of cavitation activity based on the variability in the PCD output at a given pressure amplitude and insonation time. A change in variability at 1.6 MPa occurs only for insonation times of 1 and 2 seconds, and for 0.5, 1, 2, and 5 seconds at 1.8 and 2.0 MPa, both of which are in agreement with Fig. 3.21. At and above 2.2 MPa there is significant variability for all insonation times, also consistent with the tabulated data.

This is important because it lends credibility to the qualitative determination of observable cavitation activity that created Fig. 3.21. It also suggests that a pressure threshold for cavitation activity, based on the presence of cavitation for at least one measurement, can be determined by looking at the variability in multiple measurements, at least for a moderate number of measurements. For something on the order of tens or hundreds of measurements at just one pressure and insonation duration, it cannot be assumed that one instance of cavitation activity will sufficiently influence a measure such as the standard deviation. As mentioned earlier, however, Fig. 3.22 does not allow for identification of the *percentage* of measurements which represent cavitation activity.

Two methods for determining the threshold pressure for cavitation activity, and potentially enhanced heating, based on the PCD measurements of cavitation activity have been presented. In addition, Fig. 3.21 provides a measure of the likelihood that cavitation will occur. A final criteria to consider is an analysis of the PCD output levels where the only measurements considered are those where cavitation activity is observed. The fact that the likelihood for cavitation activity in Fig. 3.21 is the same at 2.0 MPa for 0.5, 1, and 2 seconds (30%) does not guarantee that the cavitation level, as defined above, will be the same. To understand how this cavitation level is affected by insonation duration, we must look at the subset of measurements where cavitation actually occurs.

The results of such an analysis are shown in Figure 3.23. An identical procedure as was described for the results in Fig. 3.22 was applied to the subset of measurements that were determined to indicate cavitation activity when creating Fig. 3.21. Any measurement where cavitation activity was not detected was ignored. The error bars show the maximum and minimum values. Excluding the measurements with an 80% or 100% likelihood of cavitation activity, there is an insufficient number of measurements in this subset to justify a standard deviation (in some cases, there is only

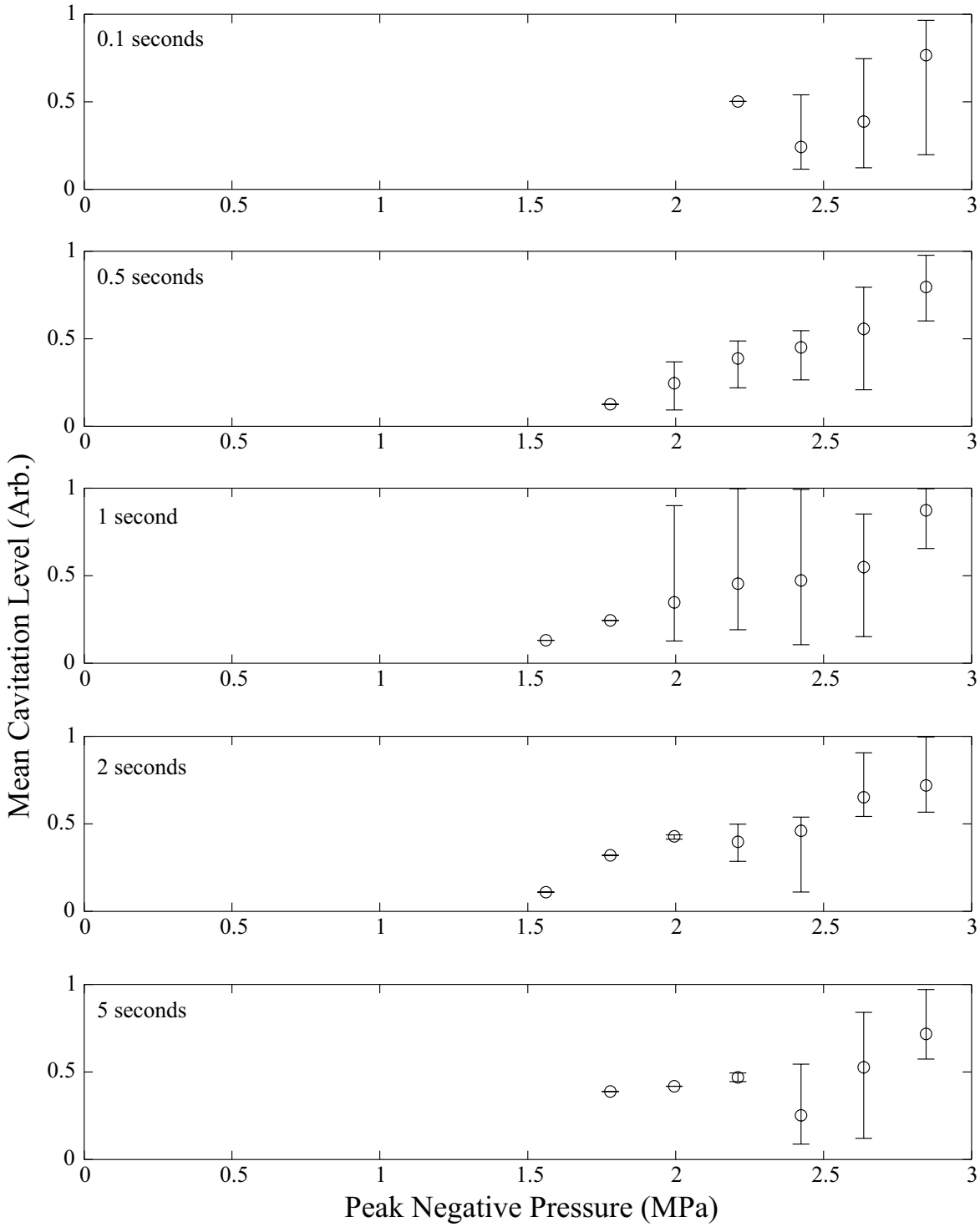

Figure 3.23: Mean PCD output during insonation (cavitation level) averaged over several repeated insonations as function of peak negative acoustic pressure amplitude at the focus and of insonation duration. Results are based only on those measurements where cavitation activity is detected.

one measurement). In addition, using the maximum and minimum gives an indication of the large variability in the cavitation level, even when the pressure amplitude and insonation duration are the same.

Figure 3.23 does not appear to suggest a pronounced trend in the mean cavitation level as a function of insonation duration. However the range of the cavitation level when more than a small sample of measurements (2 - 3) are available can be fairly large making quantitative statements regarding the trends difficult. In general, given a particular likelihood of cavitation activity in Fig. 3.21 the mean cavitation level is consistent across insonation times. Exceptions, such as the results for 2.2 MPa at 0.1 and 5 seconds, represent 1 and 2 measurements, respectively, and are not conclusive.

To summarize the results presented thus far, three criteria for determining the threshold pressure for cavitation activity as a function of insonation duration have been presented. A threshold pressure can be determined by choosing a relative likelihood that cavitation will occur, ranging from one event to nearly 100% confidence. The threshold pressure can also be determined from looking at the variability in multiple measurements of the cavitation level at each pressure. Finally the mean cavitation level when cavitation occurs can be evaluated in determining a threshold pressure.

The results suggest the effect of insonation duration is dependent on the definition of the threshold pressure. There is some variation in the minimum pressure amplitude required to observe at least one instance of cavitation activity, in particular, a noticeable increase in the minimum pressure amplitude for relatively short insonation times, *i.e.*, 0.1 seconds. This is seen in both the individual assessments of the PCD output, and the aggregate behavior of the cavitation level, defined as the mean value of the PCD output level during insonation. A threshold pressure based on a near certainty of cavitation activity, indicated as 100% in Fig. 3.21, suggests a different result. Given that definition, the threshold pressure is not markedly dependent on the insonation time. Lastly, the large variability in the PCD output when cavitation occurs makes it difficult to use this information as a criteria for the threshold pressure.

Thresholds Linked to Temperature Measurements

A similar analysis can be performed for the temperature measurements to determine the threshold pressure for enhanced heating. Although a direct temperature measurement is the most obvious detection mechanism for the enhanced heating effect, it is also an invasive one when using devices such as thermocouples. If the occurrence of the enhanced heating effect can be related to the indicators of cavitation activity, it would provide a non-invasive means of monitoring enhanced heating. Therefore the objectives of this section are two-fold: (1) to determine the influence of insonation duration on the enhanced heating effect and (2) to determine if and how the influence of insonation duration on the enhanced heating effect relates to the effect of insonation duration on cavitation activity.

The most substantial difference in the analysis of the data based on the PCD output and on the temperature measurements has to do with how one goes about quantifying the presence or absence of an enhanced heating effect. Section 3.3 describes why it is difficult to measure a "baseline" response for the PCD output representing the acoustical and electrical noise as a function of the pressure amplitude. However, an accurate model *does* exist that allows us *calculate* the baseline temperature response. This baseline response is the temperature rise due to primary absorption. Any additional temperature elevation is due to additional sources of heat deposition, and is considered an enhanced heating effect.

Despite the quality of the model, there will be small differences between measured results and numerical predictions. At low levels of enhanced heating, where the temperature elevation does not necessarily have the distinctive shape seen in the middle plot of Fig. 3.18, nor the magnitude of the top plot in the same figure, it may be unclear whether a slightly higher measured peak temperature is due to enhanced heating, or is simply due to small uncertainties in the model and measurement. For this analysis, we choose not to categorize a temperature elevation less than the difference between model predictions and experimental results (determined in the absence of enhanced heating) as an enhanced heating effect.

The general procedure for developing a table similar to Fig 3.21 for the enhanced heating effect

is as follows:

(1) Calculate a predicted temperature rise due to primary absorption using a numerical solution the Pennes equation

(2) Determine the magnitude of the maximum difference between the numerical predictions and the experimental measurements in the absence of enhanced heating

(3) Identify temperature measurements whose peak temperature exceeds that of the numerical predictions by an amount greater than the difference determined in step 2

Each of the steps will be explained in greater detail below.

Step 1 involves solving Eq. 2.22 for temperature in the phantom as function of peak negative acoustic pressure amplitude at the focus, and insonation duration. The numerical solution will be detailed in Chapter 5. A new solution is calculated for each parameter that is varied experimentally. These solutions can be analyzed in the same manner as the experimental results, by extracting values such as peak temperature, and comparing them to other simulations or experiments.

In step 2, an upper-bound of the difference between the numerical predictions and the experimental results in the absence of enhanced heating is determined. The numerical predictions and experimental measurements of temperature will never agree exactly for reasons including the uncertainty due to electrical noise described in Sec. 3.2 and numerical errors due to discretization, although this difference is generally less than 1% (see Chapter 5). However, even the smallest difference will mean that half of the experimental temperature measurements will exceed the numerical predictions, even in the absence of enhanced heating (this assumes the difference is not biased toward an over- or under-prediction of the temperature elevation). As a result, the "cutoff" temperature below which an experimental temperature elevation is presumed to agree with the numerical prediction must be buffered with an additional amount related to this inherent difference between model and experiment.

Using the information in Fig. 3.21 describing pressure amplitude where cavitation activity occurs, we can isolate the range of pressure amplitudes where cavitation activity and enhanced heating should be absent, and we would expect the experimental result to agree with a model which only considers primary absorption. This subset of numerical predictions and experimental results is used to determine the magnitude of the difference between model and experiment that is not related to

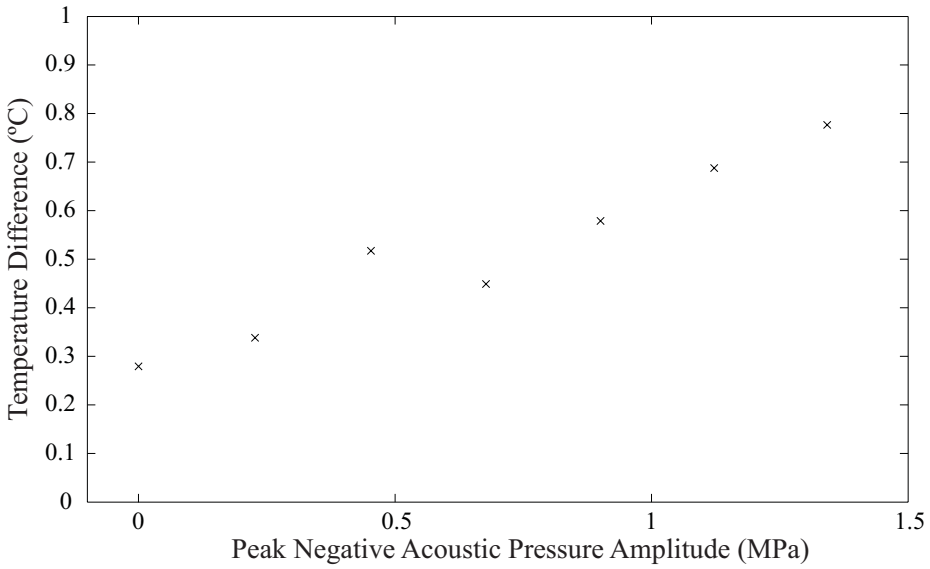

Figure 3.24: Maximum difference between numerical predictions of peak temperature and experimental results as a function of peak negative acoustic pressure amplitude. Each value represents the maximum of 5 measurements which varying in insonation duration.

the enhanced heating effect. Figure 3.24 shows the maximum difference as a function of peak negative acoustic pressure at the focus. The data suggests that there is some dependence of this error on the pressure at the focus. Therefore, a linear fit will be used to extrapolate a value for the maximum error at pressures above 1.4 MPa rather than simply taking the maximum value from the figure. For reference, an extrapolation of the data in Fig. 3.24 results in uncertainty values in absolute temperature of 0.83 °C and 1.28 °C for 1.6MPa and 2.8MPa respectively (the range for which the values are extrapolated).

The final step is to use the numerical predictions and the difference from step 2 to actually identify an enhanced heating effect in the experimental measurements. Figure 3.25 is the percentage of temperature measurements which meet the criteria outlined for enhanced heating, categorized by insonation duration and peak negative acoustic pressure amplitude at the focus.

The data in Fig. 3.25 shares some similarities with the results of the previous section on cavitation activity. The threshold pressure for at least one occurrence of an enhanced heating effect is uniform across insonation times with the exception of the shortest insonation time, 0.1 seconds. There is a threshold pressure at which there is a near certainty that enhanced heating will occur, however it is not as uniformly 100% as compared to the PCD data. The primary difference between the PCD

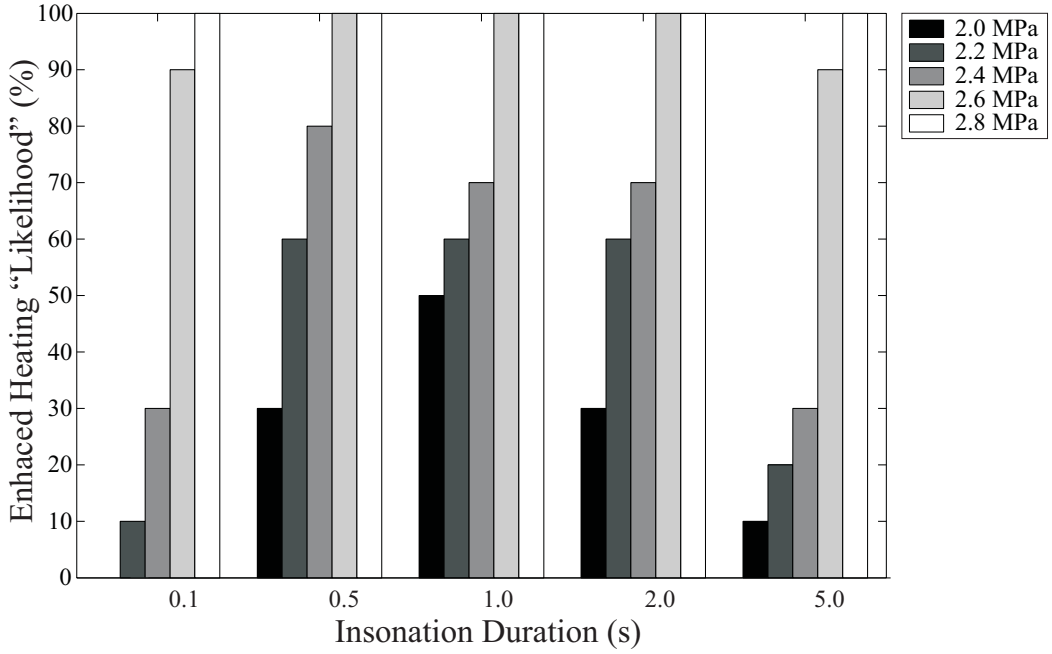

Figure 3.25: Percentage of temperature measurements, categorized by insonation duration and peak negative acoustic pressure amplitude at the focus, whose measured values exceed the numerical predictions.

data and these temperature results is the pressure amplitudes for these thresholds. The threshold pressure for any instances of enhanced heating in the measurement set is approximately 20% higher than what was found for the cavitation activity.

However, of the 30 pressure/insonation duration combinations in Fig. 3.21 where cavitation activity was detected, the number of measurements where enhanced heating is indicated by Fig. 3.25 is the same or within one measurement for 27 (90%) of those same combinations. The majority of the discrepancies occur where there is only one measurement from the entire set where cavitation activity is detected. Some potential reasons for this result have already been mentioned. A low temperature elevation related to enhanced heating may have been discarded for being less than the difference between numerical predictions and experimental measurement used as a cutoff value for identifying enhanced heating. One reason for a low temperature elevation would be that cavitation activity occurs late in the insonation time (as in Fig. 3.19). The values in Fig. 3.21 are independent of the time during insonation when cavitation occurs whereas the peak temperature is affected by what occurs over the entire insonation time. Alternatively, there may simply be an insufficient number of

acoustically-active bubbles to generate a detectable temperature difference.

The remainder of the analysis is nearly identical to that for cavitation activity. The variability in the temperature response can be analyzed as a potential indicator of the threshold pressure for enhanced heating. Figure 3.26 shows the average peak temperature change as a function of peak negative acoustic pressure amplitude and insonation duration. The "average peak temperature change" for each pressure amplitude represents an average of the peak value of each measurement at that pressure amplitude and insonation duration. The error bars represent one standard deviation of those measurements.

As with the cavitation activity results, there is good agreement between the variability in the measurements seen in Fig. 3.26 and the results obtained from evaluating each measurement individually, as shown in Fig. 3.25. The major exception would be at 1.8 and 2.0 MPa for a 1 second insonation duration. The variability at 1.8 MPa is closer to 2 MPa than to 1.6 MPa, suggesting some enhanced heating at this pressure amplitude. However, the analysis for Fig. 3.25 only indicates enhanced heating for 2.0 MPa.

The final analysis is to examine the average peak temperature change for the subset of measurements where enhanced heating is indicated in Fig. 3.25. Figure 3.27 shows the average peak temperature change as a function of peak negative acoustic pressure amplitude and insonation duration for only those measurements which indicated enhanced heating. The temperature elevation due to primary absorption, as calculated by the numerical model, has been subtracted out. This could be considered the "enhanced heating level", analogous to the cavitation level of the previous section. The error bars are the maximum and minimum values at each pressure amplitude.

The results suggest that the average peak temperature change does not vary significantly for a large range of insonation times (0.5 to 2 seconds) for a fixed pressure amplitude. The exception is at 0.1 seconds where this temperature change is approximately 20% of that of the other insonation times. This is consistent with the nature of the enhanced heating seen in the top plot of Fig. 3.18 where the rate of heating declines as the insonation continues. This fact would suggest that as the insonation times grow longer, the increase in the peak temperature rise would slow.

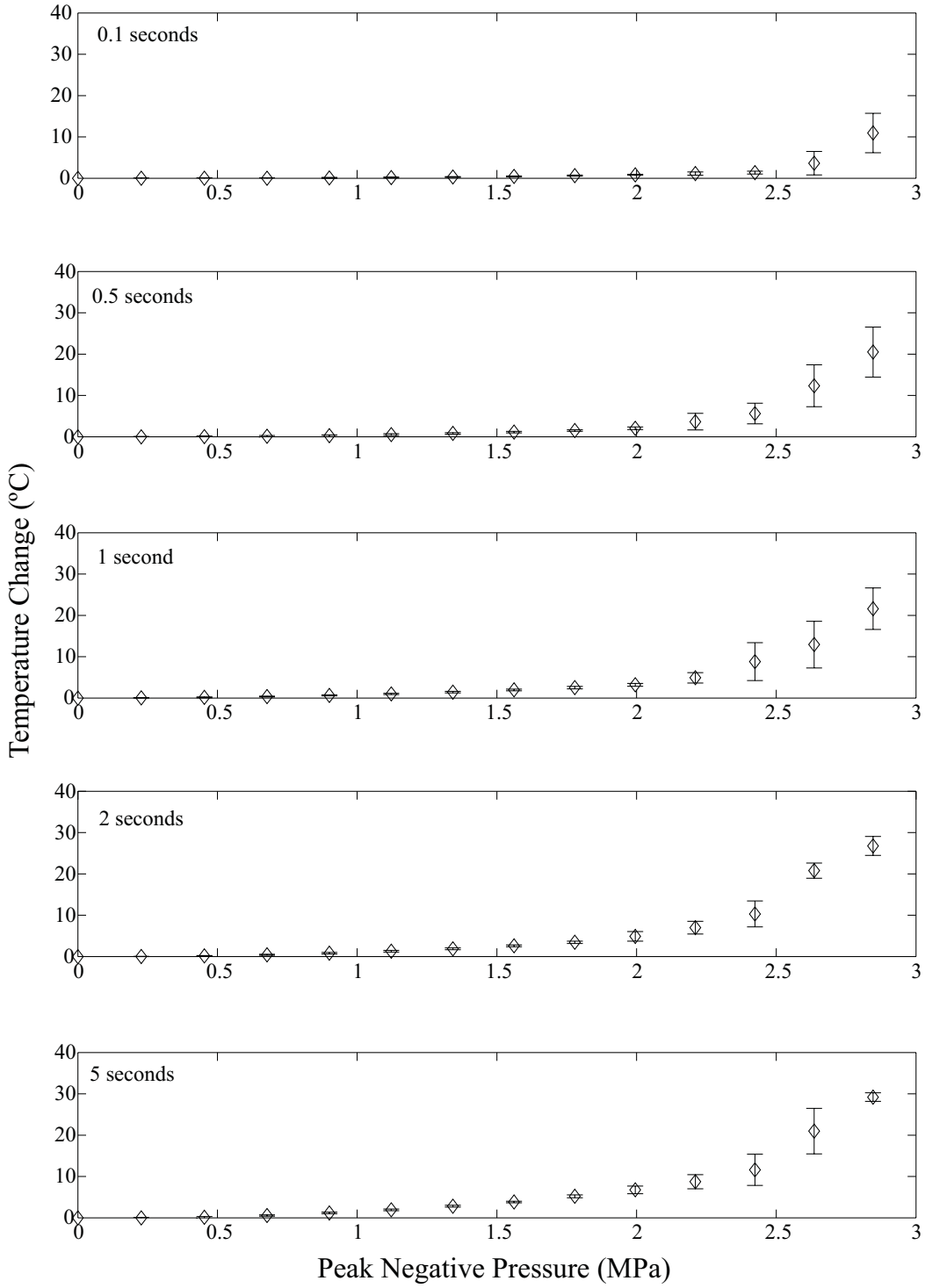

Figure 3.26: Average peak temperature change as a function of peak negative acoustic pressure amplitude at the focus and of insonation duration. Results for every measurement are included regardless of the presence or absence of cavitation activity.

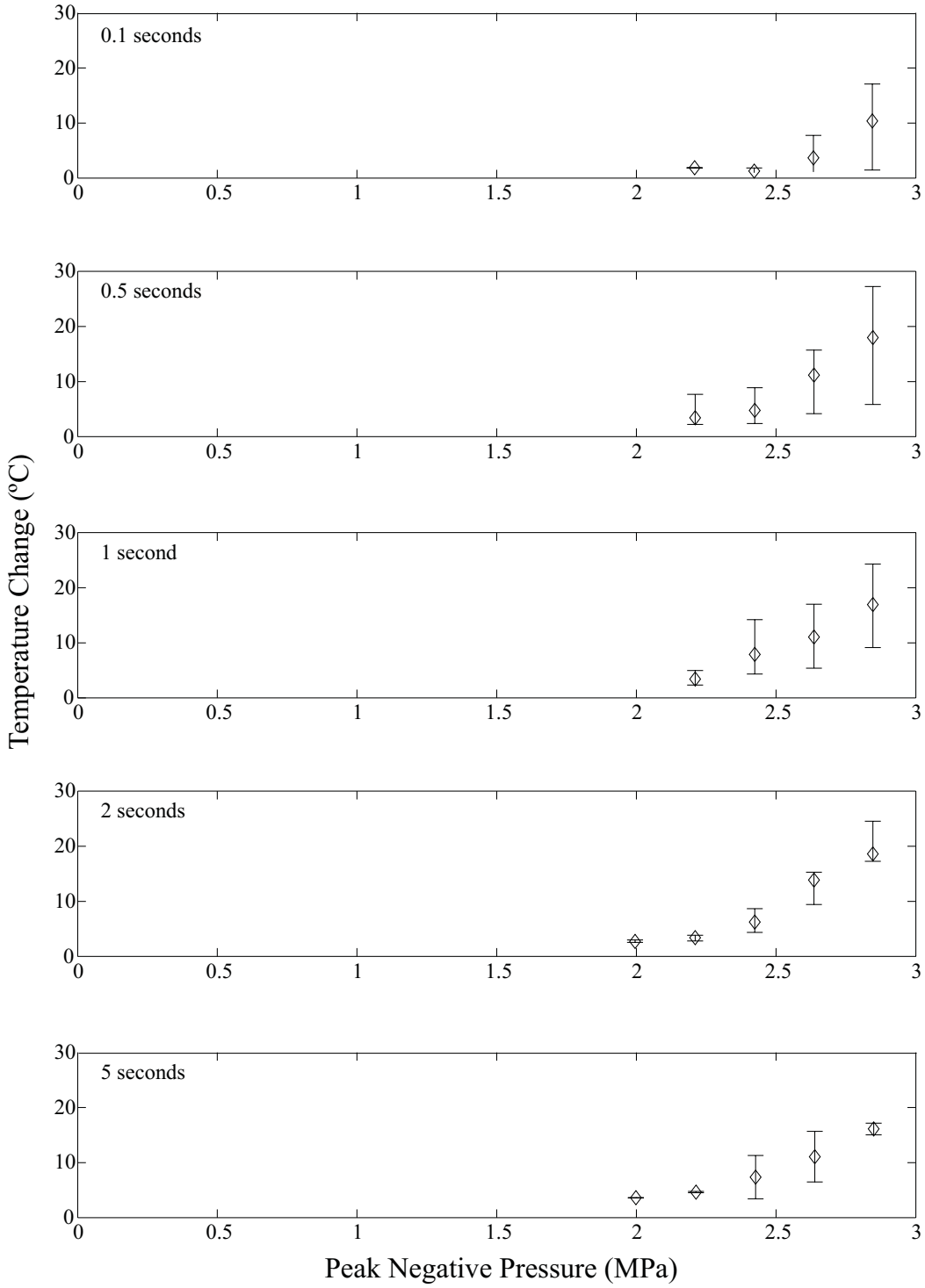

Figure 3.27: Average peak temperature change due to enhanced heating as a function of peak negative acoustic pressure amplitude at the focus and of insonation duration. The temperature elevation due to primary absorption (determined from numerical predictions) has been subtracted from the measured results. Results are based only on those measurements where enhanced heating is detected.

In summary, the results of this section are consistent with those of the previous section for cavitation activity with one exception: the threshold pressure for measurable enhanced heating was found to be higher than the threshold pressure for measurable cavitation activity, given the analysis techniques employed. The effect of insonation duration on those threshold pressures, the primary motivation for the experiments discussed in these two sections, is largely the same, however. For insonation of 0.5 seconds and above, the threshold pressure defined as any occurrence of cavitation activity is mostly unaffected. It is only for very short insonation times of 0.1 seconds that there is a noticeable change the result of which is an increase in the threshold pressure.

It is also true that the threshold pressure for a near-certainty of cavitation activity and enhanced heating are largely *independent* of the insonation duration. In addition this threshold pressure for each of these effects are nearly the same at or just above 2.6 MPa, unlike the threshold pressures for the first occurrences. This is an important result in that it is relevant to therapeutic applications which require some level of repeatability. It is also important when considering cavitation activity as a noninvasive means of monitoring the enhanced heating effect, as there is better agreement between cavitation activity and enhanced heating threshold pressures given this definition, than for lower a likelihood (below 100%) of each effect.

3.6.2 Enhanced Heating Level

The "enhanced heating level" (the additional temperature due to the presence of bubbles) as a function of insonation duration should be considered as well. The data for the magnitude of the enhanced heating level was presented as a part of the enhanced heating threshold discussion, however some additional comments are necessary. Figure 3.27 showed the average enhanced heating level as a function of insonation duration and the peak negative pressure amplitude. These values are shown in Fig. 3.28 and support the earlier statement that insonation duration does not have a substantial effect on the enhanced heating level except for the shortest of insonation times.

This does not mean, however, that the enhanced heating level as a function of insonation duration is not important. Under many circumstances, achieving the required temperature response

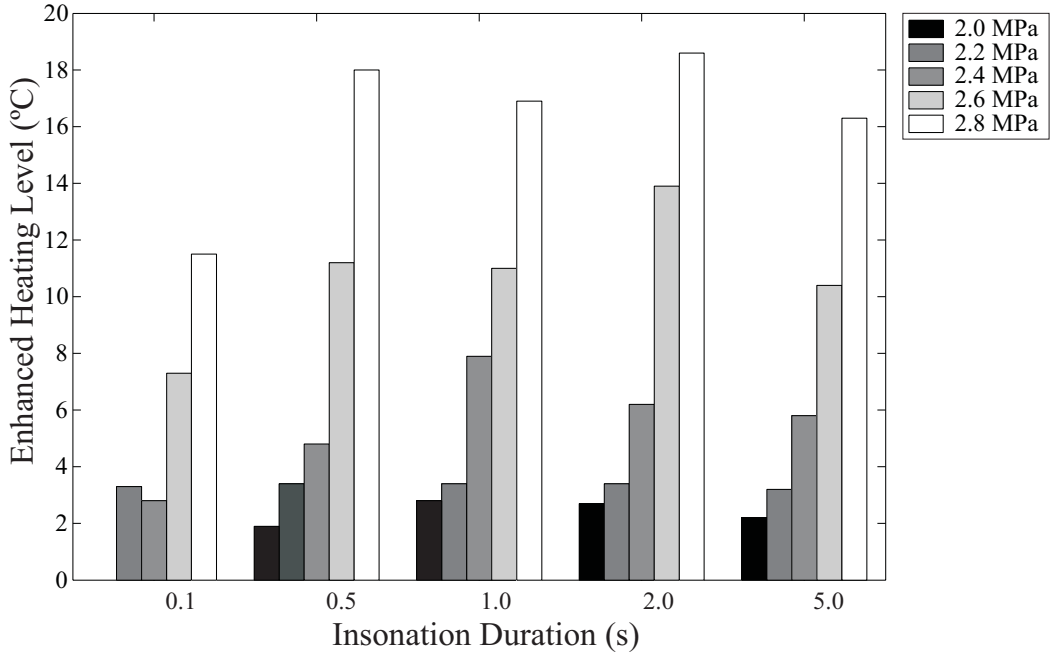

Figure 3.28: Average peak temperature change due to enhanced heating as a function of peak negative pressure amplitude and insonation duration.

with a shorter insonation duration may be beneficial. One potential benefit is a possible reduction in the power requirement for an application of therapeutic ultrasound. More importantly longer insonation times result in an increased peak temperature rise *everywhere* in the field of the source, this being the result of primary absorption. In the event that a temperature rise outside the region of interest (*e.g.*, outside the focal region of a focused source) for the longer insonation duration has a deleterious effect, the shorter insonation time may be a better choice. This assumes that, as a result of the shorter insonation time, a sufficient temperature rise is achieved at the focus due to cavitation activity related localized heating, but not elsewhere. As a result, we are interested in shorter insonation times that produce an equivalent enhanced heating level to their longer duration counterparts.

To realize these localization benefits the *total* temperature rise as a function insonation duration is still ultimately important, which brings us to Fig. 3.29. Therapeutic effects such as tissue necrosis or cauterization are not a function of the enhanced heating level, but of the overall temperature change, and Fig. 3.29 shows the peak temperature change for the measurements in Fig. 3.27 where the temperature rise due to primary absorption has *not* been subtracted. Using this criteria, there

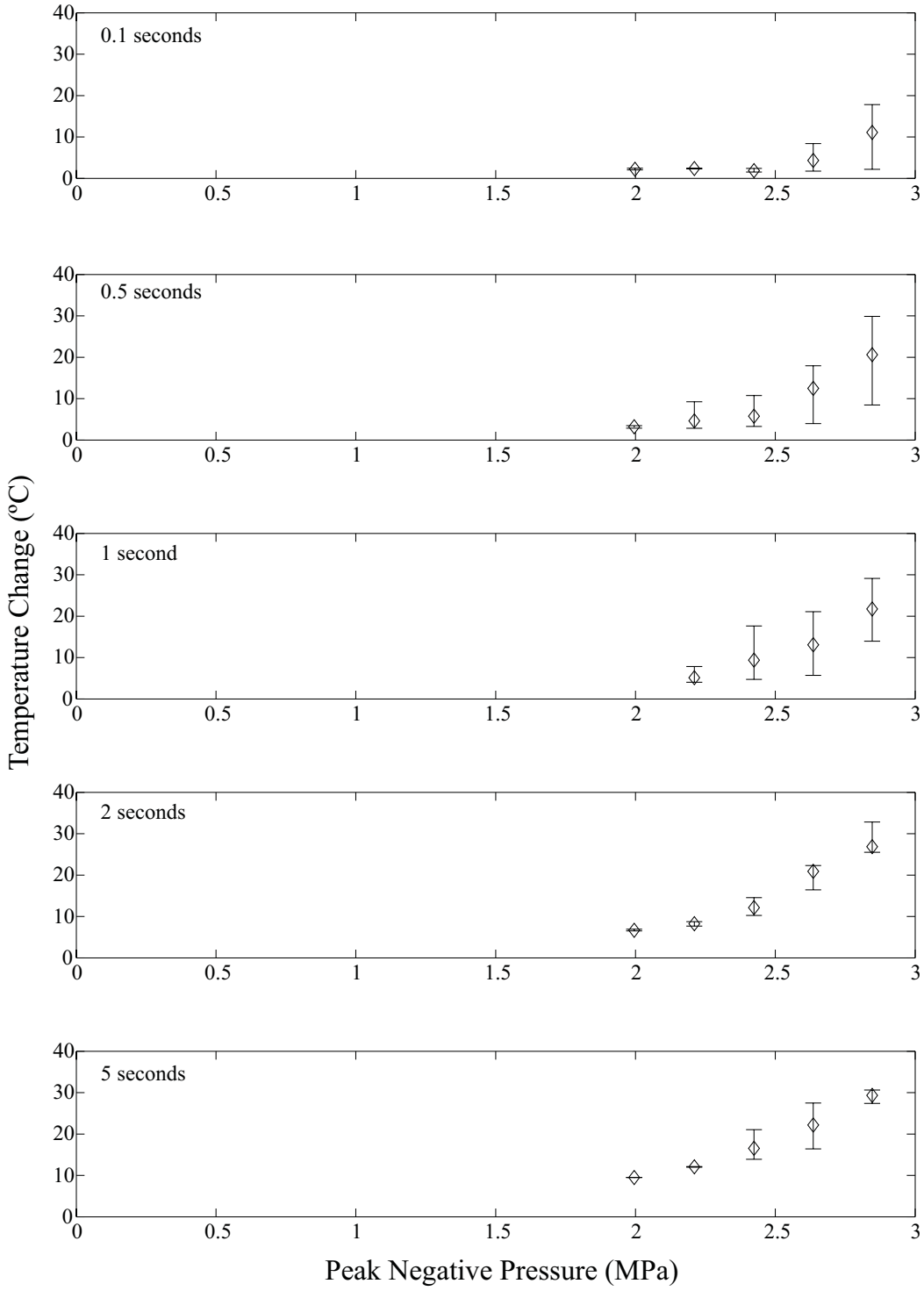

Figure 3.29: Average temperature change due to enhanced heating and primary absorption as a function of peak negative acoustic pressure amplitude at the focus. Results are based only on those measurements where enhanced heating is detected.

is a noticeable, though not substantial, change in the peak temperature change as a function of insonation duration.

The result is that the role of the enhanced heating level as a function of insonation duration is likely to be application dependent. In Fig. 3.29, the temperature rise due to enhanced heating accounts for as much as 70% of the peak temperature change (see Fig. 3.28 for the values of the enhanced heating component). Given the relative parity of the enhanced heating level in Fig. 3.28 excluding an insonation duration of 0.1 seconds, it follows that there will be near parity in total temperature change, as seen in Fig. 3.29. In many cases, therefore, a lower insonation time may be sufficient where the enhanced heating levels reasonably exceeds the requisite therapeutic temperature.

3.7 Summary of Results

An apparatus for the simultaneous measurement of temperature and cavitation activity due to a focused ultrasound transducer in a tissue phantom was presented. Measurements made with this system demonstrate an enhanced heating effect, in which a slight increase in the acoustic pressure leads to a dramatic increase in the temperature elevation. This enhanced temperature rise was strongly correlated to cavitation activity detected in the region of the enhanced heating for both the onset (onset in time and in pressure amplitude) and the relative change in magnitude of each effect. The mean correlation coefficient for 49 measurements at 5 different insonation times, with pressures ranging from 0.0 to 2.8 MPa was 0.95.

What is most important about this correlation are the implications regarding the nature of the cavitation activity. Although we have not yet described how cavitation activity is typically classified in detail, we do know from the description of the PCD system that it is sensitive to a particular range of frequencies. In the next chapter it will be shown that the relationship between the frequency of the radiated sound and the insonation frequency will reveal information about the type of bubbles and bubble motion at work. As a result, the strong correlation between enhanced heating and the detectable cavitation activity for this system will make a strong case for the nature of the cavitation

activity important to enhanced heating.

Investigating the effect of insonation duration on the threshold pressure for enhanced heating demonstrated a minor role for the threshold where a near certainty of enhanced heating exists. This is not true for the threshold for any likelihood of enhanced heating. Here, the threshold is slightly higher for the lowest of insonation times, 0.1 seconds. These results are consistent with the observed thresholds for cavitation activity.

Chapter 4

Cavitation and Bubble Related Heating Mechanisms

The objective of this chapter is to present a sufficient description of bubble dynamics and acoustic cavitation to investigate some of the bubble related heating mechanisms which may play a role in the enhanced heating effect. We will expand the Pennes bioheat transfer equation to include sources of heat generation related to acoustic cavitation, and implement a numerical solution to that modified equation. Accomplishing this requires a theoretical understanding of how bubbles may behave under the influence of an acoustic disturbance, and how that behavior may translate into energy dissipation in tissue, or in our case a tissue-mimicking phantom. Several references will be provided for readers interested in additional details.

Before a gas bubble can be involved in any form of motion it must nucleate, or come into existence. The issue of nucleation in acoustic cavitation, and the stabilization of nuclei is not a subject we directly considered in this research. However, substantial research has been devoted to the topic, particularly with regards to the "variably permeable skin model" [64–68] and the "crevice model" [69–71]. In general these models are concerned with how tiny pockets of gas are stabilized against dissolution in a liquid. For our purposes, we will assume that these nuclei are stabilized in a manner that is unrelated and unimportant to the subsequent motion of the bubble during insonation, as it is this motion that is our primary concern.

Several definitions have been put forth for the term "acoustic cavitation" [23,54,72], most often to differentiate from similar processes which may also occur in the absence of an acoustic disturbance,

e.g., due to boiling. As was stated in Chapter 3, we rely on the following definition of acoustic cavitation: the acoustically forced motion of spherical gas and vapor filled cavities (bubbles) resulting in "a conversion of acoustical to mechanical energy" [54].

Acoustic cavitation research was preceded by the analysis of purely "hydrodynamic cavitation". The rigorous study of hydrodynamic cavitation dates to the 1917 work of Lord Rayleigh [73], who studied the collapse of an empty spherical cavity in water. It was assumed the void simply appeared in water, and proceeded to collapse. Theoretical analysis continued in the absence of an acoustic disturbance through the work of Plesset [74], until Blake [75] investigated the minimum quasi-static pressure change required for "unstable" bubble growth, *e.g.*, a pressure change due to an acoustic disturbance. Several authors have also extended Rayleigh's work to directly consider the motion of a gas or gas-and-vapor filled bubble due to an acoustic pressure field, reviews of which be found in Flynn [53] and Neppiras [21], and Prosperetti [76, 77]. Leighton [24] details the wide range of applications which either take advantage of or seek to mitigate the effects of acoustic cavitation.

Once we have determined the motion of the bubble wall, we are able to evaluate various mechanisms we classify as bubble related heat deposition. There are several ways in which the presence of a bubble or a group of bubbles in motion may lead to additional energy deposition beyond primary absorption, some of which we will consider in this chapter. In considering single bubbles, Devin describes the three primary mechanisms through which a spherical, oscillating bubble may dissipate energy [78]:

(1) "Radiation": Energy radiated through emitted sound waves
(2) "Thermal": Energy transferred during the compression and expansion of the gas
(3) "Viscous": Energy lost through viscous dissipation

Given an acoustic field, each of these damping effects may lead to additional heat deposition in the surrounding medium beyond primary absorption. It may occur directly, as in the case of heat transfer if the bubble becomes hotter than the medium, or indirectly, in the case of radiated sound which is subsequently absorbed by the medium in the same manner as the incident acoustic field. Each of the mechanisms will be considered in greater detail below. Other potential sources of energy deposition which are not evaluated in detail as a part of this research will be described as well.

4.1 Bubble Equilibrium

Before discussing bubble dynamics and acoustic cavitation, a description of a static bubble in the absence of an acoustic field will be employed as a vehicle for introducing terms and presenting a physical picture of the problem. We are considering a gas or gas-and-vapor filled cavity in liquid medium. This cavity, or bubble, is assumed to be spherical, and to remain so during any changes in size. In addition, all other motion, aside from that radial expansion and contraction, is ignored.

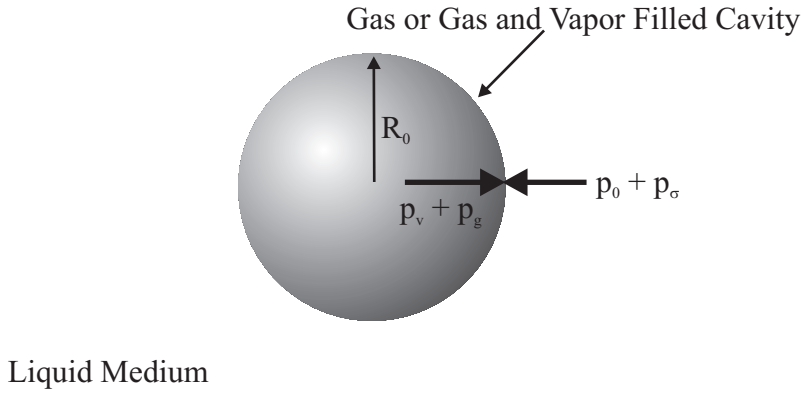

Figure 4.1: The static gas and vapor filled bubble immersed in a liquid. Vapor and gas pressures are balanced by the hydrostatic pressure and surface tension.

Figure 4.1 depicts a gas and vapor bubble in "static equilibrium". In general there is an internal pressure due to the gas, p_g, and vapor, p_v, content as well as an external, hydrostatic pressure, p_0 and surface tension pressure, p_σ where

$$p_\sigma = \frac{2\sigma}{R} \tag{4.1}$$

and σ is the surface tension of the liquid. At some "equilibrium radius", R_0, the internal and external pressures are balanced such that

$$p_{g,e} = p_0 + \frac{2\sigma}{R_0} - p_v \tag{4.2}$$

where $p_{g,e}$ is the particular value of the gas pressure for which the bubble size is stable.

The total internal pressure required to balance the hydrostatic pressure and surface tension in Eq. 4.2 will in fact be higher than the pressure in the liquid just outside the bubble. As a result the bubble will dissolve in and under- or saturated medium in the absence of an acoustic field, a problem originally addressed by Epstein and Plesset [79]. However, our ultimate interest is in the motion of

the bubble given an acoustic field, and dissolution will not be a primary concern. Although not truly stable, this definition of an equilibrium radius will provide a useful reference point.

4.2 Bubble Wall Motion

We are interested in determining the radius as a function of time of a bubble subject to the acoustic field and experimental parameters described in Chapter 3. The level of difficulty of this solution depends on the assumptions that can be made regarding the bubble and the medium. Considerations for the bubble include the contents (gas, vapor) and whether effects such as viscosity and surface tension are important. For the medium, one must determine whether it can be treated as incompressible, and whether it can be represented as a simple Newtonian fluid or if it is more complex, *e.g.*, a viscoelastic medium [80, 81].

Which of the above considerations are important is largely a function of the driving amplitude of the acoustic source and the equilibrium radius of the bubble we are interested in. For example, it is evident from Eq. 4.2 that one factor influencing the importance of surface tension is the equilibrium size of the bubble. Similarly, as the acoustic pressure amplitude is increased, the validity of treating a medium such as water as incompressible decreases.

The largest factor in our choice of a model for the motion of the bubble wall is the uncertainty in two parameters. Although the experiments described in the previous chapter provide qualitative information regarding the amount of cavitation activity as a function of time, they could not provide quantitative information regarding the actual number density and size distribution of the bubbles present. We will also discuss the uncertainty in the choice of the effective shear viscosity of the tissue phantom (which we model as a fluid) in a subsequent section. The uncertainty in each of these two parameters is as much as one or two orders of magnitude. As a result, considerations which may be important in choosing a model for the bubble motion at one end of the parameter range may not be important for the entire range.

In addition, measurements were made over a large range of acoustic pressure amplitudes. This may also influence the assumptions that can be made in evaluating which model for the bubble

motion is appropriate. As a result, we will choose a model that is suitable for each combination of bubble size, viscosity, and acoustic pressure under consideration, recognizing that for some combinations of parameters the model will contain a level of detail that is greater than what is necessary for an accurate solution.

4.2.1 The Rayleigh Model

Arguably the simplest problem relating to the radial motion of a cavity was examined by Rayleigh in 1917 [73]. The problem under consideration was an empty cavity, or void, in a liquid, which simply collapses. The assumptions in his model were:

- The liquid is water and is infinite in extent
- The water can be treated as incompressible
- The cavity simply "appears" in the water
- The external pressure, p_0, is a constant (hydrodynamic - no acoustic)
- The cavity is a void ($p_g = p_v = 0$)
- The effects of viscosity and surface tension are ignored
- The cavity remains spherical during the collapse

Rayleigh's resulting differential equation for the cavity motion is

$$R\ddot{R} + \frac{3}{2}\dot{R}^2 = \frac{p_0}{\rho}, \tag{4.3}$$

where R, $\dot{R}$, and $\ddot{R}$ are the bubble wall radius, velocity, and acceleration respectively. The density of the liquid is represented by ρ. Many subsequent models, including the one we will use in this research, are extensions of this initial work which remove one or more of the assumptions listed.

4.2.2 The "RPNNP" Model

The empty cavity and constant hydrodynamic pressure in the Rayleigh model result in the extinction of the cavity after collapse. While this is an important, fundamental result, it is somewhat of an abstraction and not as relevant to our problem as the case of a gas filled cavity (*i.e.*, a bubble) in the presence of a time-varying acoustic disturbance. Under many circumstances, this physical problem

will yield steady state results, or at a minimum a transient response which lasts longer than a simple collapse. Noltingk and Neppiras [51, 52] first investigated an extension to the Rayleigh model which included an acoustic pressure field, and a gas filled bubble. The remaining assumptions are those used by Rayleigh except as specified here:

- The bubble contains gas which is assumed to obey the perfect gas law
- Temperature and pressure inside the bubble are assumed to be uniform in space
- Mass and heat transfer between the bubble and the liquid are ignored
- Surface tension is included in the analysis for a Newtonian fluid
- There is a time-varying acoustic pressure field

The pressure in the liquid is no longer simply the hydrostatic pressure, but instead includes a time varying component due to an acoustic sound field of frequency, ω:

$$p(t)_\infty = p_0 - p_a \sin \omega t, \tag{4.4}$$

where p_∞ is the total pressure in the liquid. Soon after the work of Noltingk and Neppiras, Poritsky [82] considered the viscous stresses at the bubble-liquid boundary. This, in conjunction with the work of Noltingk and Neppiras, gave rise to the famous "RPNNP" (Rayleigh, Plesset, Noltingk, Neppiras, and Poritsky) equation for the motion of a gas filled bubble in a viscous liquid:

$$R\ddot{R} + \frac{3}{2}\dot{R} = \frac{1}{\rho}\left[\left(p_0 + \frac{2\sigma}{R_0}\right)\left(\frac{R_0}{R}\right)^{3\gamma} - \frac{4\mu\dot{R}}{R} - \frac{2\sigma}{R} - (p_0 - p_a \sin \omega t)\right], \tag{4.5}$$

where γ is the adiabatic exponent of the gas and μ is the shear viscosity of the liquid. Noltingk and Neppiras point out that Eq. 4.5 is also valid in the isothermal extreme ($\gamma = 1$), and for the addition of constant vapor content in the bubble.

Several results from Eq. 4.5 were explored in detail by Lauterborn through numerical integration [83]. Due to the large number of parameters and the required computation time, all the calculations involved an air bubble in water at 20°C. Several solutions were calculated as a function of frequency, equilibrium radius, and acoustic pressure amplitude for bubbles in water. Lauterborn's numerical solutions successfully predicted the bubble response at small and intermediate pressure amplitudes, however the solutions were later described by Keller and Miksis as predicting "unreasonably large amplitudes" or "failing to converge" for large forcing amplitudes [84].

4.2.3 The Keller-Miksis Model

This deficiency was addressed by Keller and Miksis who took into account sound radiated by the bubble by allowing the medium to be compressible [84]. The solution we will use for predicting the motion of the bubble wall is related to the one originally derived by Keller and Miksis, expanding Eq. 4.5 to include not only the effects of acoustic radiation from the bubble, but also the polytropic exponent of the gas, κ. The particular formulation we use is one by Parlitz *et al.* and is written as follows [85]:

$$\overbrace{\left(1-\frac{\dot{R}}{c}\right)R\ddot{R}+\frac{3}{2}\dot{R}^2\left(1-\frac{\dot{R}}{3c}\right)}^{\text{Interial Terms}}=\left(1+\frac{\dot{R}}{c}\right)\frac{P\left(\dot{R},R,t\right)}{\rho}+\frac{R}{\rho c}\frac{\partial P\left(\dot{R},R,t\right)}{\partial t}, \tag{4.6}$$

where

$$P\left(\dot{R},R,t\right)=\overbrace{\left[\left(p_o-p_v-\frac{2\sigma}{R}\right)\left(\frac{R_0}{R}\right)^{3\kappa}+p_v\right]}^{\text{Total Internal Pressure}}-\overbrace{p_0-\frac{2\sigma}{R}-\frac{4\mu\dot{R}}{R}-p_a\sin\omega t}^{\text{Total External Pressure}}, \tag{4.7}$$

and c is the speed of sound in the medium. The numerical results of Lauterborn and Keller and Miksis indicate that this model is valid over a large range of equilibrium radii and acoustic pressure amplitudes, including those relevant to this research.

The additional assumptions in our application that require comment here are the lack of mass transfer and the assumption of a Newtonian fluid. During the relatively long insonation times used in Chapter 3 there is some likelihood that mass transfer between the bubble and liquid will occur. Although we will not include mass transfer in our analysis, *e.g.*, rectified diffusion [62], we will consider a large range of equilibrium bubble radii (described below) which will provide some understanding as to the role of bubble equilibrium radius on bubble-related heating, should bubbles grow during insonation. For most biological tissues and for the tissue phantom materials used in the research, assuming a Newtonian fluid in Eq. 4.6 is an approximation [80, 81]. In reality, these materials may exhibit viscoelastic properties which are not accounted for in the above model, and will not be considered in this research.

4.2.4 Parameter Ranges

Equation 4.6 is a function of several parameters and physical properties. Our objective is to use parameters and properties which match those in our experimental work, however there are some parameters and properties which are not readily determined. In this regard, we are most concerned here with values for the equilibrium radius of the bubbles, R_0, and the equivalent shear viscosity of tissue phantom, μ, which we model as a Newtonian fluid .

We have already noted that there is no direct information from our experimental results regarding the equilibrium size of the bubbles detected by the PCD system. Even if the distribution were known, we are not likely to find that it contains a single equilibrium radius. As a result we must consider Eq. 4.6 in terms of a range of equilibrium radii. Measurements of equilibrium radii *in vivo* indicate that the vast majority of the bubbles exist below 50 μm [86,87]. In addition, a lower limit of 0.1 μm represents the lower bound for bubbles most susceptible to cavitation [63,88,89]. The values will serve as the limits for our numerical solutions.

It is possible to set an upper limit for the shear viscosity through our measured value of the acoustic attenuation. The shear viscosity in the phantom is directly related to absorption, yet the measured attenuation is the contribution of both the absorption and scattering in the tissue phantom. Therefore, we can determine a conservative upper bound to the viscosity by attributing the total attenuation to absorption alone. The attenuation and this upper bound to the effective viscosity will vary based on the phantom recipe. As a lower bound we choose the value for water, which is the primary component and the material with the lowest viscosity in the recipe.

Although we have limited ourselves to a Newtonian fluid in using Eq. 4.6 for the bubble motion, this is an approximation for the experimental tissue phantom material. Although this research will not incorporate non-Newtonian behavior such as shear thinning and viscoelasticity in determining the bubble motion, we will consider a range of values for shear viscosity in solving for the bubble wall motion. We recognize that the non-Newtonian behavior of the tissue rheology during the bubble oscillation is not represented by simply changing the viscosity used in a Newtonian model, however, it will provide insight as to the relative importance of viscosity.

4.3 Single Bubble Heating Mechanisms

Of the many candidate mechanisms for bubble related heat deposition the focus in this research is on the damping mechanisms of single oscillating bubbles. The thermal, viscous, and radiation damping of the *linear* bubble response has been the subject of detailed theoretical and numerical analysis [78, 90–92]. These results will serve as a useful reference point in considering the relative importance of each mechanism as a function of R_0 and μ. However, our numerical analysis will rely on the nonlinear solutions of Eq. 4.6 to calculate the magnitude of the power deposition from these mechanisms.

4.3.1 "Viscous" Contributions to Bubble Related Heating

Power deposition due to viscous dissipation is the result of stresses at the boundary between the bubble and the liquid. Poritsky [82] first incorporated a term representing this boundary stress in Eq. 4.5 and subsequently it has been used to determine the energy deposited in the form of heat [36, 37]. Prosperetti's results indicate that for bubbles with linear oscillations, viscous dissipation will be important at higher frequencies, *i.e.*, those in the megahertz range [90]. Depending on bubble size, viscous damping can be comparable to or greater than that of radiation damping in water. Prosperetti's results are for a bubble in water which corresponds to the minimum value of μ that we are considering, as described in Sec. 4.2.4. We would expect that for the higher values of μ we will consider, the viscous dissipation would meet or exceed this prediction. As a result, it is necessary to consider viscous dissipation as a mechanism for power deposition, keeping in mind the fact that nonlinear oscillations may influence the relative magnitude as compared to other mechanisms.

The stress at the pulsating bubble wall due to the viscosity of the liquid, p_{vis} is

$$p_{vis} = \frac{4\mu\dot{R}}{R}. \tag{4.8}$$

This stress acts over the entire surface of the bubble, $A = 4\pi R^2$, such that $p_{vis} \times A$ represent a force at the bubble interface. As the interface moves with velocity $\dot{R}$ energy is dissipated at a rate of $p_{vis} \times A \times \dot{R}$. As a result, the time-averaged energy deposited per unit time due to viscous dissipation

is

$$D_{vis} = \left\langle p_{vis} \times 4\pi R^2 \times \dot{R} \right\rangle_t = 16\pi\mu \left\langle \dot{R}^2 R \right\rangle_t, \tag{4.9}$$

where $\langle \cdot \rangle_t$ indicated time-averaged values. Equation 4.9 defines what we refer to as the "viscous power deposition", D_{vis}. In the following chapter, Eq. 4.9 is used to calculate the viscous power deposition for the range of R_0 and μ described in Sec. 4.2.4.

4.3.2 "Radiation" Contributions to Bubble Related Heating

Equation 4.6 was chosen over the RPNNP equation to calculate the motion of the bubble wall in part because it includes the damping effect of sound radiation from the bubble, introduced by Keller and Miksis. Any sound that is radiated from a bubble will be absorbed in the same manner as the incident sound field.

We can approximate the sound radiated by the bubble by considering the pressure radiated from any oscillating body where the wavelength of the radiated sound, λ is much larger than the body [93, 94]:

$$p_{sac}(r,t) = \frac{\rho}{4\pi r} \frac{d^2V}{dt^2}, \tag{4.10}$$

where r is the radial distance from the bubble, and V is the volume of the oscillating body. We identify this pressure, p_{sac}, as the pressure due to "secondary acoustic emission" to differentiate from the incident sound field. Equation 4.10 can be readily evaluated for a pulsating sphere:

$$p_{sac}(r,t) = \frac{\rho R}{r} \left(2\dot{R}^2 + R\ddot{R} \right), \tag{4.11}$$

We are interested in the absorption of this radiated sound. If the emitted sound can approximated as a plane wave, the time-averaged acoustic intensity, I_{sac}, can be written as

$$I_{sac}(r) = \frac{\langle p_{sac}^2(r,t) \rangle_t}{\rho c}. \tag{4.12}$$

This plane wave approximation will be valid for $1/kr \ll 1$, where k is the wave number [12]. For the parameters considered here, this requires that the radial location of interest be greater than approximately 25 μm. In the following chapter we will solve the BHTE equation with a spatial resolution of

only 1 mm. As a result we will be considering the intensities at distances where this approximation is reasonable. As in the case of the viscous dissipation we are ultimately concerned with the time-averaged power deposition, D_{sac}. The maximum "secondary acoustic power deposition" is evaluated by considering the total sound radiated by the bubble:

$$D_{sac}^{max} = 4\pi r^2 \times I_{sac} = \frac{4\pi}{\rho c} \langle q_{sac} \rangle_t \,, \tag{4.13}$$

where

$$q_{sac}(t) = \left[\rho R \left(2\dot{R}^2 + R\ddot{R} \right) \right]^2 . \tag{4.14}$$

Unlike viscous dissipation which occurs in a relatively small volume of the medium around the bubble, the absorption of radiated sound will occur in a volume related to the magnitude of the acoustic absorption coefficient. We will be interested in the fraction of total radiated sound absorbed in discrete volumes in the numerical analysis in the next chapter. As a result, we first need to develop an expression for the secondary acoustic power deposition as a function of distance from the bubble.

Table 3.2 lists the measured acoustic *attenuation* of the phantom material as 5.1 Np/m/MHz. Two facts are important to note with regard to this value. First, the measured acoustic attenuation is the result of both classical absorption and the scattering of sound in the phantom, as mentioned in Sec. 4.2.4. Although there will exist some scattering as the sound propagates, it will ultimately be absorbed and lead to additional power deposition. For the purpose of determining the power deposition due to secondary acoustic emission (as well as for the computation of primary absorption), we will use the measured attenuation value as the effective acoustic absorption. Indeed, this choice for an effective "absorption" yields good agreement between theory and experiment for heating due exclusively to primary absorption (*e.g.*, Fig. 2.6). Second, the measured attenuation is a function of the acoustic frequency, and in particular, the magnitude increases with increasing acoustic frequency. This will lead to more rapid absorption of radiated sound that contains one or more harmonic components, and the power deposition will consequently occur in a notably smaller volume around the bubble.

For materials with frequency *independent* attenuation (or for a mono-frequency sound wave), the

pressure at an arbitrary distance from the bubble will be subject to exponential attenuation [12, 19]:

$$p_{sac}(r,t) = \frac{\rho R}{r}\left(2\dot{R}^2 + R\ddot{R}\right)e^{-\alpha_f r}, \tag{4.15}$$

where α_f is the frequency independent attenuation or the attenuation at the single frequency of the sound wave. To incorporate frequency *dependent* attenuation in the calculation of the secondary acoustic power deposition we must use the Fourier transform of Eq. 4.14 and an exponential loss term that is a function of frequency

$$q^*_{sac}(r,f) = \left[\int_{\infty}^{\infty} q_{sac}(t)e^{-\imath 2\pi f t}dt\right]e^{-2\alpha(f)r}, \tag{4.16}$$

where $\alpha(f)$ is the frequency-dependent attenuation of the tissue phantom. By evaluating Eq. 4.16 at an arbitrary radial distance from the bubble, and taking the inverse Fourier transform of the result, we have an expression for the attenuated power at that distance:

$$P_{sac}(r) = \frac{4\pi}{\rho c}\left\langle q^*_{sac}(r,t)\right\rangle_t. \tag{4.17}$$

The resulting secondary acoustic power deposition, D_{sac}, is a function of radial distance from the bubble is

$$D_{sac}(r) = D^{max}_{sac} - P_{sac}(r). \tag{4.18}$$

4.3.3 "Thermal" Contributions to Bubble Related Heating

The final damping mechanism to consider is thermal. Unlike viscous or radiation damping, heat transfer may occur both to and from the bubble. As a result, it is not as immediately evident that this process will result in a net heat deposition from the bubble. As the bubble expands due to the acoustic field, the gas in the bubble will generally cool and heat transfer to the bubble will occur. The statement assumes the bubble contents and the liquid were originally in thermal equilibrium. As the the bubble contracts, the temperature in the bubble will generally rise, resulting in heat transfer from the bubble.

Prosperetti showed that despite the large contribution of thermal damping to the total bubble damping at low frequencies, it plays a relatively minor role at megahertz frequencies [90]. In addition, it has been shown that the net heat transfer in many cases favors heat deposition *to* the

bubble [92], although even this effect has been shown to be small [92, 95]. Although heat transfer between the bubble and the liquid may in fact occur to the potential benefit or detriment of bubble enhanced heating, the relative importance with respect to heat deposition from viscous and secondary acoustic emission is not likely to be significant. Consequently, we will limit our analysis to viscous dissipation and acoustic radiation.

4.4 Additional Heating Mechanisms

Other potential sources of energy deposition include surface oscillations and multiple-bubble scattering. Initial observations of surface oscillations on bubbles during noninertial cavitation were made by Kornfeld and Suvorov [96]. These oscillations can lead to radiated sound from the bubble, typically at frequencies lower than that of pulsation [97]. Non-spherical motion may also lead to greater viscous dissipation. For the purposes of this research, we are considering only spherical oscillations of the bubble, thereby neglecting heating contributions due to these surface oscillations.

Multiple-bubble scattering is a process which may enhance or reduce the energy deposition in the region of interest. Sound scattered by bubbles at the focus of an ultrasound source may in fact lead to additional acoustic absorption in the area of interest. Energy that would otherwise pass through the focus is instead redirected back to or near this area due to scattering. Behaving in this manner, the bubbles could be considered a form of additional focusing mechanism. It can also be thought of as increasing the effective path length of sound transmission at the focus.

This process is not guaranteed to result in additional sound absorption at the focus, however. The presence of bubbles in the near prefocal area may also serve to "shield" the geometric focus of the source from the incident sound by scattering away from the focus. Research by Watkin *et al.* showed that the location of a HIFU induced lesion, an indicator of the location of the focus, will actually move toward the acoustic source in the presence of large amounts of cavitation activity, an indication that the bubbles are preventing the sound from reaching the geometric focus [61]. This could be detrimental for two reasons: (1) even if sufficient heating for the desired effect occurs at this new "focus" or region of highest temperature change, it may not be in the desired location and

(2) even if the change in focus/lesion location is accounted for, it may not be at the location of maximum primary absorption, reducing overall efficiency.

This research will not consider the effects of multiple bubble scattering. From a modeling perspective this interaction is it beyond the scope of this work. From a practical or applications perspective, it may even be desirable to keep this effect to a minimum and attempt to rely on other mechanisms for the reasons noted.

4.5 Types of Cavitation Activity

The nature of bubble motion is often divided into two classifications: noninertial (or stable) and inertial cavitation activity. This distinction may be useful to us in associating the nature of the cavitation activity with the power deposition mechanisms we will calculate in the next chapter, viscous dissipation and secondary acoustic emission. This discussion is with respect to our insonation frequency of 1 MHz. The linear resonance radius for linear bubble oscillations, given by [24]

$$\omega_0^2 = 3\kappa P_0 \frac{1 + 2\sigma/P_0 R_0}{\rho R_0^2} - \frac{2\sigma}{\rho R_0^3}, \tag{4.19}$$

at 1 MHz, and for the material properties of the tissue phantom is approximately 3.72 μm. For the purposes of this discussion, we will refer to super-resonant bubbles as those with an equilibrium radius greater than this resonance radius. Conversely, sub-resonant possess equilibrium radii less than resonance size.

4.5.1 Noninertial Cavitation

Noninertial cavitation can often be identified by a relatively repetitive radial motion of the bubble wall. The motion may or may not be linear, and the each consecutive cycle may or may not be truly identical, however the general nature of the motion is to be repetitive and may last for many cycles. The bubble motion is largely controlled by the “stiffness” of the gas inside the bubble and the resulting oscillations would typically be considered gentle when compared to inertial cavitation. The threshold pressure for noninertial cavitation is the threshold pressure for nucleation. That is,

unless the circumstances meet the additional pressure threshold requirements of inertial cavitation described in the next section, the motion of any bubble which nucleates will fall in the category of noninertial cavitation.

The mass transfer over any single cycle of bubble oscillation is not likely to be significant. However, due to the large number of cycles often associated with noninertial cavitation, mass transfer can often play a role over the life of the bubble. Through a process called rectified diffusion, the mass of the gas in the bubble will increase over time as the bubble oscillates [62]. As a result, the equilibrium radius increases. Rectified diffusion is only a factor if noninertial cavitation is found to be important *and* the change in equilibrium radius during insonation substantially affects the magnitude of either the viscous dissipation or the secondary acoustic emission.

We will first consider the importance of viscous dissipation and secondary acoustic emission for large, noninertial bubbles in water. For reference, we can consider the results of Prosperetti for air bubbles undergoing linear oscillations in water [90]. How factors such as the higher viscosity values in our parameter range and nonlinear, but noninertial, oscillations may impact these results will be considered as appropriate.

For super-resonant bubbles on the order of 10 μm, the dominant dissipation mechanism in water is acoustic radiation. The relative importance of this mechanism as a source of power deposition will depend on how the radiated sound is absorbed, *i.e.*, is the absorption coefficient sufficiently large that the sound is absorbed in a localized volume around the bubble that leads to noticeable heating (see Sec. 4.3.2). Although Prosperetti's results indicate that the damping due to viscous dissipation is smaller than that of acoustic radiation, this result is for liquids with the viscosity of water. We expect that as the viscosity is increased in our range of parameter values, the relative importance of viscous dissipation as a source of power deposition may become more important as well. In addition, a higher phantom viscosity will influence the bubble motion and subsequently the acoustic radiation, typically by damping the motion and the radiated sound. Therefore, power deposition due to both viscous dissipation and secondary acoustic emission must be included when considering large, noninertial bubbles.

As the bubbles become small with respect to the resonance radius, viscous dissipation becomes increasingly important, and acoustic radiation for linear oscillations becomes relatively unimportant for air bubbles in water. If the oscillations are nonlinear, there is the potential for greater power deposition from radiated sound due to the increased absorption for increasing frequency. Therefore, we may still want to consider secondary acoustic emission in addition viscous dissipation for these small bubbles. We will discuss in the following section, however, that it is the smaller bubbles that are most susceptible to inertial cavitation. It may be that for the pressure amplitudes where enhanced heating is observed, the oscillations of smaller bubbles are always inertial, making power deposition from small, noninertial, bubbles irrelevant.

4.5.2 Inertial Cavitation

Inertial cavitation is marked by explosive bubble growth followed by a violent collapse. The motion is not linear, and at times will not last more than a few, or even one cycle. After expanding to two or more times the equilibrium radius, the gas pressure in the bubble (whose gas content we assume to be constant) drops to near the vapor pressure and has little influence on the initial collapse phase. At this phase in the collapse, the essentially vapor filled bubbles behave much like the Rayleigh cavity described earlier, in that the motion is dominated by the inertia of the collapsing fluid. The motion is always nonlinear.

Inertial cavitation occurs at higher acoustic pressures than noninertial cavitation for a given equilibrium radius and liquid properties. The acoustic pressure amplitude must not only be large enough to nucleate a bubble, but be large enough to "drive" a bubble to inertial motion, in other words to induce rapid growth followed by a violent collapse. As an additional result, super-resonant bubbles are not likely to experience inertial cavitation. These large bubbles simply respond too slowly to the change in acoustic pressure to experience the explosive growth and subsequent collapse.

For sub-resonant, behaving inertially, acoustic radiation becomes far more important than viscous dissipation as a means of power deposition. This can be attributed to the broadband emission of sound at the collapse. The power deposition from this broadband emission is greatly enhanced

by the frequency dependent acoustic attenuation of the tissue phantom. As a result, not only is substantial energy radiated as sound, it is absorbed in a substantially smaller, localized volume.

It is worth repeating here that the PCD system, as noted in Chapter 3, is most sensitive to acoustic radiation above 2 MHz. In the description of that system we also mentioned that although it may be sensitive to large, noninertial bubbles oscillating nonlinearly, the PCD system is almost certainly primarily sensitive to small inertial bubbles which emit broadband noise upon collapse. The magnitude of any radiated sound from noninertial bubbles, oscillating linearly, is likely to be severely reduced, due to the limited bandwidth of the PCD system.

4.6 Summary

We have chosen an implementation of the Keller-Miksis nonlinear model for the motion of a gas-and-vapor filled bubble in a Newtonian fluid for our analysis of bubble dynamics. In the next chapter, we will solve this equation numerically for a range of values for the equilibrium radius of the bubble and the viscosity of the tissue phantom. The range for each of these parameters represents the uncertainties in these values in the experimental work, as well as the fact that the bubble population during insonation is not uniform in space. The solutions for the motion of the bubble wall will then be used to calculate the power deposition due to viscous dissipation and the absorption of the secondary acoustic emission from the bubble using Eq. 4.9 and Eq. 4.18, respectively.

In addition, we have described how the nature of the cavitation activity may influence the mechanisms for power deposition. Of particular importance is the influence on the radiated sound as this pertains to the sensitivity of the PCD system. Small inertial bubbles, large or small noninertial bubbles oscillating linearly, and large or small noninertial bubbles oscillating nonlinearly will all radiate sound with different frequency components. As a result, the PCD is a tool that can both determine the onset and magnitude of the cavitation activity, and provide insight as to the nature of the cavitation activity as well. Specifically we expect it to be more sensitive to small inertial bubbles or possibly small and large noninertial bubbles oscillating nonlinearly.

Through the relationship between the enhanced heating effect and observed cavitation activity

seen in Sec. 3.5, the PCD system also becomes a tool for gaining insight into the nature of the cavitation activity that is responsible for the enhanced heating effect. In the next chapter we will be particularly cognizant of small inertial bubbles and noninertial bubbles with nonlinear oscillations when evaluating power deposition from viscous dissipation and secondary acoustic emission.

Chapter 5

Numerical Method and Results

In the previous three chapters a set of theoretical models and experimental results related to heating in a tissue phantom were assembled. In Chapter 2 models for the temperature rise due to primary absorption of an ultrasound field were discussed. Chapter 3 presented experimental temperature measurements where the temperature changes were the result of, at a minimum, primary absorption, and in some cases bubble-related heating mechanisms as well. The preceding chapter described theoretical models for power deposition mechanisms which are the result of ultrasound induced bubble motion. The task we address here is how to bring together these individual components in a manner in which some understanding of the experimental findings is gained from a theoretical model.

Chapter 2 introduced the concept of an enhanced heating effect, where a measured temperature rise exceeded the theoretical predictions of the bioheat transfer equation (BHTE) when only primary absorption is considered (*e.g.*, Fig. 2.7). The experimental evidence in Chapter 3 makes a strong case for the role of bubbles as the source of the temperature discrepancy. What remains to be seen is whether a "reasonable" number of bubbles, as sources of additional power deposition, can in fact account for the magnitude of this discrepancy, *i.e.*, the enhanced heating effect. The answer to this question resides in the magnitude of the bubble-related power deposition terms from the previous chapter. Also of interest is whether additional insight can be gained into the type of cavitation at

work (inertial or noninertial) through modeling the problem.

5.1 Numerical Method Overview

In this chapter we will present a numerical solution to a modified Pennes bioheat transfer equation which includes bubble-related sources of power deposition. Ideally we would incorporate the power deposition from a known number of bubbles of one or more known equilibrium sizes, R_0, and at locations which are also known, for any given experiment we wish to simulate. In other words, each of these bubble parameters would ideally be measured as readily as parameters such as sound speed and acoustic frequency. A more accurate simulated temperature change, incorporating the effects of primary absorption *and* bubble-related power deposition terms from the previous chapter, could then be compared to experimental temperature measurements. The validity of the model and the argument for bubble enhanced heating could then be evaluated based on the outcome of this comparison.

In *reality*, obtaining data regarding these bubble parameters (number, size distribution, location) is far more difficult than measurements of sound speed and acoustic frequency. The uncertainty in the appropriate tissue phantom viscosity value, μ, to use in Eq. 4.6 when solving for the bubble motion has been discussed, and this uncertainty affects our ability to make definitive choices in modeling as well. Without access to quantitative measurements of these bubble parameters, and knowledge of the effective viscosity of the tissue phantom, we must take an alternate approach. The approach, in the most general terms, can be divided into three steps:

(1) Calculate the temperature rise due to primary absorption with a numerical solution to the BHTE.

(2) Calculate the power deposition from viscous dissipation and secondary acoustic emission as a function of R_0, μ, and the acoustic pressure amplitude, p_a for a single bubble.

(3) Use the power deposition values calculated in Step (2) to determine the number of bubbles required to account for the difference in the measured temperature rise and that computed from Step (1).

The approach, while straightforward, involves several smaller steps, which will be outlined now, and can be seen in Fig. 5.1. We will first attempt to provide a general understanding of the approach,

avoiding most details of the numerical implementation. Those details will follow in a separate section.

5.1.1 Calculating the Temperature Change Due to Primary Absorption

Our objective in this first step is to implement a model for the temperature rise due to primary absorption. This implementation is important for two reasons: (1) it provides the foundation to which we will add bubble-related power density terms and (2) it allows us to compare numerical calculations to experimental results and determine where the primary absorption model is valid, as well as quantify the magnitude of the additional temperature change that is the result of bubble-related heating.

The application of the second motivation is seen in Figure 5.2, reprinted here from Chapter 2. To review, this figure shows the peak temperature change as a function of peak negative acoustic pressure at the focus for numerical simulations (BHTE) and experimental measurements. The details of the insonation duration experiments were explained in Chapter 3 and the details of the numerical implementation will be presented in this chapter. In this first step, we are concerned with implementing a numerical solution that allows us to quantitatively predict the heating behavior seen prior to the onset of bubble enhanced heating. For the example presented in the figure, this corresponds to pressures below 2 MPa.

Determining the temperature rise due to primary absorption is a two step process, as outlined briefly in Chapter 2:

(1) Solve for the steady-state pressure in the tissue phantom based on the known experimental parameters for the acoustic source, the propagation geometry, and material properties.

(2) Incorporate a power density due to primary absorption, q_{us}, based on the calculated pressure field in Step (1) in a numerical solution for the BHTE.

Although this discussion is not specific to a particular geometry, developing the process in the context of a specific coordinate system will simplify the presentation. We will use a cylindrical coordinate system in anticipation of the approach taken by the numerical implementation. The

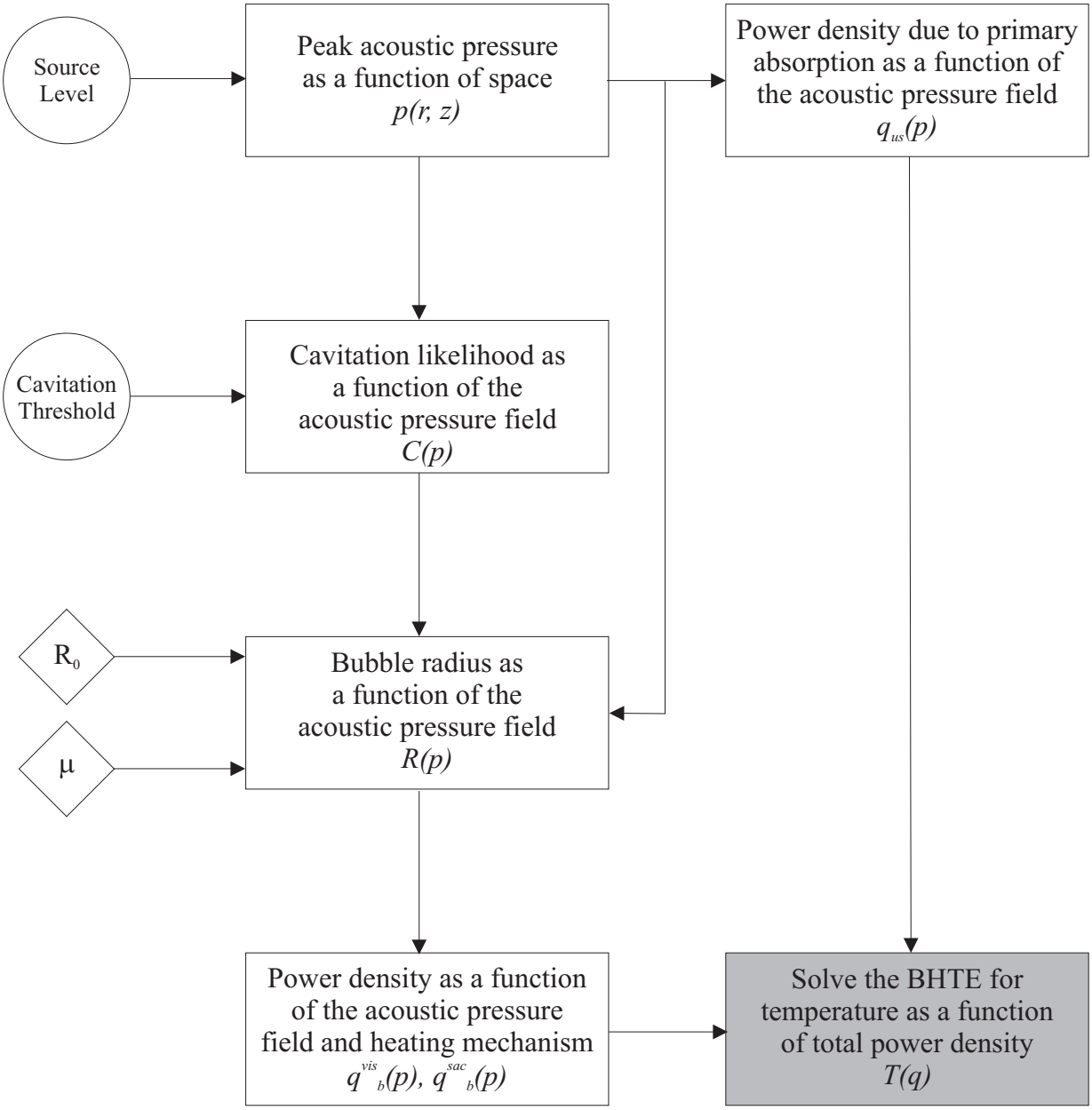

Figure 5.1: General flow of the calculations presented in this chapter. Items in circles represent parameters obtained from experimental measurements. Items in diamonds represent parameters specified solely for numerical purposes. Calculations begin with the pressure field as a function of space, based on a pressure at the acoustic source. Given the calculated pressure field, we can calculate the likelihood of cavitation activity, as well as the motion of the bubble (radius vs. time) as a function of space. With the bubble motion and expected locations, we can then determine the power density due to bubble-related heating, which when added to the contribution of primary absorption, allows us to solve the BHTE for a bubble enhanced temperature rise.

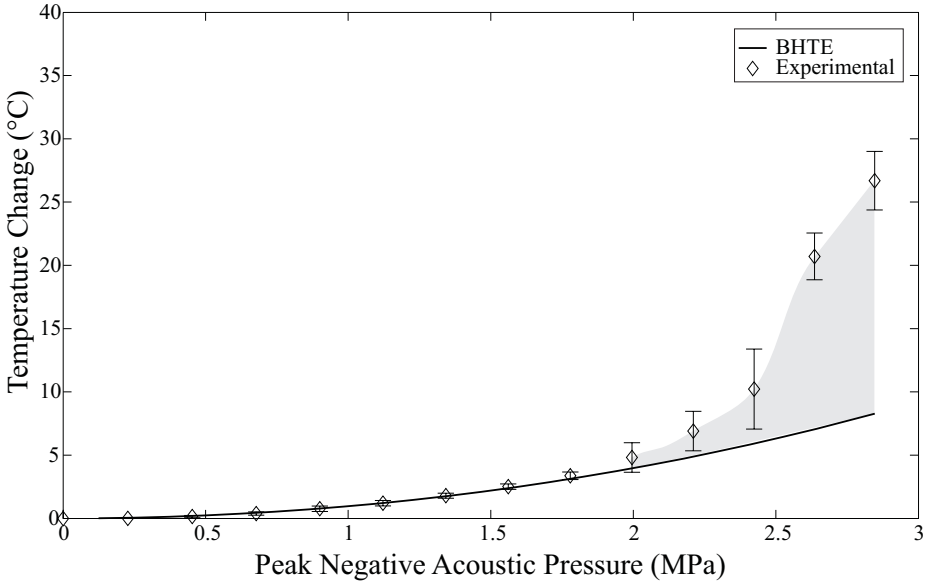

Figure 5.2: Comparison between experimental and simulated (BHTE) temperatures as a function of focal peak negative pressure for a 1 second insonation at 1 MHz. Simulated temperatures are from a finite-difference time-domain implementation. The shaded portion indicates the temperature change due to bubble-related heating.

form of the BTHE we will consider is

$$\frac{\partial^2 T}{\partial r^2} + \frac{1}{r}\frac{\partial T}{\partial r} + \frac{\partial^2 T}{\partial z^2} - \frac{\rho_t C_t}{K_t}\frac{\partial T}{\partial t} + q_{us}(r,z,t) + q_b(r,z,t) = 0, \tag{5.1}$$

where r and z are the radial and axial locations respectively and q_b is the power deposition per unit volume related to the presence of bubbles. The remaining symbols are as defined for the original BHTE. It will be argued in the details of the numerical implementation that symmetry in the θ coordinate is appropriate and this is reflected in Eq. 5.1. We have neglected the perfusion and metabolic heat generation terms which are not applicable in our tissue phantom.

The power density due to primary absorption, q_{us}, is a function of space as it is derived from the pressure field, itself a function of space. Primary absorption is also a function of time in that we will occasionally calculate a solution to the BHTE for a time that is longer than the insonation duration. Our primary interest is in the peak temperature change, a condition achieved at the end of insonation, though we may also wish to observe the post insonation cooling as well. For obvious reasons q_{us} should only be applied during insonation, however, and the magnitude of q_{us} over that interval is constant. The last term, q_b, represents the contributions from bubble-related heating mechanisms. When considering only primary absorption, we neglect this term.

5.1.2 Contributions from Bubble-Related Heating

In this second step, we determine the power deposition from individual bubbles due to viscous dissipation and secondary acoustic emission as a function of R_0, μ, and p_a. First, we must solve a second order differential equation (the Parlitz equation, Eq. 4.6). This will be discussed in the numerical implementation section. What is important to note is that we will divide the range of viscosity values and equilibrium bubble sizes into discrete values for evaluation, identified as $[\mu_1 \dots \mu_i \dots \mu_M]$ and $\left[R_{0,1} \dots R_{0,j} \dots R_{0,N}\right]$ respectively. The Parlitz equation is solved for every combination of viscosity and bubble size values, $(\mu_i, R_{0,j})$, at insonation pressure, p_a, which results in a $\mu_M \times R_{0,N}$ matrix, $\mathbf{R}$, of radius versus time ($r-t$) "curves". An $r-t$ curve calculated for a viscosity μ_i and bubble equilibrium size $R_{0,j}$ is identified as $\mathbf{R_{ij}}$.

This entire process is repeated as a function of the acoustic pressure amplitude, p_a. The range of acoustic pressure amplitudes of interest will be bounded by the measured threshold pressure for cavitation activity (lower limit) and the highest experimental focal pressure where enhanced heating was observed. We again divide the parameter range in discrete values, $[p_{a,1} \dots p_{a,k} \dots p_{a,L}]$, creating L matrices of $r-t$ curves, where a particular curve at viscosity, μ_i, equilibrium size $R_{0,j}$, and acoustic pressure amplitude, p_a^k can be identified as $\mathbf{R_{ij}^k}$.

The last step involves numerical calculations of viscous and secondary acoustic power deposition, Eq. 4.9 and Eq. 4.18, for every $r-t$ curve from the previous step resulting in two $\mu_M \times R_{0,N}$ matrices of scalar values ($\mathbf{V}$ and $\mathbf{S}$ for viscous dissipation and secondary acoustic emission, respectively), for every pressure amplitude. We can determine the total power deposition as a function of μ_i, $R_{0,j}$, and p_a^k by adding the results of $\mathbf{V_{ij}^k}$ and $\mathbf{S_{ij}^k}$.

5.1.3 Solving for the Number of Bubbles Required for Enhanced Heating

With knowledge of the viscous and secondary acoustic power deposition, the objective of this final step is to incorporate those mechanisms in the BHTE (Eq. 5.1), represented as a power density, q_b. The implementation of q_b is the point in this analysis where our procedure diverges from the "ideal" situation described earlier. If we did know the number of bubbles, their size distribution and

locations, as well as the phantom viscosity, we could use the results from the last step to calculate q_b on a per bubble basis and discretely add each bubble contribution to the BHTE at the appropriate location. Since we do not have that information, the intent here is to solve for the number of bubbles required to simulate the measured temperature rise. This requires making assumptions regarding the bubble locations, size distribution, and the phantom viscosity. We can then comment on whether this number of bubbles is reasonable, and how that number varies if different assumptions are made for the other parameters.

The steps we will take are not unlike what we would need to do if we did not know the acoustic pressure as a function of space when determining the power density due to primary absorption, q_{us}. We could still make temperature predictions by making assumptions regarding the spatial variation (the "shape") of q_{us}. We would then infer the pressure as a function of space based on the known relationship between the pressure and q_{us} (Eq. 5.11).

In our actual application, we will make assumptions regarding how the bubble-related power density, q_b, varies as a function of space. The complexity in the bubble problem is that while there is only one relationship between q_{us} and the acoustic pressure (Eq. 5.11), there are several possible relationships between q_b and the number of bubbles required to generate the power deposition. This is because there are different bubble responses, and subsequently power deposition and power density, as a function of R_0 and μ. As a result, we must consider specific cases regarding R_0 and μ in determining q_b.

5.2 Numerical Implementation: Primary Absorption

We are interested in the temperature, as a function of space and time, in the tissue phantom. The finite difference time domain (FDTD) code used to calculate the acoustic pressure and the temperature is derived from code described and used extensively by Hallaj [49]. Our modifications consist mainly of altering the geometry and material properties to match experimental conditions and, more importantly, to incorporate additional sources of power deposition in the BHTE.

The FDTD method relies on discrete differences in place of partial derivatives in the wave equa-

tion and the BHTE by dividing the spatial and time domains into discrete spatial grid points and discrete time steps. The particular implementation chosen here is an *explicit* method where only known values from past time steps are required. Several texts are available which detail the general implementation of the FDTD technique [98, 99], however important aspects of the implementation will be described in this chapter.

Accurate FDTD modeling of wave propagation requires sufficient resolution in space and time with respect to the relevant length and time scales, where the resolution is defined by the separation of the grid points and the time steps. The original implementation of FDTD solutions to wave propagation problems is generally attributed to Yee [100] and his solution of Maxwell's equations for electromagnetic fields. This method has since been adapted to several applications of acoustics [101–103].

An accurate representation of a sinusoidal waveform generally requires a minimum of 10-12 spatial points per wavelength. For a source frequency of 1 MHz that does not see substantial harmonic generation during propagation, and a speed of sound on the order of 1600 m/s for the tissue phantom, we will be using a grid separation of 0.1 mm. The maximum time step where the stability of the solution is assured is, in general, a function of the spatial grid separation and the speed of sound for wave propagation. For an absorbing wave equation, a simple expression for the maximum stable time step is not available. However, prior consideration of the stability (stability occurs when perturbations due to errors such as round-off error tend to decay rather than grow), of this solution has demonstrated that for our grid separation and material properties, a time step of 1×10^{-8} s is sufficient [49].

These discretization requirements can demand substantial computing resources (on the order tens of hours or days for results such as those seen in Fig. 5.2), depending on their size with respect to the duration and spatial extent of the solution domain. The domains required here will be large enough that this resource concern is a consideration. However, the nature of our experimental geometry is such that cylindrical symmetry can be used to reduce the number of spatial dimensions to just two, which will substantially reduce the resources needed. The cylindrical coordinate system

is oriented with the acoustic axis of the source transducer as the z (axial) axis. Radial position is measured from this axis. In addition, we will see that the pressure solution reaches steady-state in a fraction of the insonation times under consideration, making it necessary to model only a portion of this time. Once the pressure solution has reached steady state, the magnitude of the primary absorption will not change with continued modeling. Despite the attempts at making the computation reasonable, the demands are still high.

Fortunately, this high degree of temporal resolution employed for the wave equation is not required for the BHTE solution. The rate of change of the temperature response is orders of magnitude slower than the insonation frequency. As a result a time step on the order of 1×10^{-3} s was found to be sufficiently small. We will maintain the resolution in space, primarily to simplify mapping the spatial pressure results as a source term to the BHTE (q_{us}).

5.2.1 Finite-Difference Time-Domain Solution: Pressure

To review from Chapter 2, the equation used to solve for the pressure in both the tissue phantom and water is a nonlinear equation, presented here in cylindrical coordinates:

$$\frac{\partial^2 p}{\partial r^2} + \frac{1}{r}\frac{\partial p}{\partial r} + \frac{\partial^2 p}{\partial z^2} - \frac{1}{c^2}\frac{\partial^2 p}{\partial t^2} + \frac{2\alpha}{c\omega^2}\frac{\partial^3 p}{\partial t^3} + \frac{\beta}{\rho c^4}\frac{\partial^2 p^2}{\partial t^2} = 0, \tag{5.2}$$

where r is the radial location and z is the axial location. The desired solution domain, in time and space, is divided into a discrete grid where $p_{i,j}^n$ represents the pressure, $p(r_j, z_i, t_n)$, at location indices (i, j) and time step n. The mapping to spatial location and time from these indices is

$$z_i = z_0 + (i-1)\delta_z, \tag{5.3}$$

$$r_j = r_0 + (j-1)\delta_r, \tag{5.4}$$

$$t_n = t_0 + (n-1)\delta_t, \tag{5.5}$$

where δ_r, δ_z, and δ_t represent the space between grid points and time steps respectively. The

difference equations used for Eq. 5.2 are second order accurate in space and time [49,99]:

$$
\begin{aligned}
\frac{\partial p}{\partial r} &= \frac{1}{2\delta_r}\left(p^n_{i,j+1} - p^n_{i,j-1}\right), \\
\frac{\partial^2 p}{\partial r^2} &= \frac{1}{\delta_r^2}\left(p^n_{i,j+1} - 2p^n_{i,j} + p^n_{i,j-1}\right), \\
\frac{\partial^2 p}{\partial z^2} &= \frac{1}{\delta_z^2}\left(p^n_{i+1,j} - 2p^n_{i,j} + p^n_{i-1,j}\right), \\
\frac{\partial p}{\partial t} &= \frac{1}{2\delta_t}\left(3p^n_{i,j} - 4p^{n-1}_{i,j} + p^{n-2}_{i,j}\right), \\
\frac{\partial^2 p}{\partial t^2} &= \frac{1}{\delta_t^2}\left(p^{n+1}_{i,j} - 2p^n_{i,j} + p^{n-1}_{i,j}\right), \quad \text{“centered” forumlation} \\
\frac{\partial^2 p}{\partial t^2} &= \frac{1}{\delta_t^2}\left(2p^n_{i,j} - 5p^{n-1}_{i,j} + 4p^{n-2}_{i,j} - p^{n-3}_{i,j}\right), \quad \text{“right-sided” forumlation} \\
\frac{\partial^3 p}{\partial t^3} &= \frac{1}{2\delta_t^3}\left(6p^n_{i,j} - 23p^{n-1}_{i,j} + 34p^{n-2}_{i,j} - 24p^{n-3}_{i,j} - 8p^{n-4}_{i,j} - p^{n-5}_{i,j}\right).
\end{aligned}
\tag{5.6}
$$

Two formulations for the second time derivative are shown. For the explicit method only one unknown term, representing the future pressure value is permissible. With several time derivatives in the equation, one most be chosen to contain this reference to the future value. The second time derivative in the D'Alembertian in the wave equation is chosen because the numerical solution was found to behave best in the original implementation [49].

Solution Domain

Figure 5.3 shows the geometry of the spatial domain for the simulations presented in this chapter. It represents a slice along the axial and radial axes, measure by the discrete indices r_j and z_i. A radial index of 1 represents the axis of symmetry, in this case, the acoustic axis. An axial index of 1 indicates the point in the transducer furthest from the focus. The shaded region indicates the portion of the domain with the properties of the tissue phantom. The remaining portion of the domain is modeled as water. The spatial resolution is 0.1 mm, or approximately 15 pts/wavelength for the material properties of the phantom, at 1 MHz (see Table 5.1).

The curve in the leftmost portion of the figure represents the grid locations of the source transducer face. The source transducer pressure values are specified along this curve as a function of time. The driving waveform at the transducer face may vary based on whether the simulation represents a pulsed or CW configuration, the duration of the insonation, and additional source param-

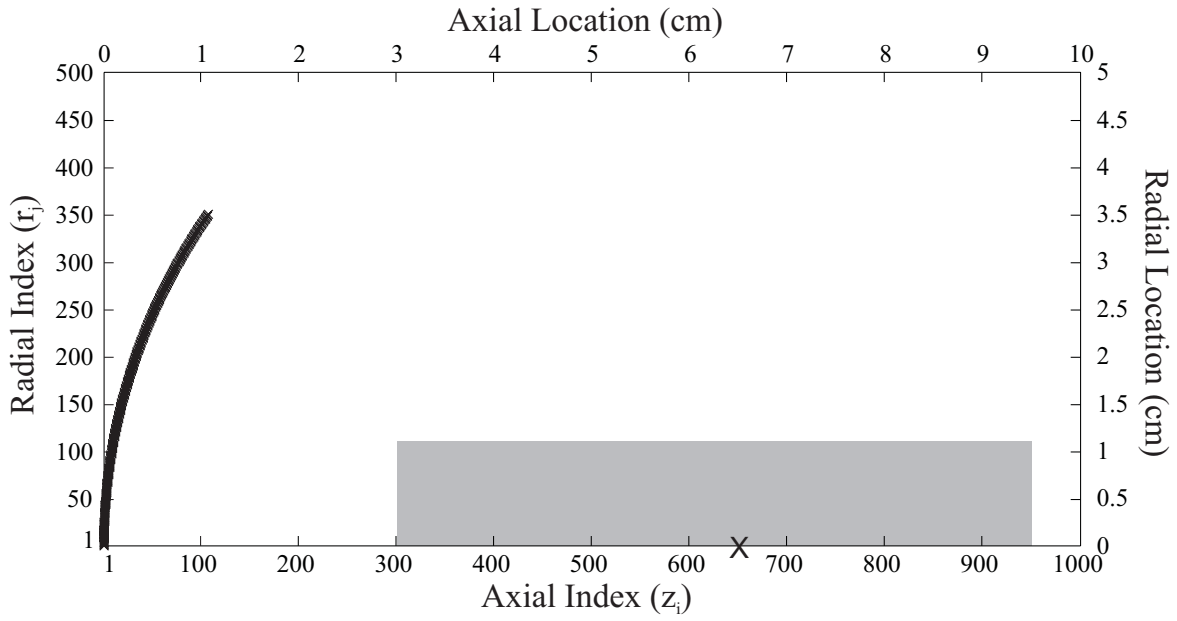

Figure 5.3: The geometry of the FDTD pressure solution domain. The coordinates are shown as the discrete radial and axial indices. The shaded region represents the portion of the domain occupied by the phantom. The symbols on the left which form a curve are the locations corresponding to points on the source transducer. The 'x' represents the location of the focus.

eters. The focus, defined as the location of the peak positive acoustic pressure, will vary somewhat depending on the material properties and the geometry of the tissue phantom. A typical distance for the geometry and material properties of these simulations is at a depth of 3.5 to 4 cm in the tissue phantom. The 'x' in Fig. 5.3 represents this general location at a distance of 3.5 cm.

In general it may be necessary to solve this problem for two time domains: (1) short (< 100 cycles) pulses where the transient response is desired or (2) long ($> 10^5$ cycles) insonation times where a steady-state pressure field is reached long before the full insonation time expires. In the case of (2) we will conserve time and computing resources by only calculating a solution for the fraction of the insonation time necessary to reach steady-state.

Initial and Boundary Conditions

The initial condition in all simulations is a pressure value of zero everywhere. This is not required, however, and with proper saving of variables a simulation could be resumed from past results. The boundary condition at every boundary except the axis of symmetry (radial index of 1), is an "absorbing boundary condition" (ABC) which minimizes reflections. This represents the fact that

we are only modeling a portion of the test chamber. In fact, the focused nature of the source means reflections are primarily a concern only at the "far" boundary with respect to the transducer ($z_i = 951$). Using the ABC, the vast majority of the energy which reaches a boundary is numerically dissipated rather than reflected, as is appropriate here. The particular absorbing boundary employed here was originally used by Mur [104]:

$$\begin{aligned} \frac{\partial p}{\partial r} - \frac{1}{c}\frac{\partial p}{\partial t} &= 0, \\ \frac{\partial p}{\partial z} - \frac{1}{c}\frac{\partial p}{\partial t} &= 0. \end{aligned} \tag{5.7}$$

For cylindrical symmetry, the boundary condition at $r = 0$ ($r_j = 1$) is simply

$$\frac{\partial p}{\partial r} = 0. \tag{5.8}$$

Source Pressure "Calibration"

A primary concern regarding the comparison of FDTD simulations to experimental results involves "calibrating" the source pressure in the simulations to the experimental source pressures. The FDTD simulations specify the transducer explicitly. Ideally the experimental transducer pressure would be directly known as well. However, we are unable to directly measure the pressure at the transducer experimentally with the equipment available. Our closest measure of the transducer pressure experimentally is the voltage at the input to the transducer. The coincides with the output of the matchbox described in Chapter 3, so it is referred to here as the matchbox voltage, V_m.

In order to compare the FDTD simulations to experimental results in the phantom, we must determine the relationship between the pressure at the transducer and the matchbox voltage. This can be accomplished by comparing experimental and numerical results where we are confident both are valid. Experimentally, this means measurements of the acoustic pressure in water, using the calibrated PVDF hydrophone described in Chapter 3. From the simulations the relationship between the transducer pressure, p_t, and the pressure anywhere in the field can be determined. By comparing the measured pressure at some field point with predicted values from the FDTD solution representing the same conditions, we can determine the relationship between the matchbox voltage and the pressure at the source. For example, if we were to consider the peak positive pressure at

the focus, and drive the transducer at a voltage where we know the propagation remains linear, we would expect the following to hold:

$$\begin{aligned} P_f^{pk+} &= k_1 V_m^{pk+} \quad \text{Experimental relationship,} \\ P_f^{pk+} &= k_2 P_s^{pk+} \quad \text{Numerical relationship,} \end{aligned} \tag{5.9}$$

where P_s^{pk+} is the peak positive source pressure specified in the FDTD solution. The relationship is then very simple:

$$P_s^{pk+} = \frac{k_1}{k_2} V_m^{pk+} \tag{5.10}$$

Eq. 5.10 allows us to determine the appropriate source pressure to use in simulations involving the tissue phantom based on the matchbox voltage associated with a particular experimental measurement. Figure 5.4(a) shows the measured P_f^{pk+}, obtained in water, as a function of matchbox voltage and the computer pressure, P_f^{pk+}, as a function of source pressure, each with linear fits whose slope represents k_1 and k_2 respectively. For reference, the results of the analysis in this figure are values of $k_1 = 0.1404$ MPa/V, $k_2 = 24.548$, such that $P_s^{pk+} = 0.0057 V_m^{pk+}$.

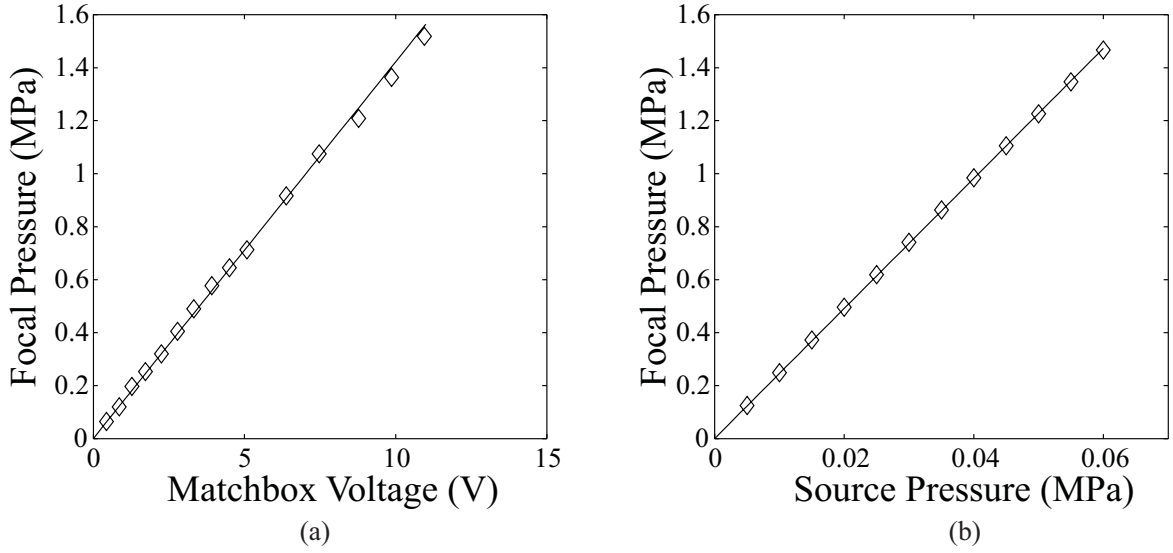

Figure 5.4: Peak positive acoustic pressure at the focus of the source transducer: (a) measured in water, as a function of matchbox voltage (experimental results) and (b) the pressure at the face of the source transducer (numerical simulations)

All measurements and simulations were performed in water only. The experimental measurements were made at the focus of the transducer by averaging 100 waveforms sampled by a digital oscilloscope (Model 9450, 150 MHz, 8-bit resolution, Lecroy, Chestnut Ridge, NY), and taking the

peak positive value of this average. Simulations use the measured matchbox voltage as the driving pressure waveform, scaled appropriately for a range of transducer pressures, again because is the closest representation of the experimental transducer pressure available. This waveform is shown in Fig. 5.5 and remains true to this form with the exception of a scaling for the range of data seen in Fig. 5.4. The entire solution domain has the properties of water, specifically: ρ = 1000 kg/m^3, c = 1500 m/s, α = .0253 Np/m/MHz, and β = 3.5.

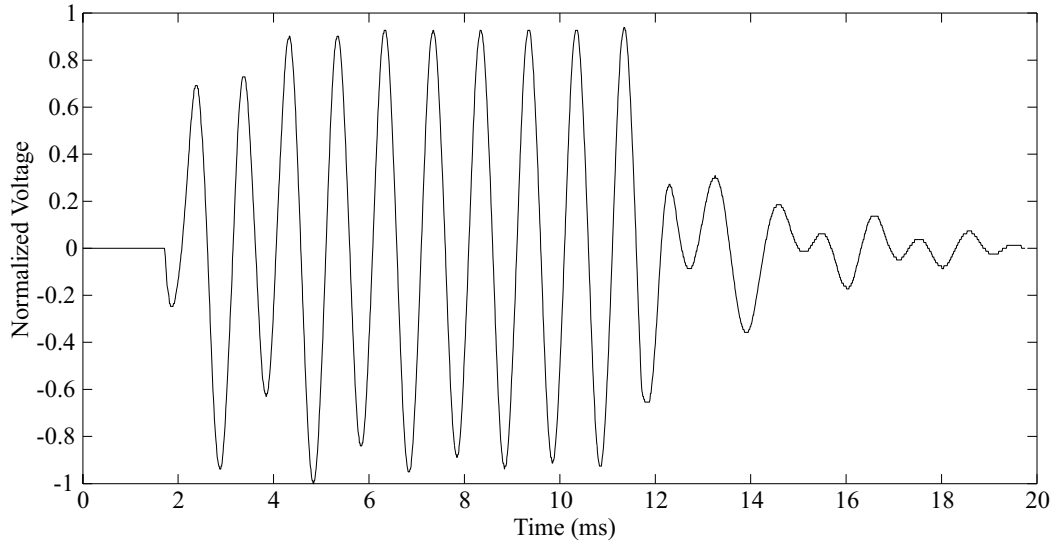

Figure 5.5: The voltage measured at the input to the source transducer during measurements with the PVDF hydrophone. The waveform was used as the source pressure in numerical simulations, scaled to the appropriate pressure amplitude.

It should be noted that this result assumes that the relationship between the matchbox voltage and the source pressure remains linear for the entire range of experimental pressures. Due to the relatively fragile nature of the PVDF hydrophone, this relationship could be experimentally verified for only 65% of the range of pressures used. For the upper 35% of the experimental pressures we must assume that this relationship remains linear.

Solution Method

The motivation for calculating a pressure solution is to determine the power deposited per unit volume due to primary absorption. All calculations of the acoustic pressure for this purpose are performed in much the same way. Often the only difference between simulations is the amplitude

of the acoustic driving pressure. Occasionally, material properties will be changed to match new phantom recipes and on rare occasions, the geometry will be updated to reflect changes in the tissue phantom size. Because the solution reaches steady-state in a fraction of even the shortest of insonation times, changes do not need to be made in the pressure simulations to account for changes in insonation duration.

As was mentioned in the general description of the FDTD method, these simulations use grid and time separations of $\delta_r = \delta_z = 0.1$ mm, and $\delta_t = 1 \times 10^{-8}$ s. A sample of the transducer source condition use in the simulations is shown in Fig. 5.6. For each simulation, this waveform is scaled to the desired source pressure. With a steady-state source condition at the transducer, the pressure field will reach steady-state as well, barring any changes in the environment or geometry during insonation. If the absorbing boundary conditions accomplish their intended purpose, the pressure solution will reach steady-state at approximately the time it takes for the wave to propagate to the farthest distance from the source transducer in the solution domain. For our experimental domain of approximately 5 x 10 cm and the speed of sound of water and the phantom being approximately 1500 m/s and 1600 m/s, respectively, the solution is expected to reach steady-state in 60-80 μs. As a conservative implementation, the simulations are allowed to progress for 100 μs. As mentioned, this feature means that the pressure solution does not depend on the insonation time. As a result, the simulation results for a particular source pressure can be used for all BHTE simulations at that amplitude, independent of insonation duration.

The material properties relevant to the pressure solution for water and the tissue phantom are listed in Table 5.1. The majority of the experiments, and therefore the simulations, were performed with the recipe for “Agar-2”. Any simulation results using properties for “Agar-1” will be specifically noted.

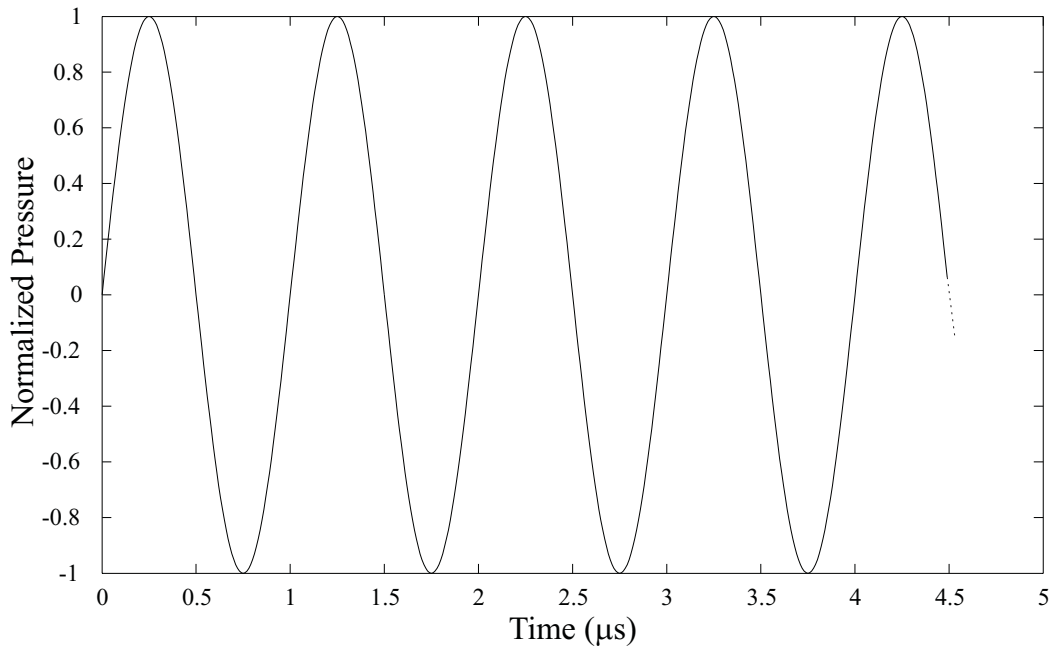

Figure 5.6: A portion of the source waveform used in numerical simulations of the pressure field during CW-insonation. The waveform is applied at each discrete point in the FDTD solution representing the transducer location, and scaled to the desired source pressure.

Material Property	Water	"Agar 1"	"Agar 2"
Density (kg/m^3)	1000	1005	1003
Sound speed (m/s)	1500	1560	1588
Absorption (Np/m)	0.0253	18.2	5.066
Nonlinearity coefficient	3.5	4.4	4.4

Table 5.1: Material properties required for the FDTD pressure solution.

5.2.2 Primary Absorption Power Deposition

From Chapter 2 the equation for the instantaneous power deposition, per unit volume, due to primary absorption is

$$q_{us}(r,z,t) = \frac{2\alpha}{\rho c \omega^2}\left(\frac{\partial p}{\partial t}\right)^2. \tag{5.11}$$

In order to fully decouple the pressure and heat transfer solutions, a time-averaged value of Eq. 5.11 is used. The last 10 acoustic cycles of the pressure simulation are taken as a reasonable basis for determining the time-averaged value. The discrete form of Eq. 5.11 is

$$q_{i,j}^{us} = \frac{2\alpha_{i,j}}{\rho_{i,j} c_{i,j} \omega^2}\left(\frac{1}{2\delta_t}\right)^2 \sum_{n=1}^{N}\left(3P_{i,j}^{n} - 4P_{i,j}^{n-1} + P_{i,j}^{n-2}\right)^2 \tag{5.12}$$

where N is the number of times steps averaged.

Figure 5.7 shows two plots of the power density due to primary absorption, q_{us}, as a function of radial and axial location, for two acoustic pressure amplitudes. Figure 5.7a shows q_{us} for a peak positive and peak negative acoustic pressure amplitude at the focus of 0.125 MPa. Figure 5.7b is an identical solution with a peak positive pressure amplitude of 2.84 MPa and a peak negative pressure amplitude of 2.64 MPa. These pressure amplitudes are near the upper and lower limits of those used in the temperature solutions. The axial location is with respect to the *phantom* not the transducer. The radial location is with respect to the acoustic axis of the source. The solution is calculated in the half-radial domain, as indicated previously, due to cylindrical symmetry. This half solution is mirrored in each plot to better illustrate the complete field.

The main peak in the power density occurs at the focus of the pressure field, as would be expected. The peak values are 57 kW/m^3 and 28 MW/m^3 for plots (a) and (b) respectively. The intermediate peaks and ripples represent the near-field interference of the pressure field. The results are nearly identical, except of course, for the magnitude of the power density, despite some nonlinearity in acoustic pressure (as evidenced by the disparity in the peak positive and negative amplitudes listed) at focus for the data shown in Fig. 5.7b. Equation 5.11 indicates that, if the incident sound is mono-frequency and can be represented as a plane wave, $q_{us} \approx 2\alpha p_{pk}^2$. This suggests we should expect q_{us} to scale approximately as p_{pk}^2. These two plots represent a change in peak pressure at

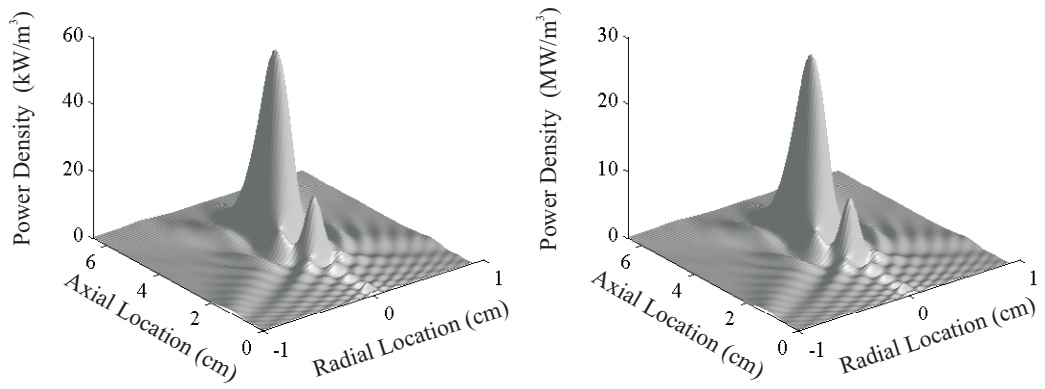

Figure 5.7: Power density due to primary absorption as a function of axial and radial location for two FDTD solutions to the wave equation: (a) based on a peak positive and negative acoustic pressure amplitude of 0.125 MPa and (b) based on a peak positive and negative acoustic pressure amplitude of 2.84 MPa and 2.64 MPa, respectively, at the focus.

the focus of ~22 times, therefore, we would expect q_{us} in Fig. 5.7b to be on the order of 484 times that of Fig. 5.7a. The actual value is 486.

5.2.3 Finite-Difference Time-Domain Solution: Bioheat Transfer Equation

The numerical implementation of the BHTE is analogous to, though computationally much simpler than, the pressure solution. This is true for multiple reasons:

(1) The rate of change of the temperature response is substantially slower than the period of the acoustic frequency in the pressure solution.

(2) The highest order derivative is of order two (vs. three)

(3) The solution domain can be limited to the tissue phantom.

Although we maintain the same spatial discretization, the relatively slow rate of change of the temperature response with respect to the acoustic frequency means that the resolution in time as compared to the pressure solution may be reduced by orders of magnitude. Specifically, a time step of 1 ms is sufficient for stability and accuracy [49]. Lower order derivatives generally reduce the number of terms that need to be calculated, given the same order of accuracy. Lastly, the spatial solution domain can be reduced not in resolution but in size. Although the water path is important to the pressure solution, it simply serves as a large reservoir of constant temperature as compared

to the tissue phantom region. As a result, we can reduce the solution space to just the phantom for the BHTE, using a constant temperature condition at the water boundary.

We are interested in the solution to the modified Pennes equation shown in Eq. 5.1, repeated here for convenience:

$$\frac{\partial^2 T}{\partial r^2} + \frac{1}{r}\frac{\partial T}{\partial r} + \frac{\partial^2 T}{\partial z^2} - \frac{\rho_t C_t}{K_t}\frac{\partial T}{\partial t} + q_{us}(r,z,t) = 0. \tag{5.13}$$

The discretized partial derivatives are the same as those for the pressure except for $\partial T/\partial t$ where a centered difference is used to determine the next temperature value in time:

$$\frac{\partial T}{\partial t} = \frac{1}{2\delta_t}\left(T_{i,j}^{n+1} - T_{i,j}^{n-1}\right). \tag{5.14}$$

The discretized form of q_{us} was shown in Eq. 5.12.

Solution Domain, Initial and Boundary Conditions

As was mentioned above, the solution domain for the BHTE equation is limited to the region of the tissue phantom. This is represented by the shaded region in Fig. 5.3. The large reservoir of water surrounding the phantom serves as an excellent constant temperature boundary condition, making calculations in water unnecessary. The initial condition is simply to use the ambient temperature at every point.

5.2.4 Results: Primary Absorption

Figure 5.8 shows two plots of the temperature change at the end of insonation as a function of radial distance off-axis and axial distance in the phantom . They are the result of using the power density seen in Figure 5.7 where the acoustic pressure amplitudes at the focus were (a) 0.125 MPa and (b) 2.84 MPa peak positive and 2.64 MPa peak negative. The material properties used in the BHTE simulations are listed in Table 2.1. The two source terms in Figure 5.7 are nearly identical in shape (though not magnitude) and the resulting temperature responses are nearly identical as well. The primary difference is in the peak temperature change with is 0.02 C and 9.8 C for plots (a) and (b) respectively. The primary difference between the temperature plots and their respective source

term plots are that the ridges where there was interference in the pressure field, and in turn q_{us}, are mitigated in the temperature response due to the smoothing effect of conduction. In general, the models in Chapter 2 suggest the temperature change should be proportional to the intensity, and therefore the power density due to primary absorption, q_{us}. The ratio of the two peak temperatures is 486, the same value as for the two peak values of q_{us} in Figure 5.7 which is consistent with this expectation.

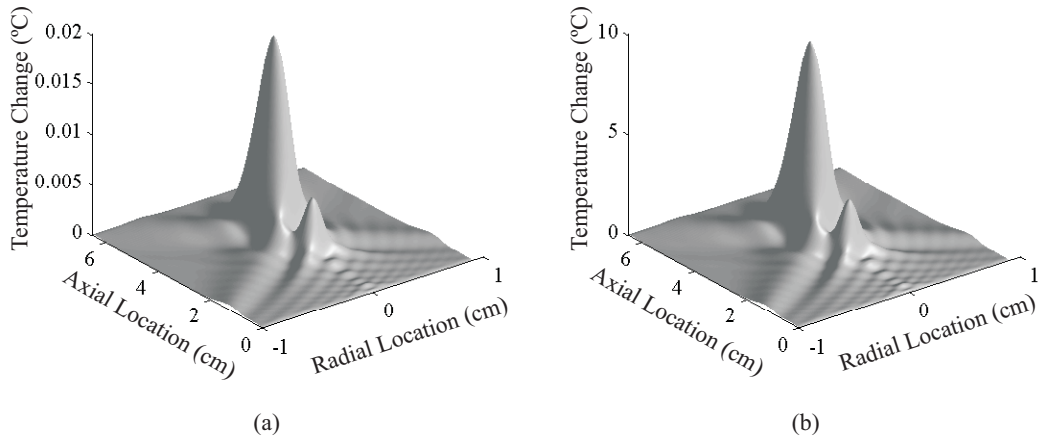

Figure 5.8: Temperature change as a function of axial and radial location for two FDTD solutions to the BHTE: (a) based on a peak positive and negative acoustic pressure amplitude of 0.125 MPa and (b) based on a peak positive and negative acoustic pressure amplitude of 2.84 MPa and 2.64 MPa, respectively, at the focus (the source terms, q_{us}, can be seen in Fig. 5.7).

5.3 Numerical Implementation: Bubble-Related Power Deposition

5.3.1 Bubble Motion

We must now solve the Parlitz equation (Eq. 4.6) for the motion of the bubble wall. The solutions to this equation are calculated using a commercial, Runge-Kutta ordinary differential equation solver (MATLAB Release 11.1, Release 12, The MathWorks, Natick, MA). The solver can provide direct results for the bubble radius and velocity as a function of time. Calculation of the secondary acoustic emission also requires the bubble wall acceleration which can be estimated by differencing the velocity solution.

The fixed parameters in the Parlitz equation are as follows: ρ = 1003 kg/m^3, c = 1588 m/s, p_0 = 1.01 x 10^5 Pa, p_v = 2330 Pa, σ = 0.0725 N/m, and κ = 1.4. We solve for the bubble motion for every combination of bubble sizes, R_0, and tissue phantom viscosity, μ in the ranges of interest. The three fixed limits discussed in the previous chapter were μ_{min} = 0.001 N·s/m^2 (1 cP), $R_{0,min}$ = 0.1 μm, and $R_{0,max}$ = 50 μm. For the tissue phantom recipe "Agar-2", μ_{max} = 0.1 N·s/m^2.

The final parameter of note is the duration of the solution. Given the range of parameters of interest (R_0, μ, p_a), as many as 60,000 or more $r-t$ curves are desirable. This provides the resolution needed in the discretization of the parameter ranges for R_0, μ, and p_a to see trends in the behavior of the bubble responses as a function of these parameters. The computational demands of any one solution of the Parlitz equation are not substantial, but for all of the solutions as whole this may not be true. Solving the Parlitz equation for the full insonation times would be computationally prohibitive for even a fraction of the number of desired solutions. It is also not necessary as the bubble responses reach steady-state in only a fraction of that time. As a result, the minimum number of acoustic cycles required until steady-state is reached was chosen. The bubble motion was found to reach a steady-state response within 5 cycles for our parameter range, and the results in this chapter are based on that solution duration.

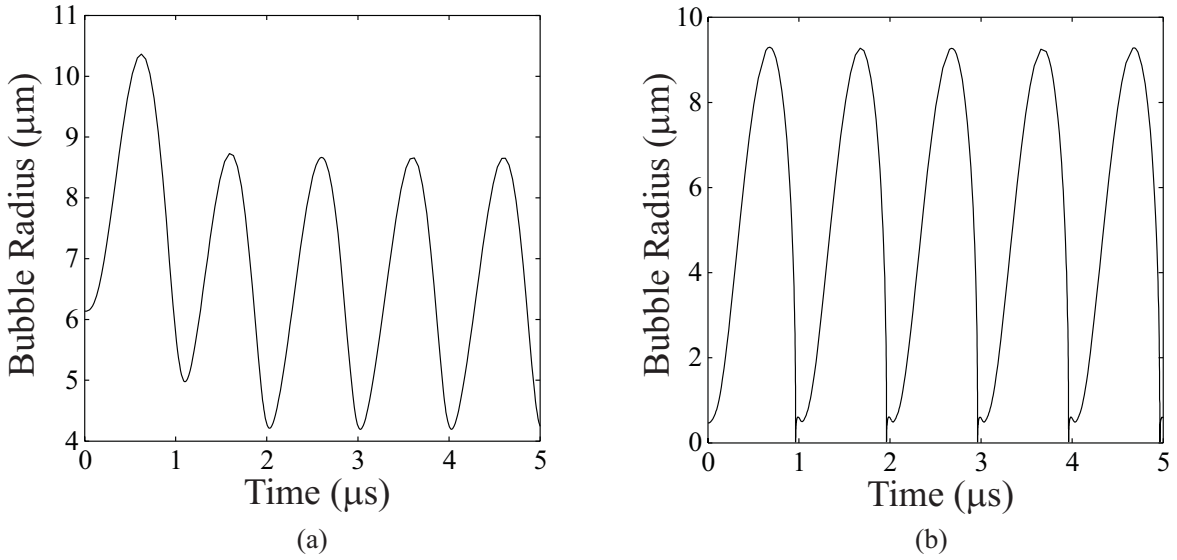

Figure 5.9: Bubble radius as function of time for (a) noninertial bubble motion (μ = 0.1 N·s/m^2, R_0 = 6.1 μm) and (b) inertial bubble motion (μ = 0.004 N·s/m^2, R_0 = 0.46 μm). The acoustic pressure amplitude is 1 MPa.

The large range of values for μ, R_0, and p_a, also means it is not possible to show a "typical" response representative of all or even most solutions. The individual bubble responses are simply too varied. It is possible, however, to show typical examples of non-inertial and inertial cavitation, as classified in the last chapter. Figure 5.9 shows the calculated bubble wall motion for two bubbles sizes, in tissue phantoms with different viscosity values. The acoustic pressure amplitude is 1 MPa. Figure 5.9a is an example of non-inertial cavitation (μ = 0.1 N·s/m^2, R_0 = 6.1 μm). Although it is slightly nonlinear, the oscillations could likely be sustained indefinitely, and the motion is controlled by the stiffness of the gas in the bubble. Figure 5.9b shows an inertial response where, after expansion during the rarefaction phase, the bubble motion is dominated by the inertia of the liquid during collapse (μ = 0.004 N·s/m^2, R_0 = 0.46 μm).

The survivability of bubbles subject to such inertial collapses is debatable. Many believe that the bubble shown in Figure 5.9b will self destruct on collapse, thus the term "transient" cavitation frequently used to describe bubbles undergoing inertial collapse [23]. Conversely, the literature on single bubble sonoluminescence clearly shows that inertially driven bubbles can survive violent collapses cycle after cycle [105]. It is not the intention of this dissertation to resolve this argument. We assume that inertial cavitation bubbles survive intact for the duration of the pulse, or that they are replenished with additional nuclei during insonation such that there is effectively a single bubble's worth of cycles over the course of insonation.

A final note is required regarding the time-averaged values necessary for the viscous dissipation and secondary acoustic emission calculations, represented by Eq. 4.9 and Eq. 4.18. Highly nonlinear inertial cavitation exhibits dramatic changes in bubble wall velocity during the growth and collapse phases. To accurately and efficiently solve for the bubble wall motion, the ordinary differential equation solver uses variable time steps whose values depend on the behavior of the solution. Therefore, time step weighted averages must be used with results such as bubble wall motion or velocity, and quantities derived from these results.

5.3.2 Viscous Dissipation

For convenience, the expression for the power deposition from viscous dissipation is repeated here:

$$D_{vis} = 16\pi\mu \left\langle \dot{R}^2 R \right\rangle_t . \tag{5.15}$$

Given the radius and velocity results from the Parlitz equation, the calculations of D_{vis} is straightforward. Figure 5.10 shows the power deposition per bubble due to viscous dissipation as a function of R_0 and μ for two acoustic pressure amplitudes. The pressure amplitudes are near the upper and lower pressure limits of the enhanced heating region seen in Figure 5.2: plots (a) and (b) are for peak acoustic pressure amplitudes of 2.0 and 2.8 MPa respectively. Note that, to better see the features in the figure, given values of μ and R_0 that span orders of magnitude, both axes are a logarithmic scale. It should also be noted that with viscous dissipation occurring at the bubble interface, the power deposition occurs in a relatively small volume around the bubble.

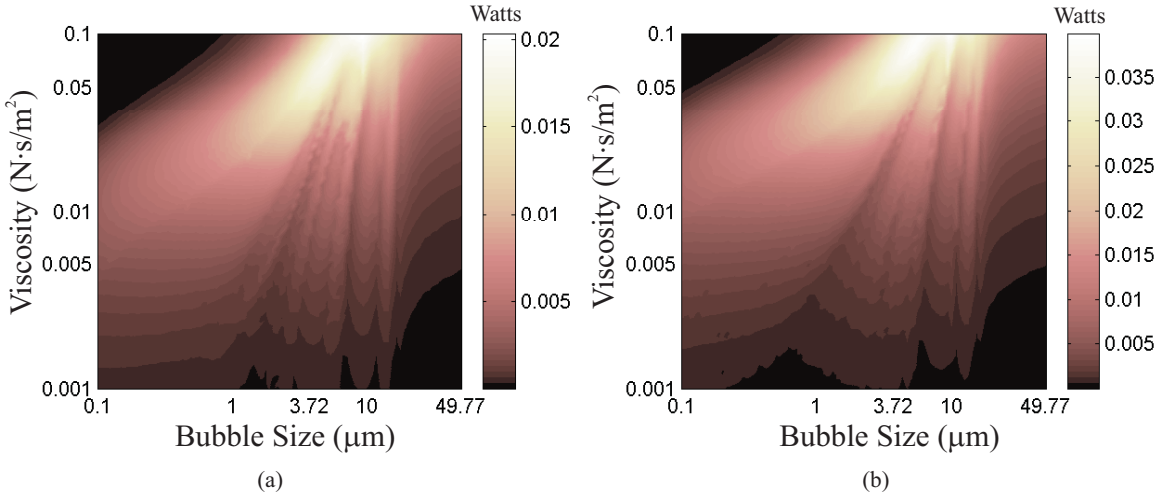

Figure 5.10: Power deposition per bubble due to viscous dissipation as a function of bubble size and tissue phantom viscosity. The acoustic pressure amplitude is (a) 2.0 MPa (b) and 2.8 MPa.

General Observations

High viscosity and large bubbles with respect to the resonance radius generally serve to dampen the bubble motion. This in turn, may reduce the overall bubble wall velocity by reducing overall bubble growth. As a result the components which determine the viscous power deposition in Eq. 5.15, μ, R,

and $\dot{R}$, can work against each other. The peak values in Fig. 5.10 represent a balance between high phantom viscosity while maintaining large time-averaged bubble radii and large time-average bubble wall velocities. The peak power deposition at 2.0 MPa is 0.0204 W (μ = 0.1 N·s/m^2, R_0 = 9.33 μm) and is 0.0398 for 2.8 MPa (μ = 0.1 N·s/m^2, R_0 = 10.0 μm). The peak power deposition per bubble nearly doubles for an increase in acoustic pressure amplitude of 40%.

An additional feature of interest in each plot are the striations seen in the upper and middle left portion of each plot. The striations are indications of the resonance structure often observed in nonlinear bubble dynamics [83]. The result is bubble motion with larger time-averaged radius and velocity values with respect to neighboring bubbles sizes, for a fixed viscosity.

We will now consider the behavior of sub-resonant bubbles (below resonance size). The region in the upper left portion of each plot (above ~0.05 N·s/m^2 and less than ~1.00 μm) where the viscous power deposition is substantially lower is the result of very small bubbles which are heavily damped by large viscosity values. The oscillations are nonlinear but are not inertial, and time-averaged radii and are noticeably smaller than larger bubbles, for a fixed viscosity, or bubbles with less damping (smaller viscosity), for a fixed bubble size. For the remainder of the sub-resonance bubbles, the bubble motion becomes increasingly inertial as the viscosity decreases. This leads to larger time-averaged radii and wall velocities and as a result, the viscous power deposition begins to increase. This decrease in viscosity eventually exceeds the gains due to the increased bubble motion, and the viscous power deposition begins to decrease again.

5.3.3 Secondary Acoustic Emission

Unlike viscous dissipation, only a portion of the power deposition from secondary acoustic emission, will be absorbed in a small volume around the bubble. For many bubble sizes and viscosity values considered only a small fraction of the radiated sound will be absorbed in the entire focal region, while for others this fraction will be quite large. This dependence of the absorbed sound on the bubble motion in the region of interest (in our case, this means the region that influences the location of the thermocouple) means that the power deposition will be a function of the bubble response. For

this reason we will need to specify the nature of the bubble response under consideration prior to incorporating the power deposition in the BHTE.

Total Radiated Power

To determine the fraction of the radiated sound that is absorbed as a function of distance from the bubble, we must first know the total power radiated, D_{sac}^{max}. This would be the total power absorbed if we considered an *infinite* propagation distance for this radiated sound. Figure 5.11 shows D_{sac}^{max} for acoustic pressure amplitudes of 2.0 MPa (a) and 2.8 MPa (b), the same values used for the viscous power deposition in Fig. 5.10.

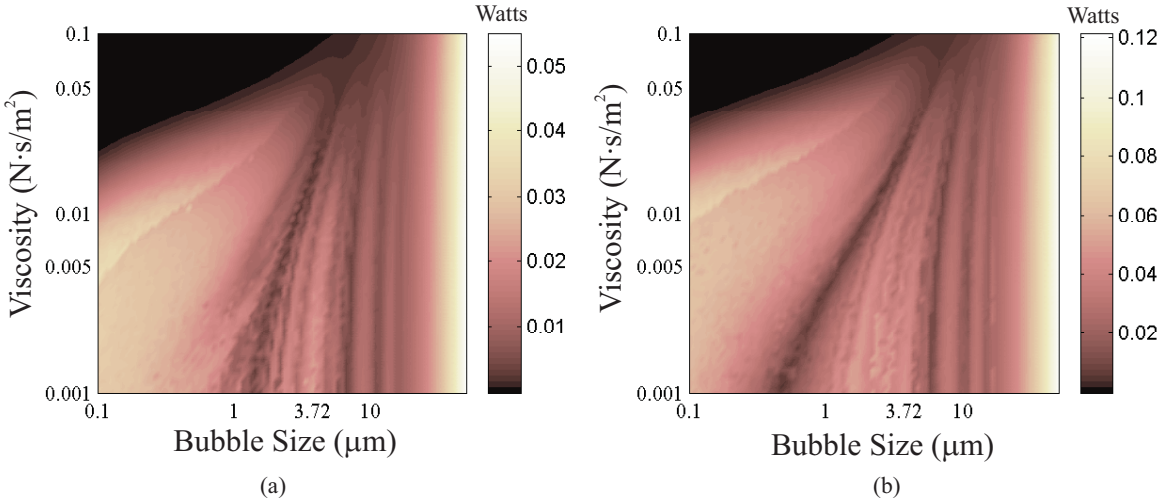

Figure 5.11: Total radiated power per bubble due to secondary acoustic emission as a function of bubble size and tissue phantom viscosity. The acoustic pressure amplitudes are (a) 2.0 MPa and (b) 2.8 MPa.

The regions of maximum radiated power in Fig. 5.10 can be divided into three sections. The increase in the far right off each plot, for ~25 μm and higher, is the result of very large bubbles with moderate acceleration (with respect to smaller bubbles). The radiated sound is the result of a large, pulsating sphere, an example of which is shown in Fig. 5.12a. This plot represents the radiated pressure 1 mm from a 30.5 μm bubble, with a phantom viscosity of 0.01 N·s/m^2 for a peak acoustic driving pressure of 2.8 MPa. The plot is of the unattenuated pressure.

The remaining two regions are the result of a different type of bubble motion, and subsequently emit a different type of radiated pressure. The region of radiated power above ~0.02 W in Fig. 5.11a

and above ~0.05 W in Fig. 5.11b and comprising much of the lower left portion of each plot, represents sub-resonant, inertial bubbles. The peak radiated pressure from these bubbles is the result of the violent collapse, and far exceeds the magnitude of the radiated pressure at any other point during an acoustic cycle. This effect can be seen clearly in Fig. 5.12b where the sharp spikes indicate the violent collapses such as those seen in Fig. 5.9b. This plot represents the radiated pressure 1 mm from a 0.46 μm bubble, with a phantom viscosity of 0.004 N·s/m^2, also for a peak acoustic driving pressure of 2.8 MPa.The final region is indicated by the striations in Fig. 5.11, generally between ~2 and ~15 μm. These striations are again indicative of the nonlinear response of super-resonant bubbles whose period of oscillation is a function of the insonation frequency. As a result, there are violent collapses similar to the sub-resonant bubbles, however, unlike most sub-resonant inertial bubbles the collapses do not occur every period with respect to the driving frequency.

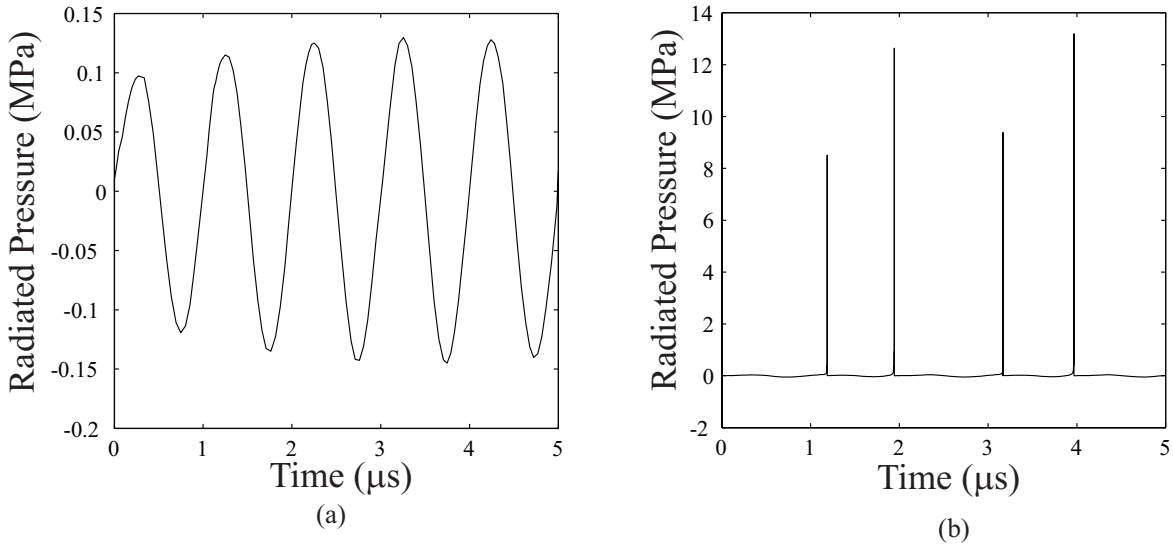

Figure 5.12: The radiated acoustic pressure 1 mm from the bubble wall in the absence of attenuation for (a) a noninertial (μ = 0.01 N·s/m^2, R_0 =30.5 μm) and (b) an inertial (μ = 0.004 N·s/m^2, R_0 = 0.46 μm) bubble. The acoustic driving amplitude is 2.8 MPa.

Relevant Power Deposited

Radiated acoustic sound is not a guarantor of *absorbed* power in a finite volume, in particular the finite volume relevant to the experimental temperature measurements we will ultimately attempt to simulate. We are primarily concerned with the peak temperature rise at a thermocouple located

0.5 mm off-axis, in the focal plane. As a result, radiated power that is absorbed at a distance from the thermocouple that does not affect the peak temperature at the thermocouple is not of importance for these simulations.

The primary factors affecting the fraction of the radiated sound that is absorbed are the frequency dependence of the attenuation of the phantom material and the nature of the radiated sound. The dramatic difference between the radiated pressure seen in Fig. 5.12 is the result of the presence of higher frequencies, or the broadband nature of the sound, a direct consequence of the bubble dynamics. The increased phantom attenuation as a function of increasing frequency results in greater power deposition for the radiated sound seen in Fig. 5.12b than for Fig. 5.12a, for a fixed volume.

The power deposition as a function of distance from the bubble, $D_{sac}(r)$, was defined in Eq. 4.18. As described in the previous chapter, it is the result of subtracting the attenuated power, as a function of distance from the bubble, from the total radiated power. The attenuated power, P_{sac}, is determined by calculating the frequency spectrum of the radiated pressure, applying the frequency dependent attenuation to this spectrum, and converting the attenuated pressure back to the time domain. The numerical conversion to and from the frequency domain is performed here using a commercial discrete and inverse discrete Fourier transform package (MATLAB Release 11.1, Release 12, The MathWorks, Natick, MA).

Figure 5.13 shows the fraction of the total radiated power that is absorbed as a function of distance from the bubble. At some distance that is a function of the frequency content of the radiated sound and the phantom attenuation, this value will approach unity. The results are for the same bubble responses used to calculate the radiated pressure in Fig. 5.12. Figure 5.13a is for a 30.5 μm bubble, with a phantom viscosity of 0.01 N·s/m^2 and a peak acoustic driving pressure of 2.8 MPa. Figure 5.13b is for a 0.46 μm bubble, with a phantom viscosity of 0.004 N·s/m^2 and a peak acoustic driving pressure of 2.8 MPa.

Although the total radiated power, as indicated in Fig. 5.11, for these two bubble responses is of the same order of magnitude, there is a clear difference in the fraction of that power that is absorbed in a region relevant to the focal region and the thermocouple. A relatively insignificant

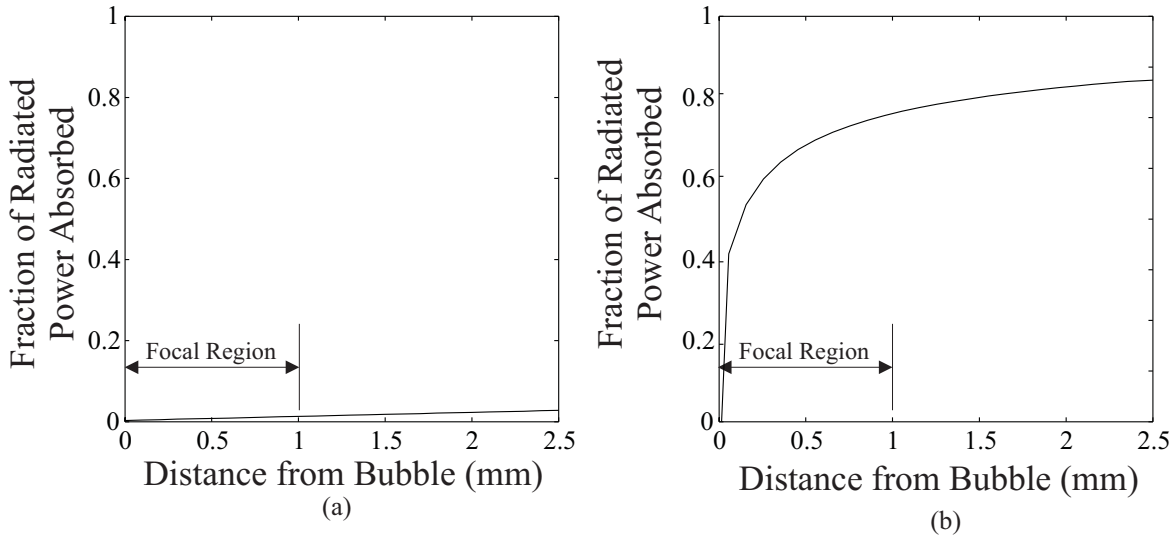

Figure 5.13: The fraction of the radiated power that is absorbed as a function of distance from the bubble for (a) a noninertial (μ = 0.01 N·s/m^2, R_0 =30.5 μm) and (b) an inertial (μ = 0.004 N·s/m^2, R_0 = 0.46 μm) bubble. The acoustic driving amplitude is 2.8 MPa.

portion (~1%) of the radiated power from the 30.5 μm bubble is actually absorbed and contributes to power deposition within the focal region. In contrast, between 75% and 80% of the radiated power is absorbed in the focal region for the 0.46 μm bubble.

5.3.4 General Observations

Before these calculations of bubble-related power deposition are put to use, an important feature can be observed by viewing the results of viscous dissipation and secondary acoustic emission side-by-side. Figure 5.14 shows the power deposition from each mechanism for an acoustic pressure amplitude of 2.8 MPa.

Figure 5.14a is the same viscous dissipation results shown in Fig. 5.10b. Figure 5.14b is the fraction of the total power deposition due to secondary acoustic emission seen in Fig. 5.11, which occurs in the focal region, taking into account the frequency dependent absorption. What is arguably most striking is the distinct difference between which combinations of R_0 and μ are important to each mechanism. Although there is some overlap in which bubble sizes and viscosity values do *not* lead to significant power deposition, and there is some small overlap in some areas of moderate power deposition, there is no similarity in the regions of peak power deposition for each result. This is the

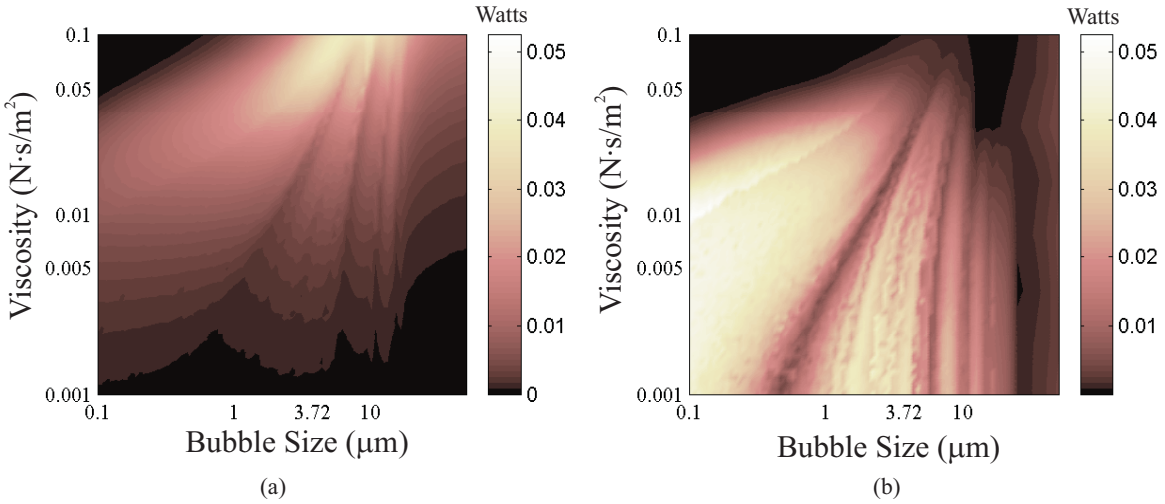

Figure 5.14: The magnitude of the power deposition per bubble due to (a) viscous dissipation and (b) secondary acoustic emission in the focal region as a function of bubble size and tissue phantom viscosity . The acoustic pressure amplitude 2.8 MPa

result of the secondary acoustic emission being primarily due to a function of the inertial cavitation activity while viscous dissipation results primarily from the noninertial cavitation activity. As a result, if other analysis or detection mechanisms, such as the PCD system used in the experiments, are sensitive to a particular range of R_0 and μ (or conversely a particular type of cavitation) it may provide additional evidence as to which mechanism is most important.

5.3.5 Numerical Implementation: Determining the Number of Bubbles Required for Enhanced Heating

In the absence of specific knowledge regarding the locations of individual bubbles, we will use a power density, q_b, that is a function of space and which is intended to be representative of the aggregate contributions of any bubbles in the volume where cavitation is assumed to occur. The total magnitude of this spatial distribution of the power density will then be varied until simulated peak temperatures match the experimental results. This approximation for the bubble-related power density term, q_b, requires 3 assumptions:

(1) We assume that there are sufficient bubbles such that this aggregate representation of the power density is accurate. As the number of bubbles approaches zero, the power density becomes increasingly discrete, and distributing the power over the entire volume containing any bubbles becomes less accurate.

(2) By using cylindrical symmetry, and including a non-zero bubble-related power density off-axis, we assume that the off-axis bubbles are evenly distributed around the volume and do not favor a particular θ location. This is likely true given the cylindrical symmetry in the acoustic pressure field.

(3) By defining the spatial distribution of the power density, independent of the magnitude, and then varying that magnitude to match the temperature, we assume that for a fixed insonation pressure, the relative spatial distribution of bubbles is independent of the total number of bubbles.

The quantity we must define can be thought of as the bubble-related "power density (spatial) distribution". It represents the relative magnitude of the power density as a function of space, independent of the total power density. An example of a power density distribution that is *not* bubble-related is that from primary absorption. Figure 5.15 shows the normalized power density from primary absorption as a function of axial and radial distance. As demonstrated in Fig. 5.7, the actual power density, q_{us}, is simply a scaled version of Fig. 5.15 based on the peak intensity of the acoustic field. The objective of this section is to develop a bubble-related power density distribution similar to this example (similar in functionality not necessarily in shape) for primary absorption.

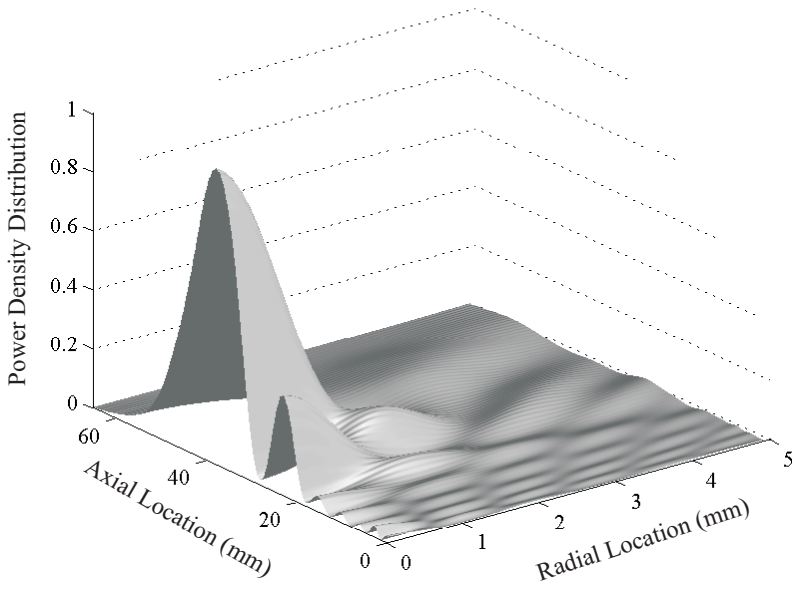

Figure 5.15: Relative power density as a function of axial and radial location for primary absorption.

The experimental data we will use for comparison are the measurements for the 2 second insonation in the insonation duration experimental section (Sec. 3.6). The insonation duration experiments have the largest number of repeated measurements at a given acoustic pressure amplitude

and insonation duration. This will provide the best available estimate of the average of the temperature rise due to enhanced heating as a function of acoustic pressure. Two seconds is chosen for it lies near the middle range of insonation times investigated.

The bubble-related power deposition is a function of acoustic pressure. As a result, the power *density*, q_b, we apply to the BHTE equation will be a function of the pressure in the phantom. However, the relationship between bubble-related power deposition and acoustic pressure is not necessarily the same for all combinations of R_0 and μ. The power deposition of sub-groups of bubbles within the parameter ranges may scale similarly with acoustic pressure, but as seen in Fig 5.9, the bubble response over the entire range can be very different, and the power deposition as function of acoustic pressure may be very different as well.

To accommodate these differences we will consider specific cases of distinct bubble responses. The two cases we will consider are the "optimal" noninertial bubble response and the "optimal" inertial bubble response. By optimal we mean the bubble size and phantom viscosity combination whose bubble response produces the maximum power deposition. For noninertial bubble responses, this means those bubbles with the maximum viscous power deposition, as indicated by results such as those in Fig. 5.10. The specific bubble size and phantom viscosity is not crucial as there is a range of bubble sizes and viscosity values which have very similar responses and subsequently very similar values for viscous power deposition. For this analysis we will choose μ = 0.1 N·s/m^2, R_0 = 10.0 μm. Optimal bubble responses for inertial bubbles are those with the maximum secondary acoustic power deposition. These are represented by bubbles below approximately 1 μm and phantom viscosity values below 0.02 N·s/m^2. Again, the particular response is not crucial, and we will use μ = 0.01 N·s/m^2, $R_0 = 0.5\mu$m.

Implications of Cavitation Pressure Thresholds

The first step in applying a bubble-related power density distribution is to determine where the bubbles are likely to exist. We begin with the assumption that there are no bubbles present in the phantom. From the PCD data for an insonation duration of 2 seconds (Fig. 3.21), we can limit

the location of the bubbles to the region of the solution domain where the peak negative acoustic pressure is at or above the threshold pressure of 1.6 MPa. Figure 5.16a is a plot of the peak negative acoustic pressure as a function of radial and axial location. These results are calculated from the FDTD solutions for the pressure, matching the experimental conditions and material properties of the insonation duration experiments. The peak negative acoustic pressure amplitude at the focus is 2.76 MPa.

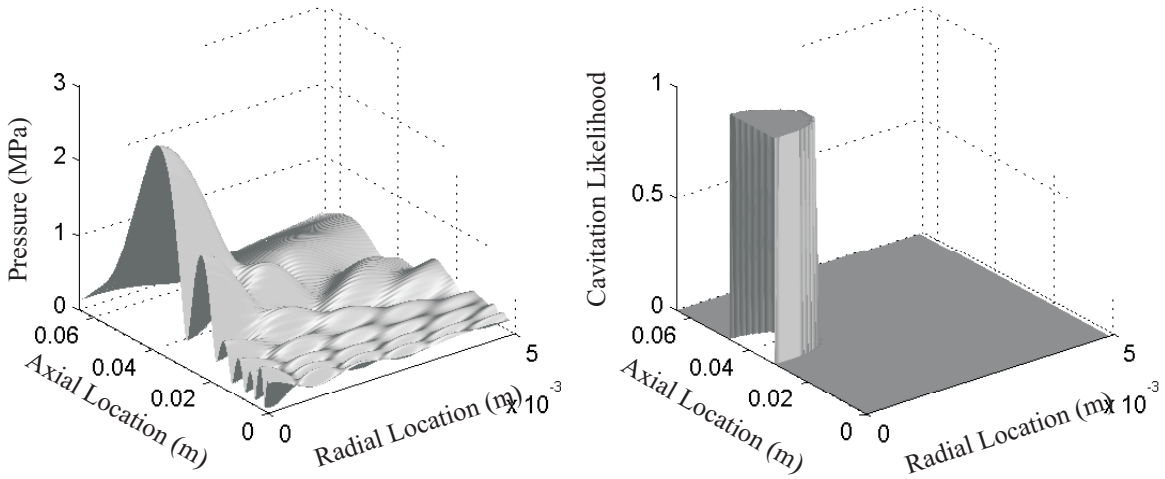

(a) (b)

Figure 5.16: (a) Peak negative acoustic pressure as a function of axial and radial location determined from the FDTD pressure solution. The peak negative acoustic pressure is 2.76 MPa. (b) Cavitation likelihood spatial distribution based on the experimental threshold pressure for cavitation activity for a peak negative acoustic pressure of 2.76 MPa. A value of 1 indicates locations where bubbles are assumed to exist.

Figure 5.16b is the resulting cavitation likelihood as a function of radial and axial location based solely on the criteria of the 1.6 MPa threshold pressure for cavitation activity at an insonation duration of 2 seconds. To stop the analysis here and use this distribution would be to assume that at any and every location where the peak negative acoustic pressure exceeds 1.6 MPa the contribution from bubble-related power deposition is equal, and at every other location it is zero.

We can develop a better power density distribution by taking into consideration the likelihood for cavitation activity. Figure 3.21 shows the likelihood of cavitation activity as a function of acoustic pressure amplitude. By interpolating (linearly) between measured values, we can scale the power density distribution to reflect the fact that we are likely to find more bubbles at higher acoustic

pressures in the field, than for lower pressures. Figure 5.17 shows the cavitation likelihood from Fig. 5.16b scaled to reflect the decreasing likelihood as a function of acoustic pressure.

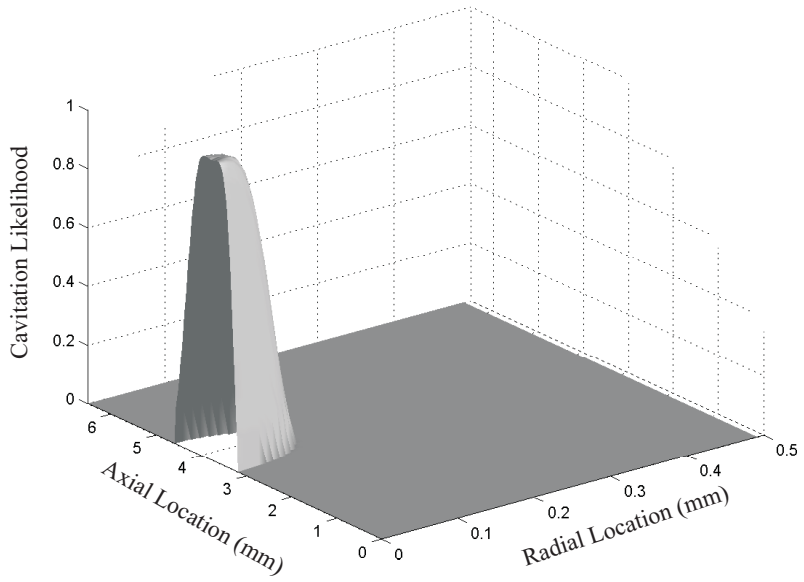

Figure 5.17: A cavitation likelihood spatial distribution based on the experimental threshold pressure for cavitation activity and the pressure dependent likelihood for cavitation activity based on experimental results obtained for a 2 second insonation duration and a peak acoustic pressure of 2.76 MPa.

Consideration of cavitation thresholds is only the first step. It is now necessary to determine the influence of acoustic pressure on the power density distribution. This will be evaluated individually for the two cases we are considering: optimal noninertial and inertial bubbles.

Noninertial Power Density Distribution

In this section we are concerned with the effect of acoustic pressure on the power density for noninertial bubbles with high viscous power deposition. We will neglect the secondary acoustic contribution for this bubble size and phantom viscosity whose power deposition is dominated by viscous dissipation. Figure 5.18a shows the viscous power deposition as a function of acoustic pressure for a bubble size of 10.0 μm and μ = 0.1 N·s/m^2. A curve fit is also shown which is represented by $D_{vis} = 0.0047 p_a^{2.01}$. Figure 5.18b shows the resulting normalized power density as a function of axial and radial location based on this relationship between viscous power deposition and acoustic pressure.

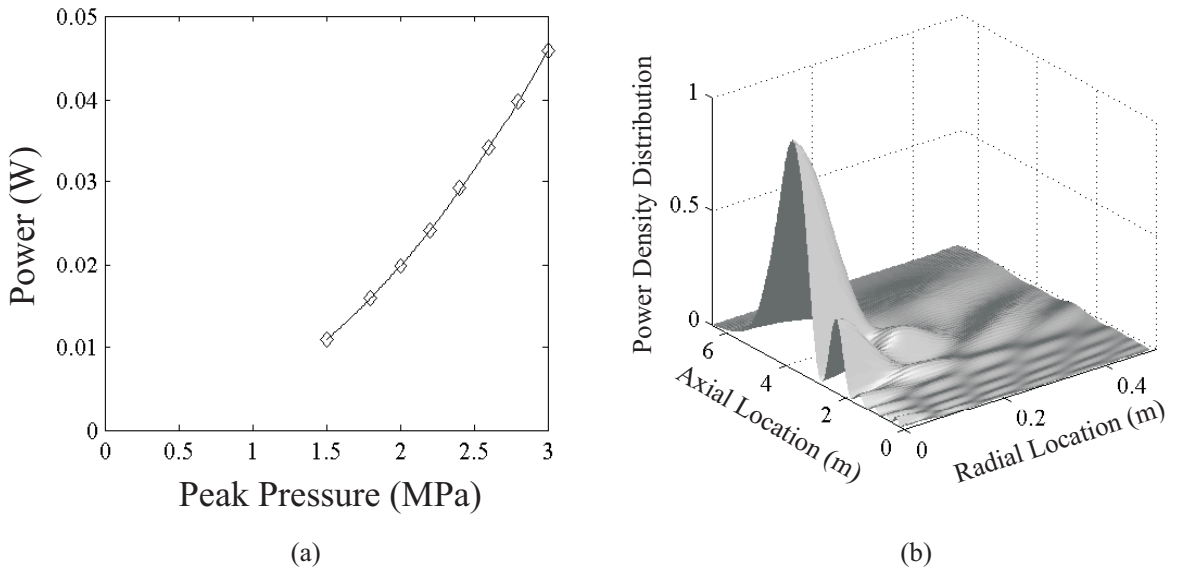

Figure 5.18: (a) Viscous power as a function of peak acoustic pressure for a bubble size of 10.0 μm and μ = 0.1 N·s/m^2. (b) Normalized power density as a function of axial and radial location for a peak negative acoustic pressure of 2.76 MPa based on the relationship between acoustic pressure and viscous power deposition in plot (a).

Inertial Power Density Distribution

The implementation of the power density for inertial bubbles will be very similar to that of the noninertial bubbles, however there are two additional issues which must be addressed. These issues relate to the fact that the absorption of radiated sound is not inherently localized to a small volume around the bubble, as is the case with viscous dissipation. The first question is whether the acoustic pressure amplitude substantially affects the absorbed sound as a function of distance from the bubble. Figure 5.19 shows the fraction of the total radiated power absorbed as a function of distance from the bubble for acoustic pressure amplitudes of 2.0 and 2.8 MPa, the general range of interest for our enhanced heating measurements. The bubble size is 0.5μm and μ = 0.05 N·s/m^2. What is important is that these values are very similar, despite the difference in the acoustic pressure. Although the magnitude of the power deposition will be different, we do not need to be concerned with the fraction of that power as a function of distance also being a function of the acoustic pressure for this range of pressure. As a result, when considering the absorbed power as a function of distance we will simply use the values from 2.0 MPa for all acoustic pressure amplitudes.

The second question involves how important the distance from the bubble is with respect to

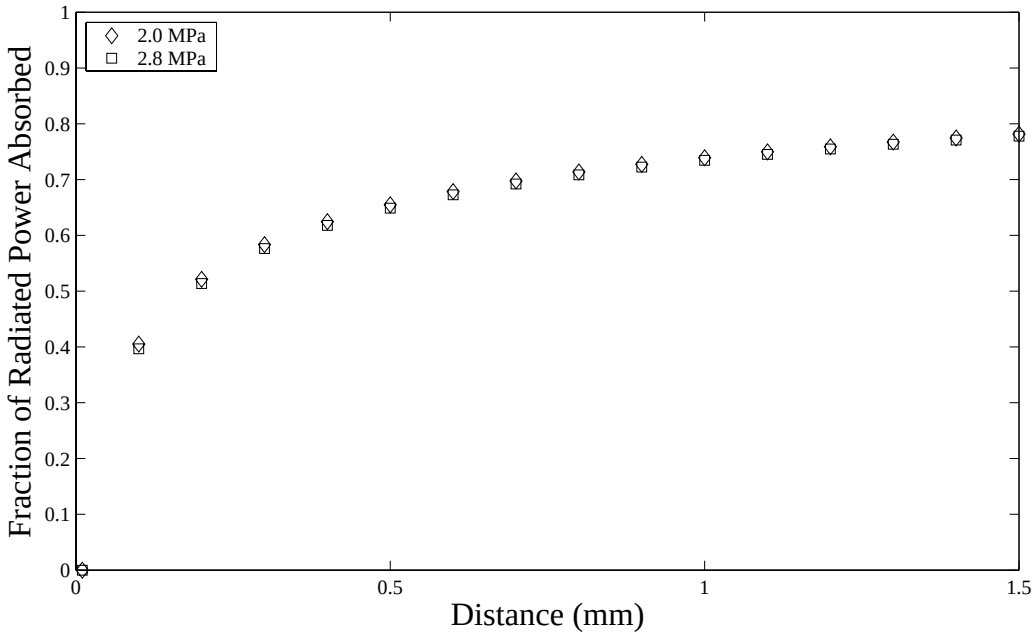

Figure 5.19: The fraction of the total radiated power absorbed as a function of distance from the bubble for two pressure amplitude.

the power deposition for the inertial bubbles under consideration here. It can be seen in Fig. 5.19 that approximately 75% of the radiated power is absorbed within 1 mm of the bubble. With the thermocouple located 0.5 mm off-axis, bubble-related power deposited outside the focal region is less important as it will not affect the thermocouple at the time of peak temperature change. The question then becomes how to implement the deposition of the 75% of that radiated power that is absorbed essentially in the focal region.

The approximation we will make is to apply the power absorbed in the focal region in the same manner as the viscous dissipation. That is, to attribute all of the power to one grid point or location when determining the aggregate behavior. Any other option to accurately apply the power deposition as a function of distance from a bubble requires specific assumptions regarding the bubble locations. To support this assumption we can again look at Fig. 5.19, this time as an indicator of the relative power deposited at each grid point in the FDTD solution for a grid spacing of 0.1 mm. The change for each subsequent value as the distance increases represent the relative amount of power deposited in the volume around that grid location. These results indicate that the largest power deposition occurs near the bubble, with largest deposition occurring at the grid location specifying the bubble

location, and substantially smaller amounts deposited thereafter. The assumption we are using here serves to attribute all of that power deposition, up to 1 mm, to the one location where the bubble is presumed to exist.

Figure 5.20a shows the secondary acoustic power deposition per bubble as a function of acoustic pressure amplitude. The secondary acoustic power deposition in this figure is defined as the 75% of the radiated sound absorbed within 1 mm of the bubble. The curve fit indicates the relationship is $D_{sac} = 0.0053 p_a^{2.25}$, which is very similar to the primary absorption and viscous power deposition. The larger exponent does serve to concentrate the power density closer to the focus as compared to primary absorption or viscous dissipation, however. Figure 5.20b is the resulting normalized power density distribution based on this relationship between secondary acoustic emission and pressure, for an acoustic pressure of 2.76 MPa. This figure is the inertial equivalent of Fig. 5.18.

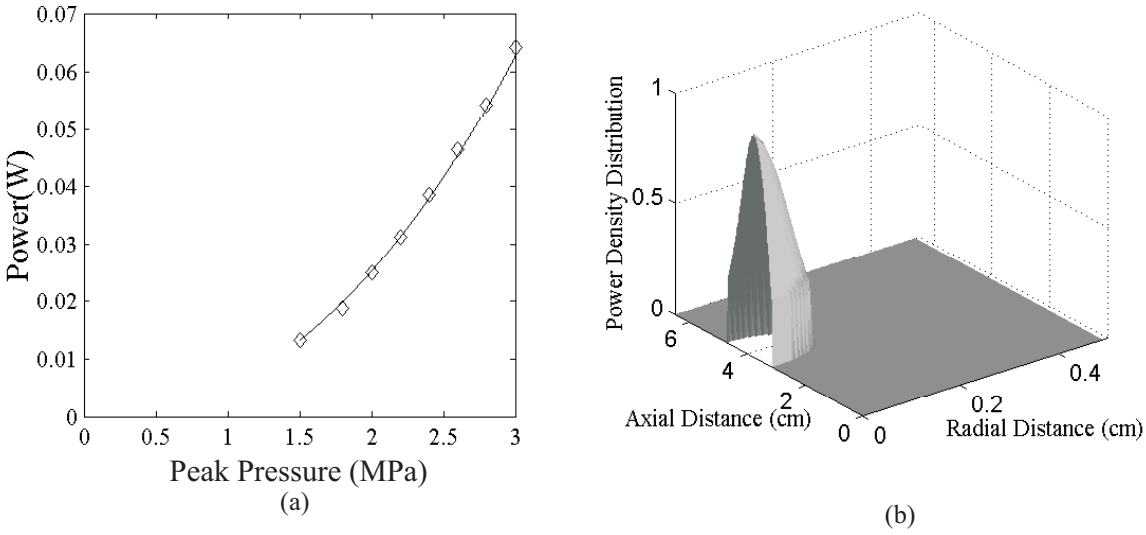

Figure 5.20: (a) Secondary acoustic power as a function of peak acoustic pressure for a bubble size of 0.5 μm and μ = 0.01 N·m. (b) Normalized power density as a function of axial and radial location for a peak negative acoustic pressure of 2.76 MPa based on the relationship between acoustic pressure and inertial power deposition in plot (a).

5.4 Results and Discussion

Estimating the actual number of bubbles required for a particular experimental temperature measurement is an iterative process. For a given insonation duration and pressure we must:

(1) Make an initial guess as to the number of bubbles required.

(2) Determine the spatial distribution of these bubbles based on the cavitation likelihood seen in Fig. 5.17.

(3) Given the bubble locations from the previous step, determine the power density contribution of each bubble, as a function of location, based on the results shown in either Fig. 5.18 and Fig. 5.20 for a noninertial or inertial bubble, respectively.

(4) Solve for the temperature rise at the thermocouple location using the BHTE and the additional power density as a function of space determined in the previous step.

(5) Compare the calculated temperature to the measured temperature. Adjust the initial guess for the number of bubbles up or down as appropriate and repeat the process until these two values are equal.

Figure 5.21 shows the results of incorporating bubble-related power deposition in the BHTE where the above process has been followed for a range of super-threshold pressures at an insonation duration of 2 seconds. The plot shows the peak temperature change for experimental and numerical results as a function of peak negative acoustic pressure at the focus. The diamonds represent the experimental results for only those measurements with enhanced heating, taken directly from Sec. 3.6. The solid line represents results from the BHTE in the absence of bubble-related power density terms. Finally, the squares represent the predicted temperatures that are the result of including a bubble-related power density in the BHTE.

Table 5.2 lists the results for the case of optimal noninertial bubbles. The table shows the measured temperature rise, as seen in Fig. 5.21 (diamonds) and the corresponding number of bubbles found to meet that temperature change, all as a function of the peak negative acoustic pressure. In particular, the number of bubbles represents the number of 10.0 μm bubbles, for a phantom viscosity of 0.1 N·m, whose individual power deposition add up to the total power deposited (this specifically assumes the contributions of individual bubbles can be added linearly). The total power deposited is simply the power density, q_b multiplied by the volume in which q_b is applied. Table 5.3 lists the results for the inertial case. In this case, the number of bubbles represents the number of 0.5 μm bubbles, for a phantom viscosity of 0.01 N·m, that are required.

These results, both independent of and in conjunction with the experimental data, provide important information regarding bubble enhanced heating. The results in Fig. 5.14 would appear to

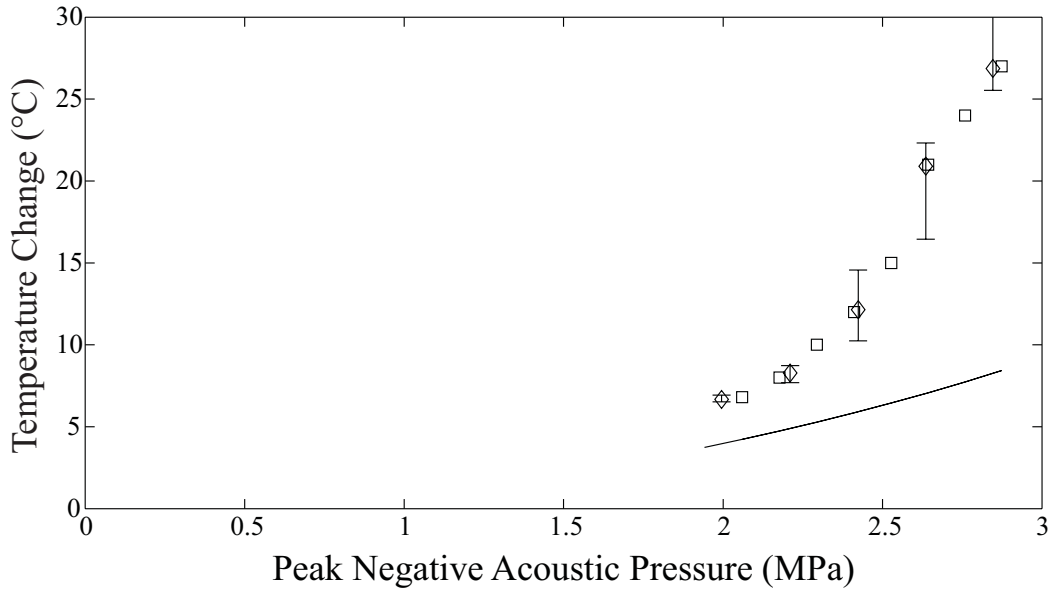

Figure 5.21: Experimental results and numerical simulations which indicate the desired result of including bubble-related power deposition in the BHTE. Experimental measurements of temperature (diamonds) are compared with numerical simulations in the absence of (solid line) and presence of (squares) bubble-related power deposition for an insonation duration of 2 seconds.

Pressure (MPa)	Δ T	No. Bubbles Required
2.06	6.8	10
2.18	8.0	12
2.30	10	16
2.41	12	17
2.53	15	22
2.64	21	27
2.76	24	35

Table 5.2: Required peak power density, q_b^{max} and the corresponding number of bubbles required to account for the enhanced temperature rise ΔT, all as a function of acoustic pressure. These results are for the noninertial case.

Pressure (MPa)	Δ T	No. Bubbles Required
2.06	6.8	10
2.18	8.0	12
2.30	10	15
2.41	12	16
2.53	15	22
2.64	21	28
2.76	24	35

Table 5.3: Required power density, q_b^{max} and the corresponding number of bubbles required to account for the enhanced temperature rise ΔT, all as a function of acoustic pressure. These results are for the inertial case.

indicate that either heating mechanism has the potential to deposit enough power to account for the enhanced heating effect seen in experiments. This is supported by the tabulated data which suggests there is near parity between *optimal* noninertial and inertial bubbles required to account for the enhanced heating, suggesting the potential for either mechanism to be the cause of the enhanced heating effect (It should be noted that the fact that there is such parity at 2 seconds is primarily a coincidence of the thermocouple location. Other combinations of insonation duration and thermocouple location will not exactly equal.)

However, other factors suggest strongly the role of secondary acoustic emission. A scenario that suggests a dominant role for viscous dissipation as the primary mechanism for enhanced heating would require very high viscosity and large bubbles. Indeed, the viscosity must remain at or very near our upper limit, which, as described in the previous chapter, was a limiting value which assumed that *all* measured attenuation was due to absorption, with no scattering component. In addition, the number of bubbles listed in Table 5.2 and Table 5.3 are for "optimal" bubbles. In reality, there is likely to be range of bubble sizes present. In considering Fig 5.14, the range of sub-resonant and even super-resonant inertial bubbles which deposit power at or near the peak value used in the analysis far exceeds the range of bubble sizes which have can deposit power at the level of the noninertial, optimal bubble. As a result, an argument for noninertial bubbles with high viscous power deposition being responsible for the enhanced heating effect requires that either a high percentage of the bubbles present fall into this smaller parameter range, or there must be a greater number of total bubbles, as compared to the inertial case, such that a sufficient fraction are at or near the optimal range.

In addition, the sensitivity of the PCD system to high frequency sound radiation, and subsequently, inertial cavitation, when viewed in light of the strong correlation between the enhanced heating effect, suggests secondary acoustic emission is the primary mechanism at work. Moreover, it is not likely that bubbles larger than resonance size can survive the nucleation and subsequent growth process via rectified diffusion. Newly formed bubbles are likely to be sub-resonant, particularly near threshold [63]. The only way for those bubbles to reach super-resonant size is via rectified

gas diffusion. As the bubbles approach resonance size, however, they tend to break up due to shape instabilities [105]. The details of this process are not well understood, particularly for a non-Newtonian material. Nevertheless, there is reason to believe that a progression from sub-resonant to super-resonant size at these pressure amplitudes is unlikely. This fact, coupled with the fact that the inertial bubbles are generally more efficient power depositors and the fact that the PCD shows good correlation with pressure-dependent temperature rise measurements, suggest a primary role for sub-resonant inertial cavitation. This is a key observation and one that should be considered in all future modeling efforts.

Chapter 6

Summary and Conclusions

6.1 Recapitulation of Results

The primary findings of the experimental results and numerical simulations are identified in the following list, accompanied by the relevant section. A more detailed discussion of these results follows.

(1) The insonation of a tissue-mimicking phantom with focused, MHz-frequency ultrasound resulted in elevated temperatures in the region of the focus (Sec. 3.4).

(2) For insonation pressure amplitudes below a threshold level, the measured temperature rise is well described by classical viscous absorption. The model employs a nonlinear wave equation for the acoustic field coupled with a transport equation for the temperature field (Sec. 3.4, 5.1.1).

(3) For insonation pressures above the threshold level, measured heating rates greatly exceed those predicted by the aforementioned model. The phenomenon is referred to as "enhanced heating" (Sec. 3.4).

(4) A strong correlation is observed between the enhanced heating effect and observable cavitation activity monitored using a passive cavitation detector (PCD) (Sec. 3.5).

(5) The duration of insonation does not have a substantial impact on the enhanced heating effect or on the level of observed cavitation activity for insonation times of 0.5 seconds and longer (Sec. 3.6).

(6) The influence of cavitation is described by a model that employs contributions from large, stable cavitation bubbles (viscous heating of the fluid flow at the bubble surface) and/or small inertial cavitation bubbles (heating from the absorption of acoustic radiation) (Sec. 5.3).

(7) The bubble-related power deposition from both viscous dissipation and secondary acoustic emission can be of the same order of magnitude; albeit for markedly different bubble sizes and phantom viscosity (Sec. 5.3).

(8) Model agreement with the measured super-threshold temperature levels is achieved through the incorporation of less than 100 “optimally sized” bubbles, where the optimum size differs for the two candidate heating mechanisms (Sec. 5.4).

The correlation between the enhanced heating effect and observable cavitation activity has been extended beyond the fact that both may occur at the same pressure amplitude during insonation. A strong correlation was also observed in the onset (in time) for each effect during insonation. This is an important result in that it negates the possibility that the cavitation activity is somehow induced by the higher temperatures of the enhanced heating effect itself. At a minimum it could be concluded that enhanced heating and cavitation activity are both the result of the same physical effect, causing them to occur at the same time. However our additional knowledge of the power deposition and subsequent heating capabilities of cavitation activity suggests strongly the roles of cavitation activity as the cause and enhanced heating as the effect.

The third facet of the correlation between enhanced heating and observed cavitation activity involves the relative changes in the magnitude of each effect as a function of acoustic pressure amplitude. From inception through apparent saturation both phenomena track each other closely, and do so repeatedly. Specifically, the mean correlation coefficient was found to be 0.95 for 48 measurements, strongly suggesting a strong link between the two phenomena.

Any such correlation is important from the perspective of both fundamental research and practical application. A correlation between the enhanced heating effect and observable cavitation activity indicates that the relationship is not simply between an enhanced heating effect and generic cavitation activity, but is specifically tied to those acoustically-active bubbles to which the PCD is most sensitive. The PCD system incorporated in our experimental apparatus is maximally sensitive to acoustic radiation above the insonation frequency. This is a consequence of our choice of sensing transducer bandwidth (15 MHz center frequency) and the high-pass filtering of the signal (2 MHz cutoff, 24dB/octave attenuation). As such it is not necessarily even particularly sensitive to the first or second harmonic of the insonation frequency, but rather to even higher harmonics and to broadband sound well above 1 MHz.

As a result, the sensitivity of the PCD system is biased toward highly nonlinear oscillations associated with some forms of noninertial cavitation, and the violent collapses (and subsequent broadband acoustic emissions) of inertial cavitation. Understanding the nature of the cavitation activity at work is important to the fundamental understanding of the enhanced heating effect as it allows us to associate the nature of said cavitation activity with specific bubble-related power deposition mechanisms, ultimately leading to a better understanding of the physical process. In the case of inertial cavitation, it allows us to make a strong argument for the role of secondary acoustic emission as a means for enhancing hyperthermia. From a practical perspective, understanding the nature of the cavitation activity permits us to tailor the cavitation field to optimally achieve enhanced heating with minimal collateral bioeffect. For example, conditions which are known to induce or magnify inertial cavitation activity can be utilized. Inertial cavitation is optimally promoted by nuclei consisting of sub-resonant bubbles and pressure amplitudes in excess of the cavitation threshold – irrespective of the pulse duration. This could be achieved clinically by employing commercial echo contrast agents and pulsed ultrasound at super-threshold pressures and relatively short pulse durations (to minimize mechanical damage).

Perhaps most importantly, the strong correlation between heating and inertial cavitation means that the PCD system may be used as a means of non-invasively monitoring the enhanced heating effect in real time. Feedback could even be used to maximize the PCD output or to achieve a sustained level of cavitation with minimal acoustic exposure levels. (The observed saturation in the temperature versus time curves argues for the adoption of this sort of monitoring or feedback control.) These advantages will be revisited when the simulation results, in conjunction with these experimental results, are discussed in the conclusions.

The (non)effect of insonation duration on the onset and magnitude of enhanced heating is important primarily on account of the effect of primary absorption. Primary absorption is only localized in so much as the acoustic source is focused. Regardless and in spite of any focus, there is still direct heating outside the focal region; it is simply at a lower level in most cases. Any region of increased pressure outside of the focus will lead to increased primary absorption, and therefore an

increased temperature rise. This fact must be kept in mind when considering therapeutic applications. There may come a point where increasing the pressure or the insonation duration to achieve the desired temperature change at the focus requires an unwanted level of heating somewhere outside the focus, most notably in the propagation path, an effect commonly referred to as "pre-focal heating" [106,107].

Given the threshold nature of cavitation, however, it is possible to create a strong likelihood of cavitation at the focus while maintaining sub-threshold pressure levels everywhere else. As opposed to simply increasing the temperature rise everywhere, the heating is very localized. An obvious benefit to cavitation-enhanced hyperthermia is that one can achieve therapeutically relevant temperature rises at low insonation times that are comparable to that generated by much longer insonation times through primary heating alone (e.g., see Fig. 3.28 and Fig. 3.29). Comparable heating in less time means a reduced risk of collateral thermal bioeffect outside the immediate focal region. The experimental results demonstrated that the threshold for enhanced heating did not vary significantly as a function of insonation duration when the likelihood was at or near 100% (the onset for at least one instance was more varied). In addition the enhanced heating level and overall temperature change were often comparable as a function of insonation duration. As a result, this apparent non-effect of insonation duration in actuality has important implications for localized heating.

The objective of the numerical simulations was to determine the feasibility of bubbles as an enhanced heating mechanism, and in the process to identify likely heating mechanisms. The first interesting result is that the peak power deposition due to both viscous dissipation and secondary acoustic emission are of the same order of magnitude in the parameter range we were concerned with. These peak values did not occur for the same bubble equilibrium size and phantom viscosity however. Taken in this context, these results may not appear helpful to the process of identifying a dominant mechanism, or reducing the possible parameter range for bubble size and viscosity, other than to suggest that both mechanisms and nearly all bubbles are important.

However, taken in the context of the experimental results, the message to be taken from these numerical simulations is that the inertial bubbles which are favored by the PCD system are capable

of some of the highest power deposition, and remain likely candidates for bubble-related heating. In addition, the range of parameter space (bubble size and viscosity) for which inertial bubbles possess near peak values for power deposition is much larger than that of large noninertial bubbles with peak values for viscous dissipation. As a result, for a comparable number of noninertial and inertial bubbles, the noninertial bubbles must be much more uniform in size, and the possible phantom viscosity is limited to a much smaller range of potential values.

When evaluating the number of bubbles required to produce the enhanced heating effect, it was found that less than 100 bubbles were necessary for an insonation time of 2 seconds and acoustic pressure amplitudes of 2.8 MPa and below. This number represents the number of "optimal" bubbles that are required, or bubbles exhibiting peak, or near peak power deposition. For a distribution of bubbles with varying size the number will grow; however, the prediction for optimal bubbles is very small in absolute terms, and relative to the volume of the region where cavitation is presumed to occur. As a result, two, three, or even four times the number of optimal bubbles with a broader distribution in size and power deposition is not an unreasonable number of bubbles in many cases.

These results may be summarized in the following conclusions:

(1) There is a correlation between the onset of enhanced heating and observable cavitation in both time and acoustic pressure amplitude. This is attributed to cavitation activity being the cause of the enhanced heating.

(2) There is a correlation between the relative change of magnitude of enhanced heating and observable cavitation activity, including a saturation in both effects that may occur above the threshold pressure for enhanced heating.

(3) The nature of the cavitation activity, as indicated by the PCD system, is most likely inertial cavitation activity although the possibility of highly nonlinear, but noninertial bubbles cannot be excluded.

(4) Insonation times of 0.1 to 5 seconds do not significantly affect the threshold pressure for a "guaranteed" repeatability of cavitation activity. The threshold pressure was 2.6 MPa.

(5) Insonation times of 0.5 to 5 seconds do not substantially affect the threshold pressure for cavitation activity in the absence of requirements on the repeatability of cavitation activity. For an insonation duration of 0.1 seconds, this threshold increases between 0.2 and 0.4 MPa.

(6) Insonation duration has a similar effect on the threshold pressure for enhanced heating and on the enhanced heating level. The results are largely independent of insonation time for 0.5 to 5 seconds, however thresholds and the enhanced heating levels show a slight increase and slight decrease respectively.

(7) Peak values for viscous and secondary acoustic power deposition are of the same order of magnitude over the range of parameters $0.1 \leq R_0 \leq 50\mu$m and $0.001 \leq \mu \leq 0.1$ N·s/m^2.

(8) The enhanced heating effect can be attributed to less than 100 “optimally-sized” bubbles exhibiting maximal power deposition – or some greater number of bubbles residing in a broader size distribution.

(9) The excellent correlation between enhanced heating and PCD-measured cavitation activity suggests that the dominant physical mechanism leading to elevated heating is the absorption of broadband acoustic emission associated with the collapse of inertial cavitation bubbles. This conclusion is bolstered by existing questions regarding the likelihood of sub-resonant bubbles successfully growing through resonance to super-resonant size, the magnitude of the secondary acoustic power deposition and the large range of bubble sizes and phantom viscosity where inertial cavitation power deposition comparable to that of the “optimal” bubbles, suggest a primary role for inertial bubbles in the enhanced heating effect.

(10) The excellent correlation between enhanced heating and PCD-measured cavitation activity suggests that one could use a PCD to non-invasively monitor the enhanced heating process, or even as a means for feedback control and/or exposure optimization.

6.2 Suggestions for Further Study

6.2.1 Experimental

The primary concern in the experimental work is the lack of knowledge regarding the bubble field parameters (size distribution, spatial distribution, number) as well as issues not directly discussed such as stability and longevity. Many of the limitations and assumptions of the modeling effort could be mitigated with knowledge of these parameters. Two techniques stand out for implementing at least a partial a solution to these unknowns: (1) removing some uncertainty in the bubble population by providing known cavitation nuclei (2) employing an optical or other means of “observing” the bubble population during insonation.

A variety of non-biologically relevant (*e.g.*, polystyrene spheres) and biologically relevant (*e.g.*, contrast agents) materials are available as potential nuclei. By “seeding” tissue phantoms or tissue samples with microbubbles with a known size distribution, it may be possible to gain further insight into the role of bubble size in the enhanced heating effect. This would occur by simply having a better understanding of the possible bubble sizes detected, but would also allow the parameter ranges in the modeling to be reduced.

Developing a means to directly observe the bubble population could mitigate any need to know, or attempt to influence by seeding, the bubble population. Tissue phantoms are available which

are optically transparent, and may be suitable for this task. However, the problem of detecting, tracking, measuring, and following the changes of bubbles in a three-dimensional volume, preferably dynamically, is not solved by simply using an optically transparent phantom.

Several experiments could be performed, even with the current apparatus, the would yield additional information. The resolution of the insonation duration measurements could be improved around the threshold pressure now that the general region has been determined. This, in conjunction with additional insonation times, would provide a better understanding as to the exact role of insonation duration on the threshold for enhanced heating, including a more precise determination of how the threshold pressure may increase with insonation duration below 0.5 seconds.

6.2.2 Modeling

There are several components to the numerical modeling, each of which may be improved. A core issue is again the uncertainty in parameters, particularly bubble-related parameters. As long as this information remains elusive, any model, regardless of the completeness of the physical description, will be reduced to providing imprecise estimates based on the variability of these parameters. Aside from this uncertainty, specific improvements can be made to the physics of these models.

A potential concern for the FDTD pressure solution is whether there are sufficient bubbles present to significantly alter the acoustic field. Chavrier *et al.* [38] began an effort to investigate how a high density of bubbles may influence the sound propagation. For a small quantity of small bubbles, it is not clear that this should be a primary concern. An additional consideration is the possible change in material properties as the temperature changes. This would require that both the solution to the pressure equation and the bioheat transfer equation (BHTE) be solved simultaneously.

As more information is gained regarding the bubble parameters, and the solution moves from a power density distribution possibly to a discrete implementation of bubbles, it may be necessary to move to a three-dimensional version of the BHTE. Using cylindrical symmetry and discrete bubble placement, it is assumed that for every bubble, at a given axial and radial location, one exists at every point around the entire acoustic axis. The concern in moving to three dimensions for the

BHTE is that one must also do that for the pressure solution if the two solutions are coupled to enable temperature dependent changes in material properties, for example. As discussed earlier, the pressure solution is computationally more intensive which may make this infeasible for the near future.

Improvements may be made in the solution to the motion of the bubble wall as well. The use of more complicated, yet physically more accurate models for the tissue rheology is ultimately appropriate for a non-Newtonian medium such as the tissue phantoms. Investigating the mechanical and diffusive stability of these bubbles, based on their size and their motion would be a worthwhile investment as well. As a practical issue, it may reduce the range of bubble sizes under evaluation without requiring direct knowledge, simply by knowing that some bubble sizes just will not survive.

Additional experiments and improvements to the modeling may prove useful as well. Nevertheless, we believe there is strong experimental evidence for the role of and relationship between cavitation activity, specifically inertial cavitation activity, and the enhanced heating effect, and support for this belief through models which indicate a reasonable number of bubbles could be responsible. We hope this may serve as a basis for additional experimental investigations and modeling to further the understanding of this process.

Appendix A

Finite-Difference Time Domain Code: Pressure Solution

The following code is used to calculate the pressure field in the water-phantom domain as described in Chapter 5.

```
      PROGRAM nonlinear

      IMPLICIT NONE

      INTEGER Imaxp, Jmaxp, Narray, Ntrain, Nmaxp, ifocusp, jfocusp,
     & ImaxT, JmaxT, Nsonic, NstepT, itargetT, jtargetT, ifocusT,
     & jfocusT, Np, itc, jtc

      PARAMETER (Imaxp = 1001, Jmaxp = 501, Narray = 351, Nmaxp = 10001,
     & Ntrain = 10001, ifocusp = 651, jfocusp = 1, Np = 25, itc = 351,
     & jtc = 6, ImaxT = 651, JmaxT = 111, Nsonic = 1001, itargetT = 327,
     & jtargetT = 1, ifocusT = 351, jfocusT = 1)

      DOUBLE PRECISION drp, dxp, dtp, t, cp(Imaxp,Jmaxp),
     & rhop(Imaxp,Jmaxp), alphap(Imaxp,Jmaxp), Betap(Imaxp,Jmaxp),
     & xshock, xtarget, xmaxp, rtarget, rmaxp, tmaxp, pi, period, freq,
     & omega, kwave, lambda, tendtoend, Umax, Mach, train(Ntrain),
     & trainmult, pnplus1(Imaxp,Jmaxp), pn(Imaxp,Jmaxp),
     & pnminus1(Imaxp,Jmaxp), pnminus2(Imaxp,Jmaxp), q1, q2, q3, q4,
     & pnminus3(Imaxp,Jmaxp), Qn, Q(ImaxT,JmaxT), BetaH2O, cH2Op,
     & rhoH2O, ctissp, rhotiss, Betatiss, P0, pfocusmax, pfocusmin,
     & alphaH2O, alphatiss, Qmax, ptcmax, ptcmin

      INTEGER i, j, n, m, k, itargetp, jtargetp, Nptspercycle,
     & nendtoend, ielement(Narray), jelement(Narray), maxvalip,
     & maxvaljp, minvalip, minvaljp, dumpnumber, Naverage, maxvaliT,
     & maxvaljT, minvaliT, minvaljT, i0, j0, maxvaliQ, maxvaljQ

      CHARACTER*50 infile1, trainfile, TvsPfile, arrayfile, Ttracefile,
     & Qfile, filename

      DATA infile1/'bowl_press.in'/

      CALL readparams(drp, dxp, dtp, Nptspercycle, Naverage, P0, cH2Op,
```

```
     & rhoH2O, BetaH2O, ctissp, rhotiss, Betatiss, alphaH2O,
     & alphatiss, infile1, trainfile, TvsPfile, arrayfile, Qfile)

      CALL icfiles(cp, rhop, alphap, Betap, cH2Op, rhoH2O, BetaH2O,
     & ctissp, rhotiss, Betatiss, alphaH2O, alphatiss, Imaxp, Jmaxp,
     & ImaxT, JmaxT)

      CALL readtrain(train, n, Ntrain, trainfile)

      CALL cylarray(Narray, arrayfile, ielement, jelement, itargetp,
     & jtargetp)

      CALL calcparams(rmaxp, drp, Imaxp, Jmaxp, xmaxp, dxp, tmaxp, dtp,
     & Nmaxp, pi, period, Nptspercycle, freq, omega, lambda, kwave,
     & tendtoend, nendtoend, P0, cH2Op, rhoH2O, BetaH2O, itargetp,
     & jtargetp, rtarget, xtarget, q1, q2, q3, q4, xshock, Umax, Mach)

      CALL displayparams(drp, dxp, dtp, freq, lambda, kwave, cH2Op,
     & rhoH2O, BetaH2O, Umax, Mach, tmaxp, tendtoend, xshock,
     & Nptspercycle, Nmaxp, nendtoend, Imaxp, Jmaxp, rmaxp,xmaxp,
     & itargetp, jtargetp, rtarget, xtarget, ImaxT, JmaxT)

      ! Open the TvsPfile file
      open(1, file = TvsPfile, form = 'formatted', status = 'unknown')
      print*
      print*, 'Opened ', TvsPfile

      ! Loop over pressure amplitudes
      do 90 k = 11, Np
        trainmult = k * P0

        CALL initialize(Imaxp, Jmaxp, pn, pnplus1, pnminus1, pnminus2,
     &    pnminus3, Q, ImaxT, JmaxT)

        pfocusmax = 0.d0
        pfocusmin = 0.d0
        ptcmax = 0.d0
        ptcmin = 0.d0

        ! Start time-stepping
        t = 0.d0

        do 10 n = 1, Nmaxp

          ! Use the input wave train file at array locations to drive
          if (n.le.Ntrain) then
            do 20 m = 1, Narray
              pn(ielement(m),jelement(m)) = trainmult * train(n)
20          continue
          end if

          CALL fdtd2s2t(pn, pnplus1, pnminus1, pnminus2, pnminus3, q1,
     &      q2, q3, q4, drp, dxp, dtp, Imaxp, Jmaxp, cp, rhop, alphap,
     &      Betap, omega, Narray, ielement, jelement)
```

```
        ! Find pressure amplitude at the real focus and TC at the
        ! last cycle
        if (Nmaxp-n.le.Nptspercycle)then
          pfocusmax = MAX(pfocusmax, pn(ifocusp,jfocusp))
          pfocusmin = MIN(pfocusmin, pn(ifocusp,jfocusp))
          ptcmax = MAX(ptcmax, pn(ifocusp,jtc))
          ptcmin = MIN(ptcmin, pn(ifocusp,jtc))
        end if

        ! Collect intensity integral over the last ten cycles
        if (n.ge.(Nmaxp-Naverage).and.n.lt.Nmaxp)then
          do 40 j = 1, JmaxT
            do 30 i = 1, ImaxT
              i0 = i + 300
              Qn = ((3.d0 * pn(i0,j) - 4.d0 * pnminus1(i0,j) +
     &          pnminus2(i0,j)) / (2.d0*dtp))**2 /
     &          (omega * omega * rhop(i0,j) * cp(i0,j))
              Q(i,j) = Q(i,j) + Qn
 30         continue
 40       continue
        end if

        CALL updatep(Imaxp, Jmaxp, pn, pnplus1, pnminus1, pnminus2,
     &    pnminus3)

        t = t + dtp
 10   continue

      do 60 j = 1, JmaxT
        do 50 i = 1, ImaxT
          Q(i,j) = Q(i,j) / DBLE(Naverage)
 50     continue
 60   continue

      ! Dump the intensity Qfile
      if (k.lt.10) then
        write(filename,101) Qfile, '0', k, '.dat'
101     format(a35,a1,i1,a4)
      else
        write(filename,102) Qfile, k, '.dat'
102     format(a35,i2,a4)
      end if

      open(4, file = filename, form = 'formatted', status = 'unknown')
      do 80 j = 1, JmaxT
        do 70 i = 1, ImaxT
          write(4,103) Q(i,j)
 70     continue
 80   continue
103   format(E15.9)

      close(4)
```

```
        ! Find where the maximum intensity is
        CALL maxQ(Q, ImaxT, JmaxT, Qmax, maxvaliQ, maxvaljQ)

        print*
        print 104, trainmult
  104   format ('P0 = ', e14.7)

        ! Display the pressure at focus
        print 105, pfocusmax
  105   format ('  Peak Positive Focus Pressure: ',e14.7)
        print 106, pfocusmin
  106   format ('  Peak Negative Focus Pressure: ',e14.7)

         ! Display the pressure at focus
        print 107, ptcmax
  107   format ('  Peak Positive Thermcouple Pressure: ',e14.7)
        print 108, ptcmin
  108   format ('  Peak Negative Thermcouple Pressure: ',e14.7)

        ! Display where the maximum intensity is
        print*
        print 109, Qmax, maxvaliQ, maxvaljQ
  109   format ('  Maximum Intensity:', e14.7, ' at (',I4,',',I4,')')

        ! Save to TvsP File
        write(1,110) k, trainmult, pfocusmax, pfocusmin, ptcmax, ptcmin
  110   format(i2, 5(e14.7, 1x))

   90 continue

      close(1)

      print*
      print*,'Closed ', TvsPfile, '.'

      END

! ----------------------------------------------------------------------
!     READPARAMS
! ----------------------------------------------------------------------
      SUBROUTINE readparams(drp, dxp, dtp, Nptspercycle, Naverage,
     & P0, cH2Op, rhoH2O, BetaH2O, ctissp, rhotiss, Betatiss, alphaH2O,
     & alphatiss, infile1, trainfile, TvsPfile, arrayfile, Qfile)

      IMPLICIT NONE

      DOUBLE PRECISION drp, dxp, dtp, P0, cH2Op, rhoH2O, BetaH2O,
     & ctissp, rhotiss, Betatiss, alphaH2O, alphatiss

      INTEGER Nptspercycle, Naverage

      CHARACTER*50 infile1, trainfile, TvsPfile, arrayfile, Qfile

      ! Read the pressure's input parameters from input file
```

```
      print*, 'READPARAMS'
      open(unit = 1,file = infile1, status = 'unknown')
      print*, '  Opened ', infile1
      read(1,*) drp, dxp, dtp, Nptspercycle
      read(1,*) trainfile
      read(1,*) TvsPfile
      read(1,*) P0
      read(1,*) arrayfile
      read(1,*) cH2Op, rhoH2O, BetaH2O, alphaH2O
      read(1,*) ctissp, rhotiss, Betatiss, alphatiss
      read(1,*) Naverage

      read(1,*) Qfile
      close(1)
      print*, '  Closed ', infile1

      RETURN
      END

! ----------------------------------------------------------------------
!      ICFILES
! ----------------------------------------------------------------------
      SUBROUTINE icfiles(cp, rhop, alphap, Betap, cH2Op, rhoH2O,
     & BetaH2O, ctissp, rhotiss, Betatiss, alphaH2O, alphatiss, Imaxp,
     & Jmaxp, ImaxT, JmaxT)

      IMPLICIT NONE

      DOUBLE PRECISION cp(Imaxp,Jmaxp), rhop(Imaxp,Jmaxp),
     & alphap(Imaxp,Jmaxp), Betap(Imaxp,Jmaxp), cH2Op, rhoH2O, BetaH2O,
     & ctissp, rhotiss, Betatiss, alphaH2O, alphatiss

      INTEGER i, j, Imaxp, Jmaxp, ImaxT, JmaxT

      print*
      print*, 'ICFILES'

      do 20 j = 1, Jmaxp
        do 10 i = 1, Imaxp
          cp(i,j) = cH2Op
          rhop(i,j) = rhoH2O
          alphap(i,j) = alphaH2O
          Betap(i,j) = BetaH2O
   10   continue
   20  continue

      ! Phantom fill the domain: x=30:95mm, r=0:11mm drp=drx=0.1mm
      do 40 i = 301, 951
        do 30 j = 1, 111
          cp(i,j) = ctissp
          rhop(i,j) = rhotiss
          alphap(i,j) = alphatiss
          Betap(i,j) = Betatiss
   30   continue
```

```
   40 continue

      print*, '  Properties of water:'
      print 100, cH2Op
  100 format('   Speed of sound: ',F7.2,' m/s')
      print 110, rhoH2O
  110 format('   Density: ',F7.2,' kg/m^3')
      print 120, alphaH2O
  120 format('   Absorption: ',F6.3,' np')
      print 130, BetaH2O
  130 format('   Nonlinearity: ',F6.3,'')
      print*, '  Properties of tissue:'
      print 140, ctissp
  140 format('   Speed of sound: ',F7.2,' m/s')
      print 150, '     rhotiss = ', rhotiss
  150 format('   Density: ',F7.2,' kg/m^3')
      print 160, '     alphaH2O = ', alphaH2O
  160 format('   Absorption: ',F6.3,' np')
      print 170, '     BetaH2O = ', BetaH2O
  170 format('   Nonlinearity: ',F6.3,'')

      RETURN
      END

! ---------------------------------------------------------------------
!     INITIALIZE
! ---------------------------------------------------------------------
      SUBROUTINE initialize(Imaxp, Jmaxp, pn, pnplus1, pnminus1,
     & pnminus2, pnminus3, Q, ImaxT, JmaxT)

      IMPLICIT NONE

      INTEGER i, j, Imaxp, Jmaxp, ImaxT, JmaxT

      DOUBLE PRECISION pn(Imaxp,Jmaxp),pnplus1(Imaxp,Jmaxp),
     & pnminus1(Imaxp,Jmaxp), pnminus2(Imaxp,Jmaxp),
     & pnminus3(Imaxp,Jmaxp), Q(ImaxT,JmaxT)

      print*
      print*, 'INITIALIZE'

      ! Initialize pressure field to zero everywhere
      print*, '  Initializing pressure arrays.'
      do 30 j = 1 ,Jmaxp
         do 20 i = 1, Imaxp
            pn(i,j) = 0.d0
            pnplus1(i,j) = 0.d0
            pnminus1(i,j) = 0.d0
            pnminus2(i,j) = 0.d0
            pnminus3(i,j) = 0.d0
   20   continue
   30 continue

      do 50 j = 1, JmaxT
```

```
        do 40 i = 1, ImaxT
          Q(i,j) = 0.d0
   40   continue
   50 continue

      RETURN
      END

! ----------------------------------------------------------------------
!     READTRAIN
! ----------------------------------------------------------------------
      SUBROUTINE readtrain(train, n, Ntrain, trainfile)

      IMPLICIT NONE

      DOUBLE PRECISION train(Ntrain)

      INTEGER n, Ntrain

      CHARACTER*50 trainfile

      ! Read in wave train data file
      print*
      print*, 'READTRAIN'
      open(unit = 1, file = trainfile, status = 'unknown')
      print*, '  Opened ', trainfile

      do 10 n = 1, Ntrain
        read(1,*) train(n)
   10 continue

      close(1)
      print*, '  Closed ', trainfile

      RETURN
      END

! ----------------------------------------------------------------------
!     CYLARRAY
! ----------------------------------------------------------------------
      SUBROUTINE cylarray(Narray, arrayfile, ielement, jelement
     & , itargetp, jtargetp)

      IMPLICIT NONE

      DOUBLE PRECISION temp1, temp2

      INTEGER n, Narray, ielement(Narray), jelement(Narray),
     & itargetp, jtargetp

      CHARACTER*50 arrayfile

      print*
      print*,'CYLARRAY'
```

```
      open(1, file=arrayfile, form='formatted', status='unknown')
      print*, '  Opened ', arrayfile

      read(1,*) temp1, temp2
      itargetp = INT(temp1)
      jtargetp = INT(temp2)

      do 10 n=1,Narray
        read(1,*) temp1, temp2
        ielement(n) = INT(temp1)
        jelement(n) = INT(temp2)
   10 continue

      close(1)
      print*, '  Closed ', arrayfile

      RETURN
      END

! ----------------------------------------------------------------------
!     CALCPARAMS
! ----------------------------------------------------------------------
      SUBROUTINE calcparams(rmaxp, drp, Imaxp, Jmaxp, xmaxp, dxp, tmaxp,
     & dtp, Nmaxp, pi, period, Nptspercycle, freq, omega, lambda, kwave,
     & tendtoend, nendtoend, P0, cH2Op, rhoH2O, BetaH2O, itargetp,
     & jtargetp, rtarget, xtarget, q1, q2, q3, q4, xshock, Umax, Mach)

      IMPLICIT NONE

      DOUBLE PRECISION rmaxp, drp, xmaxp, dxp, tmaxp, dtp, pi, period,
     & freq, omega, lambda, kwave, tendtoend, Umax, P0, Mach, xshock,
     & rtarget, xtarget, cH2Op, rhoH2O, BetaH2O, q1, q2, q3, q4

      INTEGER Imaxp, Jmaxp, Nmaxp, Nptspercycle, nendtoend, itargetp,
     & jtargetp, i, j

      print*
      print*,'CALCPARAMS'

      ! Calculate some basic run parameters:
      rmaxp = drp * DBLE(Jmaxp - 1)
      xmaxp = dxp * DBLE(Imaxp - 1)
      tmaxp = dtp * DBLE(Nmaxp - 1)
      pi = ACOS(-1.d0)
      period = dtp * DBLE(Nptspercycle)
      freq = 1.d0 / period
      omega = 2.d0 * pi * freq
      lambda = cH2Op * period
      kwave = omega / cH2Op
      tendtoend = xmaxp / cH2Op
      nendtoend = INT(tendtoend / dtp)
      Umax = P0 /(rhoH2O * cH2Op)
      Mach = Umax / cH2Op
```

```
      xshock = 1.d0 / (BetaH2O * Mach * kwave)

      ! Calculate where all the x's are at:
      xtarget = dxp * DBLE(itargetp - 1)
      rtarget = drp * DBLE(jtargetp - 1)

      q1 = dtp * dtp / (drp * drp)
      q2 = dtp * dtp / (2.d0 * drp)
      q3 = dtp * dtp / (dxp * dxp)
      q4 = 2.d0 / (omega * omega * dtp)

      RETURN
      END

! ----------------------------------------------------------------------
!     DISPLAYPARAMS
! ----------------------------------------------------------------------
      SUBROUTINE displayparams(drp, dxp, dtp, freq, lambda, kwave,
     & cH2Op, rhoH2O, BetaH2O, Umax, Mach, tmaxp, tendtoend, xshock,
     & Nptspercycle, Nmaxp, nendtoend, Imaxp, Jmaxp, rmaxp, xmaxp,
     & itargetp, jtargetp, rtarget, xtarget, ImaxT, JmaxT)

      IMPLICIT NONE

      DOUBLE PRECISION drp, dxp, dtp, freq, lambda, kwave, cH2Op,
     & rhoH2O, BetaH2O, Umax, Mach, tmaxp, tendtoend, xshock, rmaxp,
     & xmaxp, rtarget, xtarget

      INTEGER Nptspercycle, Nmaxp, nendtoend, Imaxp, Jmaxp, itargetp,
     & jtargetp, ImaxT, JmaxT

      ! Put some initial info on the screen so user knows what to expect
      print*
      print*,'DISPLAYPARAMS'

      print 10, dxp * 1.d3
   10 format('   dx = ', F4.2, ' mm')

      print 20, drp * 1.d3
   20 format('   dr = ', F4.2, ' mm')

      print 30, dtp * 1.d6
   30 format('   dt = ', F4.2, ' microseconds')

      print 40, freq/1.d6
   40 format('   Frequency: ',F4.2,' MHz')
      print 50, Nptspercycle
   50 format('   Number of samples per period: ',I4)
      print 60, INT(lambda/dxp)
   60 format('   Number of samples per wavelength: ',I3)
      print 70, lambda*1.d3
   70 format('   Wavelength in 1500m/s water: ',F6.3,' mm')
      print 80, kwave
   80 format('   Wave number: ',F6.1)
```

```
      print 200, Umax
  200 format('   Maximum particle velocity is ',E11.4,' m/sec')
      print 210, Mach
  210 format('   Acoustic Mach number is about ',E11.4)
      print*
      print 230, tendtoend*1.d6,nendtoend
  230 format('   Signal travels end to end in ',F8.4,' microseconds (',
     &I6,' steps)')
      print 235, tmaxp*1.d6,Nmaxp
  235 format('   Max calculation time is ',E10.3,' microseconds (',
     &I6,' steps)')
      print 240, xtarget*100.d0, itargetp
  240 format('   Focus is at x =',F7.3,' cm (i=',I5,')')
      print 245, rtarget*100.d0, jtargetp
  245 format('   Focus is at r =',F7.3,' cm (j=',I5,')')
      print 250, xmaxp*100.d0,Imaxp
  250 format('   X max is ',F7.3,' cm (i=',I5,')')
      print 260, rmaxp*100.d0,Jmaxp
  260 format('   R max is ',F7.3,' cm (j=',I5,')')
      print 270, xshock*100.d0,INT(xshock/dxp)
  270 format('   Shock forms at x = ',F7.3,' cm (i=',I6,')')
      print 275, xshock*1.d6/cH2Op,INT((xshock/cH2Op)/dtp)
  275 format('   Shock forms at t = ',E11.5,' microseconds (',I7,')')

      RETURN
      END

! ----------------------------------------------------------------------
! FDTD2S2T
! ----------------------------------------------------------------------
      SUBROUTINE fdtd2s2t(pn, pnplus1, pnminus1, pnminus2, pnminus3,
     & q1, q2, q3, q4, drp, dxp, dtp, Imaxp, Jmaxp, cp, rhop, alphap,
     & Betap, omega, Narray, ielement, jelement)

      IMPLICIT NONE

      DOUBLE PRECISION pn(Imaxp,Jmaxp), pnplus1(Imaxp,Jmaxp),
     & pnminus1(Imaxp,Jmaxp), pnminus2(Imaxp,Jmaxp),
     & pnminus3(Imaxp,Jmaxp), z1, z2, z3, z4, z5, z6, z7, drp, dxp,
     & dtp, q1, q2, q3, q4, cp(Imaxp,Jmaxp), rhop(Imaxp,Jmaxp),
     & alphap(Imaxp,Jmaxp), Betap(Imaxp,Jmaxp), omega, r

      INTEGER i, j, Imaxp, Jmaxp, Narray, ielement(Narray),
     & jelement(Narray), I0

      ! Put in first order Mur BC's at r=rmax, ie, j=Jmax:
      do 60 i = 1, Imaxp
        pn(i,Jmaxp) = pnminus1(i,Jmaxp-1) + ((cp(i,Jmaxp)*dtp-drp) /
     &    (cp(i,Jmaxp)*dtp+drp)) * (pn(i,Jmaxp-1) - pnminus1(i,Jmaxp))
   60 continue

      ! Put in first order Mur BC's at x=xmax, ie, i=Imax:
      do 50 j = 1, Jmaxp
        pn(Imaxp,j) = pnminus1(Imaxp-1,j) + ((cp(Imaxp,j)*dtp-dxp) /
```

```
     &    (cp(Imaxp,j)*dtp+dxp)) * (pn(Imaxp-1,j) - pnminus1(Imaxp,j))
   50 continue

      ! Put symmetric BC's at j=1, r=0
      do 40 i = 2, Imaxp - 1
        z1 = 2.d0*(pn(i,2)-pn(i,1))
        z3 = pn(i+1,1)-2.d0*pn(i,1)+pn(i-1,1)
        z4 = pn(i,1)-3*pnminus1(i,1)+3*pnminus2(i,1)-pnminus3(i,1)
        z5 = pn(i,1)*(2.d0*pn(i,1)-5.d0*pnminus1(i,1)
     &     +4.d0*pnminus2(i,1)-pnminus3(i,1))
        z6 = (3.d0*pn(i,1)-4.d0*pnminus1(i,1)+pnminus2(i,1))**2
        z7 = -2.d0*pn(i,1)+pnminus1(i,1)
        pnplus1(i,1) = (cp(i,1)*cp(i,1))*(q1*z1+q3*z3) +
     &    cp(i,1)*alphap(i,1)*q4*z4 + (2.d0*Betap(i,1)
     &    / (rhop(i,1)*cp(i,1)*cp(i,1)))*(z5+z6/4.d0) - z7
   40 continue

      ! Put in first order Mur BC's at i=ielement(Narray)
      i = ielement(Narray)
      do 30 j = jelement(Narray), Jmaxp
        pn(i,j) = pnminus1(i+1,j) + ((cp(i,j)*dtp-dxp) /
     &    (cp(i,j)*dtp+dxp)) * (pn(i+1,j) - pnminus1(i,j))
   30 continue

      ! Inside cells
      do 10 j = 2, Jmaxp - 1
        r=(j - 1) * drp
        if (j.le.jelement(Narray)) then
          I0 = ielement(j) + 1
        else
          I0 = ielement(Narray) + 1
        end if
        do 20 i = I0, Imaxp - 1
          z1 = pn(i,j+1) - 2.d0*pn(i,j)+pn(i,j-1)
          z2 = pn(i,j+1) - pn(i,j-1)
          z3 = pn(i+1,j) - 2.d0*pn(i,j)+pn(i-1,j)
          z4 = pn(i,j) - 3*pnminus1(i,j) + 3*pnminus2(i,j)-pnminus3(i,j)
          z5 = pn(i,j) * (2.d0*pn(i,j) - 5.d0*pnminus1(i,j)
     &         + 4.d0*pnminus2(i,j) - pnminus3(i,j))
          z6 = (3.d0*pn(i,j) - 4.d0*pnminus1(i,j) + pnminus2(i,j))**2
          z7 = -2.d0*pn(i,j) + pnminus1(i,j)
          pnplus1(i,j) = (cp(i,j)*cp(i,j)) * (q1*z1+q2*z2/r+q3*z3)
     &      + cp(i,j) * alphap(i,j)*q4*z4 + (2.d0*Betap(i,j)
     &      / (rhop(i,j) * cp(i,j) * cp(i,j))) * (z5+z6/4.d0) - z7
   20   continue
   10 continue

      RETURN
      END

! ----------------------------------------------------------------------
! UPDATEP
! ----------------------------------------------------------------------
      SUBROUTINE updatep(Imax, Jmax, pn, pnplus1, pnminus1, pnminus2,
```

```
     & pnminus3)

      IMPLICIT NONE

      DOUBLE PRECISION pn(Imax,Jmax), pnplus1(Imax,Jmax)
     & ,pnminus1(Imax,Jmax), pnminus2(Imax,Jmax), pnminus3(Imax,Jmax)

      INTEGER i, j, Imax, Jmax

      ! Update arrays in time.
      do 20 j = 1, Jmax
        do 10 i = 1, Imax
          pnminus3(i,j) = pnminus2(i,j)
          pnminus2(i,j) = pnminus1(i,j)
          pnminus1(i,j) = pn(i,j)
          pn(i,j) = pnplus1(i,j)
   10   continue
   20 continue

      RETURN
      END

! ----------------------------------------------------------------------
! MAXQ
! ----------------------------------------------------------------------
      SUBROUTINE maxQ(Q, Imax, Jmax, Qmax, maxvali, maxvalj)

      DOUBLE PRECISION Q(Imax,Jmax), Qmax

      INTEGER i, j, Imax, Jmax, maxvali, maxvalj

      Qmax = Q(1,1)
      maxvalj = 1

      ! Find maximum along acoustic axis
      do 10 i = 1, Imax
        if(Q(i,1).gt.Qmax)then
          Qmax = Q(i,1)
          maxvali = i
        end if
   10 continue

      RETURN
      END
```

Appendix B

Finite-Difference Time Domain Code: BHTE Solution

The following code is used to calculate the temperature field in the phantom domain as described in Chapter 5.

```
      PROGRAM bioheat

      IMPLICIT NONE

      INTEGER ImaxT, JmaxT, NmaxT, Np, Nsonic, ifoc, jfoc, itc, jtc

      PARAMETER(ImaxT = 651, JmaxT = 111,
     &  ifoc = 351, jfoc= 1, itc = 351, jtc = 6)

      DOUBLE PRECISION t, drT, dxT, dtT, Q(ImaxT,JmaxT),
     &  Tn(ImaxT,JmaxT), Tnminus1(ImaxT,JmaxT), Tnplus1(ImaxT,JmaxT),
     &  rhotiss, alphatiss, CtissT, Ktiss, Cblood, Wblood, Ta, Tb,
     &  Ttcmax, Tfcmax, qh1, qh2, qh3, qh4, readval, Qb, QbFac

      INTEGER i, j, n, m, k, ks, Nsonic, NmaxT, Np, bubbleSourceType

      CHARACTER*50 infile, TvsPfile, Ttracefile, filename,
     &  TempSavePrefix

      DATA infile/'param.in'/

      CALL READPARAMS(infile, rhotiss, TvsPfile, drT, dxT, dtT,
     &  Wblood, Cblood, Ta, Tb, Ttracefile, CtissT, Ktiss, alphatiss,
     &  TempSavePrefix, ks, NP, Nsonic, NmaxT, Qb, bubbleSourceType)

      CALL CALCPARAMS(dtT, drT, dxT, Cblood, qh1, qh2, qh3, qh4)

      CALL DISPLAYPARAMS(drT, dxT, dtT, ImaxT, JmaxT, NmaxT)

      ! Open the TvsPfile file
      open(3, file = TvsPfile, form = 'formatted', status = 'unknown')

      print*
      print*, 'Opened ', TvsPfile
```

```
      do 10 k = ks, Np

        CALL INITIALIZE(Ta, ImaxT, JmaxT, Tn, Tnplus1, Tnminus1)

        ! Read from the intensity Qfile
        if (k.lt.10) then
          write(filename,111) '/tinker/scratch/pedson/bb-02/Q0', k,
     &      '.dat'
  111     format(A31, I1, A4)
        else
          write(filename,112) '/tinker/scratch/pedson/bb-02/Q', k,
     &      '.dat'
  112     format(A30, I2, A4)
        end if

        open(4, file = filename, status = 'UNKNOWN')
        open(5, file = '/tinker/scratch/pedson/bb-02/gtestdistr.dat',
     &    status = 'UNKNOWN')
!        open(16, file = '/tinker/scratch/pedson/bb-02/test.dat',
!     &    status = 'UNKNOWN')
!        open(17, file = '/tinker/scratch/pedson/bb-02/test2.dat',
!     &    status = 'UNKNOWN')

        do 30 j = 1, JmaxT
          do 20 i = 1, ImaxT
            read(4,*) readval
            read(5,*) QbFac
            Q(i,j) = (2 * alphatiss * readval) + (QbFac * Qb)
!            write(16,207) Q(i,j)
!            write(17,207) (QbFac * Qb)
   20     continue
   30   continue
  207   format(e14.7)

        close(4)

        ! Incorporate bubble related heating terms
        !if (bubbleSourceType.eq.1) then
        !  print *, 'Q before ', Q(ifoc,jfoc)
        !  Q(ifoc,jfoc) = Q(ifoc,jfoc) + Qb
        !  print *, 'Q after ', Q(ifoc,jfoc)
        !end if

        !do 32 j = 1, 9
        !  do 22 i = 306, 396
        !    Q(i,j)= Q(i,j) + 4.3664e7
 !  22   !  continue
  ! 32   !continue

        ! Open temperature trace file
        if (k.lt.10) then
          write(filename,121) Ttracefile, 0, k, '.dat'
  121     format(A35, I1, I1, A4)
```

```
      else
        write(filename,122) Ttracefile, k, '.dat'
122     format(A35, I2, A4)
      end if

      open(2, file = filename, form = 'FORMATTED', status = 'UNKNOWN')

      t = 0.d0

      Ttcmax = 0.d0
      Tfcmax = 0.d0

      ! Branch statements (if/then) tend to hurt compiler
      ! optimizations in loops.  Rather than continually test for
      ! n == Nsonic to turn of the sound source, and save the
      ! temperature field, we can simply make two loops through the
      ! code.

      ! Start time stepping
      do 40 n = 1, Nsonic

        CALL HEAT2S1T(ImaxT, JmaxT, Q, Ta, Tb, drT, dtT, Tn, Tnminus1,
     &      Tnplus1, qh1, qh2, qh3, qh4, Ktiss, rhotiss, CtissT, Wblood)

        write(2,103) t, Tn(ifoc,jfoc) - Ta, Tn(itc,jtc) - Ta
103     format(3(e14.7, 1x))

        Ttcmax = MAX(Ttcmax, Tn(itc,jtc))
        Tfcmax = MAX(Tfcmax, Tn(ifoc,jfoc))

        CALL UPDATET(ImaxT, JmaxT, Tn, Tnplus1, Tnminus1)

        t = t + dtT
 40   continue

      CALL SAVETEMP(TempSavePrefix, ImaxT, JmaxT, Tnminus1, Ta, k)

      ! Turn off acoustic source
      do 60 j = 1, JmaxT
        do 50 i = 1, ImaxT
          Q(i,j) = 0.d0
 50     continue
 60   continue

      ! Resume time stepping
      do 70 n = Nsonic + 1, NmaxT

        CALL HEAT2S1T(ImaxT, JmaxT, Q, Ta, Tb, drT, dtT, Tn, Tnminus1,
     &      Tnplus1, qh1, qh2, qh3, qh4, Ktiss, rhotiss, CtissT, Wblood)

        write(2,103) t, Tn(ifoc,jfoc) - Ta, Tn(itc,jtc) - Ta

        Ttcmax = MAX(Ttcmax, Tn(itc,jtc))
        Tfcmax = MAX(Tfcmax, Tn(ifoc,jfoc))
```

```
          CALL UPDATET(ImaxT, JmaxT, Tn, Tnplus1, Tnminus1)

          t = t + dtT
   70   continue

        close(2)

       PRINT 802, Ttcmax - Ta
  802 FORMAT('    Maximum TC Temperature: ', e14.7)

        ! Save to TvsP File
        write(3,104) k, Tfcmax - Ta, Ttcmax - Ta
  104   format(I2, 2(E14.7))

   10 continue

       close(3)

       print *
       print *, 'Closed ', TvsPfile

       END

! ----------------------------------------------------------------------
!      READPARAMS
! ----------------------------------------------------------------------
       SUBROUTINE READPARAMS(infile, rhotiss, TvsPfile, drT, dxT,
      &  dtT, Wblood, Cblood, Ta, Tb, Ttracefile, CtissT, Ktiss,
      &  alphatiss, TempSavePrefix, ks, NP, Nsonic, NmaxT,
      &  Qb, bubbleSourceType)

       IMPLICIT NONE

       DOUBLE PRECISION rhotiss, drT, dxT, dtT, Wblood, Cblood,
      &  Ta, Tb, CtissT, Ktiss, alphatiss, Qb

       INTEGER ks, NP, Nsonic, NmaxT, bubbleSourceType

       CHARACTER*50 infile, TvsPfile, Ttracefile, TempSavePrefix

       ! Read the input parameters.
       PRINT *, 'READPARAMS'

       OPEN(unit = 1,file = infile, status = 'UNKNOWN')
       PRINT *, '  Opened ', infile

       READ(1,*) drT, dxT, dtT
       READ(1,*) Wblood, Cblood, Ta, Tb
       READ(1,*) CtissT, Ktiss, alphatiss, rhotiss
       READ(1,*) Ttracefile
       READ(1,*) TvsPfile
       READ(1,*) TempSavePrefix
       READ(1,*) ks,NP,Nsonic,NmaxT
```

```
      READ(1,*) Qb,bubbleSourceType

      CLOSE(1)
      PRINT *, '  Closed ', infile

      RETURN
      END

! ----------------------------------------------------------------------
!     CALCPARAMS
! ----------------------------------------------------------------------
      SUBROUTINE CALCPARAMS(dtT, drT, dxT, Cblood, qh1, qh2, qh3, qh4)

      IMPLICIT NONE

      DOUBLE PRECISION dtT, drT, dxT, Cblood, qh1, qh2, qh3, qh4

      PRINT *
      PRINT *, 'CALCPARAMS'

      qh1 = dtT / (drT * drT)
      qh2 = dtT / (2.d0 * drT)
      qh3 = dtT / (dxT * dxT)
      qh4 = dtT * Cblood

      RETURN
      END

! ----------------------------------------------------------------------
!     DISPLAYPARAMS
! ----------------------------------------------------------------------
      SUBROUTINE DISPLAYPARAMS(drT, dxT, dtT, ImaxT, JmaxT, NmaxT)

      IMPLICIT NONE

      DOUBLE PRECISION drT, dxT, dtT

      INTEGER ImaxT, JmaxT, NmaxT

      PRINT *
      PRINT *, 'DISPLAYPARAMS'

      PRINT 100, dxT * 1.d3
  100 FORMAT('   dx = ', F4.2, ' mm')

      PRINT 110, drT * 1.d3
  110 FORMAT('   dr = ', F4.2, ' mm')

      PRINT 120, dtT * 1.d3
  120 FORMAT('   dt = ', F4.2, ' ms')

      PRINT 130, dxT * DBLE(ImaxT - 1) * 100.d0, ImaxT
  130 FORMAT('   X max is ', F7.3, ' cm (i =',I5,')')
```

```
      PRINT 140, drT * DBLE(JmaxT - 1) * 100.d0, JmaxT
  140 FORMAT('   R max is ', F7.3, ' cm (j =',I5,')')

      PRINT 150, dtT * DBLE(NmaxT - 1), NmaxT
  150 format('   Max calculation time is ', F4.2, ' seconds (',
     &  I6, ' steps)')

      RETURN
      END

! ---------------------------------------------------------------------
!     INITIALIZE
! ---------------------------------------------------------------------
      SUBROUTINE INITIALIZE(Ta, ImaxT, JmaxT, Tn, Tnplus1, Tnminus1)

      IMPLICIT NONE

      DOUBLE PRECISION dtT ,Ta, Tn(ImaxT,JmaxT), Tnplus1(ImaxT,JmaxT),
     &  Tnminus1(ImaxT,JmaxT)

      INTEGER i, j, ImaxT, JmaxT

      PRINT *
      PRINT *, 'INITIALIZE'

      PRINT *, '  Initializing temperature arrays.'
      DO 20 j = 1, JmaxT
        DO 10 i = 1, ImaxT
          Tn(i,j) = Ta
          Tnplus1(i,j) = Ta
          Tnminus1(i,j) = Ta
   10   CONTINUE
   20 CONTINUE

      RETURN
      END

! ---------------------------------------------------------------------
!     HEAT2S1T
! ---------------------------------------------------------------------
      SUBROUTINE HEAT2S1T(ImaxT, JmaxT, Q, Ta, Tb, drT, dtT, Tn,
     &  Tnminus1, Tnplus1, qh1, qh2, qh3, qh4, Ktiss, rhotiss, CtissT,
     &  Wblood)

      IMPLICIT NONE

      DOUBLE PRECISION Q(ImaxT,JmaxT), Tn(ImaxT,JmaxT),
     &  Tnminus1(ImaxT,JmaxT), Tnplus1(ImaxT,JmaxT), rhotiss, CtissT,
     &  Ktiss, Wblood, Ta, Tb, z1, z2, z3, z4, z5, r, drT, dtT, qh1,
     &  qh2, qh3, qh4, qT

      INTEGER i, j, ImaxT, JmaxT

      qT = rhotiss * CtissT
```

```
      ! r = 0, j = 1  - Symmetric BC.  All other boundary conditions are
      ! T = Ta which is the initial condition, so it requires no update.
      DO 120 i = 2, ImaxT - 1
        z1 = 2.d0 * (Tn(i,2) - Tn(i,1))
        z3 = Tn(i+1,1) - 2.d0 * Tn(i,1) + Tn(i-1,1)
        z4 = Tn(i,1) - Tb
        Tnplus1(i,1) = Tn(i,1) + (Ktiss/qT) * (qh1 * z1 + qh3 * z3)
     &    - (Wblood / qT) * qh4 * z4 + dtT * Q(i,1) / qT
  120 CONTINUE

      ! Inside cells
      DO 30 j = 2, JmaxT - 1
        r = (j - 1) * drT
        DO 40 i = 2, ImaxT - 1
           z1 = Tn(i,j+1) - 2.d0 * Tn(i,j) + Tn(i,j-1)
           z2 = Tn(i,j+1) - Tn(i,j-1)
           z3 = Tn(i+1,j) - 2.d0 * Tn(i,j) + Tn(i-1,j)
           z4 = Tn(i,j) - Tb
           Tnplus1(i,j) = Tn(i,j) + (Ktiss / qT)
     &       * (qh1 * z1 + qh2 * z2 / r + qh3 * z3)
     &       - (Wblood / qT) * qh4 * z4 + dtT * Q(i,j) / qT
   40   continue
   30   continue
      RETURN
      END

! ----------------------------------------------------------------------
!     UPDATET
! ----------------------------------------------------------------------
      SUBROUTINE UPDATET(ImaxT, JmaxT, Tn, Tnplus1, Tnminus1)

      IMPLICIT NONE

      DOUBLE PRECISION Tn(ImaxT,JmaxT), Tnplus1(ImaxT,JmaxT),
     &  Tnminus1(ImaxT,JmaxT)

      INTEGER i, j, ImaxT, JmaxT

      DO 10 j = 1, JmaxT
        DO 20 i = 1, ImaxT
          Tnminus1(i,j) = Tn(i,j)
          Tn(i,j) = Tnplus1(i,j)
   20   CONTINUE
   10 CONTINUE

      RETURN
      END

! ----------------------------------------------------------------------
!     SNAPDUMP
! ----------------------------------------------------------------------
      SUBROUTINE SAVETEMP(TempSavePrefix, ImaxT, JmaxT, Tn, Ta, k)
```

```
      IMPLICIT NONE

      DOUBLE PRECISION Tn(ImaxT,JmaxT), Ta, maxTemp, minTemp

      INTEGER ImaxT, JmaxT, i, j, k

      CHARACTER*50 TempSavePrefix, filename

      CALL MINMAX2D(Tn, ImaxT, JmaxT, maxTemp, minTemp)

      PRINT *
      PRINT 101, k
  101 FORMAT('  K = ', I2)
      PRINT 102, maxTemp - Ta
  102 FORMAT('    Maximum Temperature: ', e14.7)
      PRINT 103, minTemp - Ta
  103 FORMAT('    Minimum Temperature: ', e14.7)

      IF (k.LT.10) THEN
        WRITE(filename, 104) TempSavePrefix, '0', k, '.dat'
  104   FORMAT(A30, A1, I1, A4)
      ELSE
        WRITE(filename, 105) TempSavePrefix, k, '.dat'
  105   FORMAT(A30, I2, A4)
      END IF

      OPEN(10, file = filename, form = 'FORMATTED', status = 'UNKNOWN')

      DO 20 j = 1, JmaxT
        DO 10 i = 1, ImaxT
          WRITE(10,*) Tn(i,j) - Ta
   10   CONTINUE
   20 CONTINUE

      CLOSE(1)

      RETURN
      END

!-----------------------------------------------------------------------
!     MINMAX2D
!-----------------------------------------------------------------------
      SUBROUTINE MINMAX2D(T, Imax, Jmax, tmax, tmin)

      DOUBLE PRECISION  T(Imax,Jmax), tmax, tmin

      INTEGER i, j, Imax, Jmax

      tmax = T(1,1)
      tmin = T(1,1)

      DO 20 i = 1, Imax
        DO 10 j = 1, Jmax
           tmax = MAX(tmax, T(i,j))
```

```
         tmin = MIN(tmin, T(i,j))
10    CONTINUE
20  CONTINUE

    RETURN
    END
```

Bibliography

[1] R. G. Holt and R. A. Roy. Measurements of bubble-enhanced heating from focused mhz ultrasound in a tissue-mimicking material. Submitted, 2001.

[2] E. N. Harvey. Biological aspects of ultrasonic waves, a general survey. *Biological Bulliten*, 59:306–325, 1930.

[3] R. W. Wood and A. L. Loomis. The physical and biological effects of high frequency sound waves of great intensity. *Philosophical Magazine*, 4:419, 1927.

[4] K. E. Astrom, E. Bell, H. T. Ballantine, and E. Heidensleben. An experimental neuropathological study of the effects of high-frequency ultrasound on the brain of cat. *Journal of Neuropathology*, 20:484–520, 1961.

[5] H. E. Cline, J. F. Schenck, K. Hynynen, R. D. Watkins, S. P. Souze, and F. A. Jolesz. Magnetic resonance imaging guided focused ultrasound surgery. *Journal of Computer Assisted Tomography*, 16:956–965, 1992.

[6] A. Darkazanli, K. Hynynen, E. Unger, and J. F. Schenck. On-line monitoring of ultrasound surgery with mri. *Journal of Magnetic Resonance Imaging*, 3:509–514, 1993.

[7] K. Hynynen, A. Darkazanli, E. Unger, and J. F. Schenck. Mri-guided noninvasive ultrasound surgery. *Medical Physics*, 20:107–115, 1993.

[8] G. R. ter Haar. Ultrasound focal beam surgery. *Ultrasound in Medicine and Biology*, 21(9):1089–1100, 1995.

[9] S. Vaezy, R. Martin, U. Schmiedl, M. Caps, S. Taylor, K. Beach, S. Carter, P. Kaczkowski, G. Keilman, S. Helton, W. Chandler, P. Mourad, M. Rice, R. A. Roy, and L. Crum. Liver hemostasis using high-intensity focused ultrasound. *Ultrasound in Medicine and Biology*, 23(9):1413–1420, 1997.

[10] J. B. Pond. The role of heat in the production of ultrasonic focal leasions. *Journal of the Acoustical Society of America*, 47:1607–1611, 1970.

[11] W. Nyborg. Heat generation by ultrasound in a relaxing medium. *Journal of the Acoustical Society of America*, 70:310–312, 1981.

[12] A. D. Pierce. *Acoustics*. Acoustical Society of America, Woodbury, New York, 1994 edition, 1994.

[13] J. Wu and G. Du. Temperature rise in a tissue-mimicking material generated by unfocused and focused ultrasound transducers. *Ultrasound in Medicine and Biology*, 18:495–512, 1992.

[14] M. G. Curley. Soft tissue temperature rise caused by scanned, diagnostic ultrasound. *IEEE Transactions on Ultrasonics, Ferroelectronics, and Frequency Control*, 40:59–66, 1993.

[15] William J. Fry and Ruth B. Fry. Determination of absolute sound levels and acoustic absorption coefficients by thermocouple probes - theory. *Journal of the Acoustical Society of America*, 26(3):294–310, May 1950.

[16] William J. Fry and Ruth B. Fry. Determination of absolute sound levels and acoustic absorption coefficients by thermocouple probes - experiment. *Journal of the Acoustical Society of America*, 26(3):311–317, May 1950.

[17] K. J. Parker. The thermal pulse decay technique for measuring ultrasonic absorption coefficients. *Journal of the Acoustical Society of America*, 74(5):1356–1361, 1983.

[18] K. J. Parker. Effects of heat conduction and sample size on ultrasonic absorption measurements. *Journal of the Acoustical Society of America*, 77(2):719–725, 1985.

[19] F. A. Duck. *Physical properties of tissue: a comprehensive reference book*. Academic Press, London, 1990.

[20] R. L. Clarke and G. R. ter Haar. Temperature rise recorded during lesion formation by high-intensity focused ultrasound. *Ultrasound in Medicine and Biology*, 23(2):299–306, 1997.

[21] E. A. Neppiras. Acoustic cavitation: an introduction. *Ultrasonics*, 22:25–28, 1984.

[22] R. E. Apfel. Acoustic cavitation inception. *Ultrasonics*, 22:167–173, 1984.

[23] E. A. Neppiras. Acoustic cavitation. *Physical Letters*, 61(3):160–251, 1980.

[24] T. G. Leighton. *The acoustic bubble*. Academic Press, San Digeo, California, 1994.

[25] W. J. Fry, V. J. Wulff, D. Tucker, and F. J. Fry. Physical factors involved in ultrasonically-induced changes in living systems: I. identification of non-temperature effects. *Journal of the Acoustical Society of America*, 22(6):867–876, 1950.

[26] F. J. Fry, G. Kossoff, R.C. Eggleton, and F. Dean. Threshold ultrasonic dosages for structural changes in the mammalian brain. *Journal of the Acoustical Society of America*, 48(6):1413–1417, 1970.

[27] K. Hynynen. The threshold for thermally significant cavitation in dog's thig muscle in vivo. *Ultrasound in Medicine and Biology*, 17(2):157–169, 1991.

[28] F. J. Fry, N. T. Sanghvi, R. S. Foster, R. Bihrle, and C. Hennige. Ultrasound and microbubbles - their generation, detection and potential utilization in tissue and organ therapy - experimental. *Ultrasound in Medicine and Biology*, 21(9):1227–1237, 1995.

[29] Padmakar P. Lele. Effects of ultrasound on "solid" mammalian tissues and tumors *in vivo*. In M. H. Repacholi, M. Grandolfo, and A. Rindi, editors, *Ultrasound: Medical Applications, Biological Effects, and Hazard Potential*, pages 275–306. Plenum Press, New York, 1987.

[30] M. H. Repacholi, M. Grandolfo, and A. Rindi, editors. *Effects of ultrasound on 'solid' mamilian tissues and tumors in vivo*, pages 275–306. Plenum, New York, 1986.

[31] J. Y. Chapelon, F. Dupenloup, H. Cohen, and P. Lenz. Reduction of cavitation using pseudo-random signals. *IEEE Transactions on Ultrasonics, Ferroelectronics, and Frequency Control*, 43(4):623–625, 1996.

[32] A. J. Coleman, M. J. Choi, and J. E. Saunders. Detection of acoustic emmision form cavitation in tissue during clinical extracorpeal lithotrispy. *Ultrasound in Medicine and Biology*, 22:1097–1087, 1996.

[33] D. J. Watmough, R. Lakshem, F. Ghezz, K. M. Quan, J. A. Watmough, E. Khizhnyak, T. N. Pashovkin, and A. P. Sarvazyn. The effect of gas bubbles on the production of ultrasound hyperthermia at 0.75 mhz: A phantom study. *Ultrasound in Medicine and Biology*, 19(3):231–241, 1993.

[34] S. Fujishiro, M. Mitsumori, Y. Nishimura, Y. Okuno, Y. Nagata, M. Hiraoka, T. Sano, T. Marume, and N. Takayama. Increased heating efficiency of hyperthermia using and ultrasound contrast agent: a phantom study. *International Journal of Hyperthermia*, 14(5):495–502, 1998.

[35] J. Wu. Temperature rise generated by ultrasound in the presence of constrast agent. *Ultrasound in Medicine and Biology*, 24:267–274, 1998.

[36] S. Hilgenfeldt, D. Lohse, and M. Zomack. Response of bubbles to diagnostic ultrasound: a unifying theoretical approach. *European Physics Journal B*, 4:247–255, 1998.

[37] S. Hilgenfeldt, D. Lohse, and M. Zomack. Sound scattering and localized heat deposition of pulse-driven microbubbles. *Journal of the Acoustical Society of America*, 107(6):3530–3539, 2000.

[38] F. Chavrier, J. Y. Chapleon, A. Gelet, and D Cathignol. Modeling of high-intensity focused unltrasound induced lesions in the presense of cavitation bubbles. *Journal of the Acoustical Society of America*, 108(1):432–440, July 200.

[39] H. H. Pennes. Analysis of tissue arterial blood temperatures in the resting human forearm. *Journal of Applied Physiology*, 1(2):93–122, 1948.

[40] C. A. Damianou, K. Hynynen, and X. Fan. Evaluation of accuracy of a theoretical model for predicting the necrosed tissue volume during focused ultrasound surgery. *IEEE Transactions on Ultrasonics, Ferroelectronics, and Frequency Control*, 42(2):182–187, 1995.

[41] M. C. Kolios, A. E. Worthington, M. D. Sherar, and J. W. Hunt. Experimental evaluation of two simple thermal models using transient temperature analysis. *Phyics in Medicine and Biology*, 43:3325–3340, 1998.

[42] Matthew G. Skinner, Megumi N. Iizuka, Michael C Kolios, and Michael D. Sherar. A theoretical comparison of energy sources - microwave ultrasound and laser - for interstitial thermal therapy. *Physics in Medicine and Biology*, 43:3535–43547, 1998.

[43] P. P. Lele. A simple method for production of trackless focal lesions with focused ultrasound; physical factors. *Journal of Physiology*, 160:494–511, 1962.

[44] H. S. Carslaw and J. C. Jaeger. *Conduction of Heat in Solids*. Clarendon, Oxford, 1947.

[45] C. L. Liu and J. W. Liu. *Linear Systems Analysis*. McGraw-Hill, New York, 1975.

[46] E. H. Wissler. Pennes' 1948 paper revisited. *Journal of Applied Physiology*, 85:36–42, 1998.

[47] David A. Nelson. Invited editorial on "pennese' 1948 paper revisted". *Journal of Applied Physiology*, 85:2–3, 1998.

[48] C. K. Charney. Mathematical models of bioheat transfer. In Y. I. Cho, editor, *Advances in Heat Transfer*, pages 19–155. Academic, 1992.

[49] I. M. Hallaj. *Nonlinear acoustics in underwater and biomedical applications: Array performance degradation and time reversal invariance*. PhD thesis, University of Washington, 1999.

[50] P. J. Westervelt. Parametric acoustic array. *Journal of the Acoustical Society of America*, 35:535–537, 1963.

[51] B. E. Noltingk and E. A. Neppiras. Cavitation produced by ultrasonics. *Proceedings of the Physical Society of London Section B*, 63:674–685, 1950.

[52] E. A. Neppiras and B. E. Noltingk. Cavitation produced by ultrasonics: Theoretical conditions for the onset of cavitation. *Proceedings of the Physical Society of London Section B*, 64:1032–1038, 1950.

[53] H. G. Flynn. Physics of acoustic cavitation in liquids. In W. P. Mason, editor, *Physical Acoustics: Principles and Methods*, volume I/B, chapter 9, pages 57–172. Academic Press, New York, 1964.

[54] Ronald A. Roy. Cavitation sonophysics. In L. A. Crum et. al., editor, *Sonochemistry and Sonoluminescence*, pages 25–38. Kluwer Academic Press, Dordrecht, Netherlands, 1999.

[55] R. A. Roy, S. I. Madanshetty, and R. E. Apfel. An acoustic backscattering technique for the detection of transient cavitation produced by microsecond pulses of ultrasound. *Journal of the Acoustical Society of America*, 87(6):2451–2458, 1990.

[56] A. M. Calabrese. *Threshold measurements and production rates for inertial cavitation due to pulsed, megahertz-frequency ultrasound*. PhD thesis, University of Mississippi, May 1996.

[57] H. F. Bowman, E. G. Cravalho, and M. Woods. Theory, measurement and application of thermal properties of biomaterials. *Annual Review of Biophysics and Bioengineering*, 4:43–80, 1975.

[58] A. J. H. Vendrick and J. J. Vos. A method for the measurement of the thermal conductivity of human skim. *Journal of Applied Physiology*, 11:211–215, 1957.

[59] Alan V. Oppenheim, Alan S. Willsky, and S. Hamid Nawab. *Signals and Systems*. Prentice Hall, New Jersey, 2 edition, 1997.

[60] Julius S. Bendat and Allan G. Piersol. *Random Data: Analysis and measurement procedures*. Wiley-Interscience, New York, 1971.

[61] N. A. Watkin, G. R. ter Haar, and I. Rivens. The intensity dependence of the site of maximal energy deposition in focused ultrasound surgery. *Ultrasound in Medicine and Biology*, 22(4):483–491, 1996.

[62] Anthony Eller and H. G. Flynn. Rectified diffusion during nonlinear pulsations of cavitation bubbles. *Journal of the Acoustical Society of America*, 37(3):493–503, 1965.

[63] Christy Katherine Holland. *Thresholds of Transient Cavitation Produced by Pulsed Ultrasound in a Controlled Nuclei Environment*. Ph.d. thesis, Yale University, 1989.

[64] F. E. Fox and K. F. Herzfeld. Gas bubbles with organic skin as cavitation nuclei. *Journal of the Acoustical Society of America*, 26:984–989, 1954.

[65] M. G. Sirotyuk. Stabilisation of gas bubbles in water. *Soviet Physical Acoustics*, 16:237–240, 1970.

[66] D. E. Young. Skins of variable permeability: a stabalisation mechanism for gas cavitation nuclei. *Journal of the Acoustical Society of America*, 65:1429–1439, 1979.

[67] D. E. Young. On the evolution, generation, and regeneration of gas cavitation nuclei. *Journal of the Acoustical Society of America*, 71:1473–1481, 1982.

[68] D. E. Young, E. W. Gillary, and D. C. Hoffman. A microscopic investigation of bubble formation nuclei. *Journal of the Acoustical Society of America*, 76:1511–1521, 1984.

[69] E.N. Harvey, D. Barnes, W. P. McElroy, A.H. Whitley, C. C. Pease, and K. W. Cooper. Bubble formation in animals i: Physical factors. *Journal of Cellular and Comparative Physiology*, 24:1–22, 1944.

[70] R. E. Apfel. The role of impurites in cavitation-threshold determination. *Journal of the Acoustical Society of America*, 48:1179–1186, 1970.

[71] A. A. Atchley and L. A. Crum. *Ultrasound: Its Chemical, Physical and Biological Effects*, chapter 1, pages 1–64. VCH, New York, 1988.

[72] A. Prosperetti. Physics of acoustic cavitation. In D. Sette, editor, *Frontiers of Physical Acoustics*, pages 145–188. Corso, Bologna, Italy, 1988.

[73] Lord Rayleigh. On the pressure developed in a liquid during the collapse of a spherical cavity. *Philosophical Magazine*, 34:94–98, 1917.

[74] M. S. Plesset. The dynamics of cavitation bubbles. *Journal of Applied Mechanics*, 16:277–282, 1949.

[75] F. G. Blake. Technical memo 12. Technical report, Acoustics Research Laboratory, Harvard University, Cambridge, Massachusetts, 1949.

[76] A. Prosperetti. Bubble phenomena in sound fields: part one. *Ultrasonics*, pages 69–77, 1984.

[77] A. Prosperetti. Bubble phenomena in sound fields: part two. *Ultrasonics*, pages 115–124, 1984.

[78] Jr. Charles Devin. Survey of thermal, radiation, and viscous damping of pulsating air bubbles in water. *Journal of the Acoustical Society of America*, 31(12):1654–1667, 1959.

[79] P. S. Epstein and M.S. Plesset. On the stability of gas bubbles in liquid-gas solutions. *Journal of Chemical Physics*, 18:1505–1509, 1950.

[80] J. S. Allen and R. A. Roy. Dynamics of gas bubbles in viscoelastic fluids. i. linear viscoelasticity. *Journal of the Acoustical Society of America*, 107(6):3167–3178, June 2000.

[81] R. A. Roy. Dynamics of gas bubbles in viscoelastic fluids. ii. nonlinear viscoelasticity. *Journal of the Acoustical Society of America*, 108(4):1640–1650, October 2000.

[82] H. Poritsky. The collapse or growth of a spherical bubble or cavity in a viscous fluid. In E. Sterberg, editor, *Proceedings of the First U.S. National Congress on Applied Mechanics*, pages 813–821, New York, 1952.

[83] W. Lauterborn. Numerical inverstigation of nonlinear oscillations of gas bubbles in liquids. *Journal of the Acoustical Society of America*, 59(2):283–293, 1976.

[84] J. B. Keller and M. Miksis. Bubble oscillations of large amplitude. *Journal of the Acoustical Society of America*, 68(2):628–633, 1980.

[85] U. Parlitz, V. Englisch, C. Scheffczyk, and W. Lauterborn. Bifurcation structure of bubble oscillators. *Journal of the Acoustical Society of America*, 88(2):1061–1077, 1990.

[86] D. Daniels, J. M. Davies, W. D. Paton, and E. B. Smith. The detection of gas bubbles in guinea-pigs after decompression from air saturation dives using ultrasonic imaging. *Journal of Physiology*, pages 380–369, 1980.

[87] G. R. ter Haar and S. Daniels. Evidence for ultrasonically induced cavitation *in vivo*. *Physics of Medicine and Biology*, 26:1145–1149, 1981.

[88] R. E. Apfel and C. K. Holland. Gauging the likelihood of cavitation from short-pulse, low-duty cycle diagnostic ultrasound. *Ultrasound in Medicine and Biology*, 17(2):197–185, 1991.

[89] J. S. Allen, R A. Roy, and C. C. Church. On the role of shear viscosity in mediating inertial cavitation from short-pulse megahertz-frequency ultrasound. *IEEE Transactions on Ultrasonics, Ferroelectrics, and Frequency Control*, 44(4):743–751, July 1997.

[90] A. Prosperetti. Thermal effects and damping mechanisms in the forced radial oscillations of gas bubbles. *Journal of the Acoustical Society of America*, 61(1):17–27, 1977.

[91] A. Prosperetti. The thermal-behavior of oscillating gas-bubble. *Journal of Fluid Mechanics*, 222:587–616, 1991.

[92] V. Kamath, H. N. Oğuz, and A. Prosperetti. Bubble oscillations in the nearly adiabatic limit. *Journal of the Acoustical Society of America*, 92(4):2016–2023, 1992.

[93] L. D. Landau and E. M. Lifshitz. *Fluid Mechanics*, volume 6 of *Course of Theoretical Physics*, chapter 8, pages 279–281. Pergamon Press, Oxford, 1982.

[94] Allan D. Pierce. *Acoustics*, chapter 4, pages 154–155. Acoustical Society of America, Woodbury, New York, 1994 edition, 1994.

[95] L. Konic, J. I Gersten, and C. Yuan. Theore. *Journal of the Acoustical Society of America*, 92(4):2016–2023, 1992.

[96] M. Kornfeld and L. Suvorov. On the destructive action of cavitation. *Journal of Applied Physics*, 15:495–506, 1944.

[97] T. G. Leighton. *The acoustic bubble*. Academic Press, San Digeo, California, 1994.

[98] C. A. J. Fletcher. *Computational Techniques for Fluid Dynamics*, volume 1 of *Springer series in computational physics*. Springer-Verlag, Berlin, 2nd edition, 1991.

[99] J. L. Buchanan and P. R. Turner. *Numerical Methods and Analysis*. International series in pure and applied mathematics. McGraw Hill, Inc., New York, 1992.

[100] Kane S. Yee. Numerical solution of initial boundary value problems involving maxwell's equations in isotropic media. *IEEE Transactions on Antennas and Propagation*, 14(8):302–307, May 1966.

[101] J. Robert Fricke. Acoustic scattering from elemental arctic ice features: Numerical modeling results. *Journal of the Acoustical Society of America*, 93(4):1784–1795, 1993.

[102] D. Botteldooren. Acoustical finite-difference time-domain simulation in a quasi-cartesian grid. *Journal of the Acoustical Society of America*, 95(5):2313–2319, 1994.

[103] Shuozong Wang. Finite-difference time-domain approach to underwater acoustic scattering problems. *Journal of the Acoustical Society of America*, 99(4):1924–1931, 1996.

[104] Gerrit Mur. Absorbing boundary conditions for the finite-differen approximation of the time-domain electromagnetic-field equations. *IEEE Transactions on Electromagnetic Compatibility*, 23(4):377–382, November 1981.

[105] R. G. Holt and D. F. Gaitan. Observation of stability boundaries in the parameter space of single bubble sonoluminescence. *Physical Review Letters*, 77(18):3791–3794, October 1996.

[106] C. Damianou and K. Hynynen. Focal spacing and near-field heating during pulsed high-temperature ultrasound therapy. *Ultrasound in Medicine and Biology*, 19(9):777–787, 1993.

[107] H. Wan, P. VanBaren, E. S. Ebbini, and C. A. Cain. Ultrasound surgery: Comparison of strategies using phased array systems. *IEEE Transactions on Ultrasonics Ferroelectrics and Frequncy Control*, 43(6):1085–1098, November 1996.